Jordan Journal of Mechanical and Industrial Engineering (JJMIE)

JJMIE is a high-quality scientific journal devoted to fields of Mechanical and Industrial Engineering. It is published by Hashemite University in corporation with the Jordanian Scientific Research Support Fund.

SUBMISSION ADDRESS:

Prof. Ahmed Al-Ghandoor, Editor-in-Chief
Jordan Journal of Mechanical & Industrial Engineering,
Hashemite University,
PO Box 330127, Zarqa, 13133 , Jordan
E-mail: jjmie@hu.edu.jo

Hashemite Kingdom of Jordan

Hashemite University

Jordan Journal of Mechanical and Industrial Engineering

JJMIE

An International Peer-Reviewed Scientific Journal

Financed by Scientific Research Support Fund

http://jjmie.hu.edu.jo/

ISSN 1995-6665

Jordan Journal of Mechanical and Industrial Engineering (JJMIE)

JJMIE is a high-quality scientific journal devoted to fields of Mechanical and Industrial Engineering. It is published by The Jordanian Ministry of Higher Education and Scientific Research in corporation with Hashemite University.

Introduction: The Editorial Board is very committed to build the Journal as one of the leading international journals in mechanical and industrial engineering sciences in the next few years. With the support of the Ministry of Higher Education and Scientific Research and Jordanian Universities, it is expected that a heavy resource to be channeled into the Journal to establish its international reputation. The Journal's reputation will be enhanced from arrangements with several organizers of international conferences in publishing selected best papers of the conference proceedings.

Aims and Scope: *Jordan Journal of Mechanical and Industrial Engineering* (JJMIE) is a refereed international journal to be of interest and use to all those concerned with research in various fields of, or closely related to, mechanical and industrial engineering disciplines. *Jordan Journal of Mechanical and Industrial Engineering* aims to provide a highly readable and valuable addition to the literature which will serve as an indispensable reference tool for years to come. The coverage of the journal includes all new theoretical and experimental findings in the fields of mechanical and industrial engineering or any closely related fields (Materials, Manufacturing, Management, Design, Thermal and Fluid, Energy, Control, Mechatronics, and Biomedical). The journal also encourages the submission of critical review articles covering advances in recent research of such fields as well as technical notes.

Guide for Authors

Manuscript Submission:

High-quality submissions to this new journal are welcome now and manuscripts may be either submitted online or email.

Online: For online and email submission upload one copy of the full paper including graphics and all figures at the online submission site, accessed via http://jjmie.hu.edu.jo. The manuscript must be written in MS Word 2010 Format. All correspondence, including notification of the Editor's decision and requests for revision, takes place by e-mail and via the Author's homepage, removing the need for a hard-copy paper trail.

Submission address and contact:

Prof. Ahmed Al-Ghandoor
Editor-in-Chief
Jordan Journal of Mechanical & Industrial Engineering,
Hashemite University,
PO Box 330127, Zarqa, 13115, Jordan
E-mail: jjmie@hu.edu.jo

Types of contributions*:* Original research papers and Technical reports

Corresponding author: Clearly indicate who is responsible for correspondence at all stages of refereeing and publication, including post-publication. Ensure that telephone and fax numbers (with country and area code) are provided in addition to the e-mail address and the complete postal address. Full postal addresses must be given for all co-authors.

Original material: Submission of an article implies that the work described has not been published previously (except in the form of an abstract or as part of a p ublished lecture or academic thesis), that it is not under consideration for publication elsewhere, that its publication is approved by all authors and that, if accepted, it will not be published elsewhere in the same form, in English or in any other language, without the written consent of the Publisher. Authors found to be deliberately contravening the submission guidelines on originality and exclusivity shall not be considered for future publication in this journal.

Withdrawing: If the author chooses to withdraw his article after it has been assessed, he shall reimburse JJMIE with the cost of reviewing the paper.

Manuscript Preparation:

General: Editors reserve the right to adjust style to certain standards of uniformity. Original manuscripts are discarded after publication unless the Publisher is asked to return original material after use. Please use MS Word 2010 for the text of your manuscript.

Structure: Follow this order when typing manuscripts: Title, Authors, Authors title, Affiliations, Abstract, Keywords, Introduction, Main text, Conclusions, Acknowledgements, Appendix, References, Figure Captions, Figures and then Tables. Please supply figures imported into the text AND also separately as original graphics files. Collate acknowledgements in a separate section at the end of the article and do not include them on the title page, as a footnote to the title or otherwise.

Text Layout: Use 1.5 line spacing and wide (3 cm) margins. Ensure that each new paragraph is clearly indicated. Present tables and figure legends on separate pages at the end of the manuscript. If possible, consult a recent issue of the journal to become familiar with layout and conventions. All footnotes (except for table and corresponding author footnotes) should be identified with superscript Arabic numbers. To conserve space, authors are requested to mark the less important parts of the paper (such as records of experimental results) for printing in smaller type. For long papers (more than 4000 words) sections which could be deleted without destroying either the sense or the continuity of the paper should be indicated as a guide for the editor. Nomenclature should conform to that most frequently used in the scientific field concerned. Number all pages consecutively; use 12 or 10 pt font size and standard fonts.

Corresponding author: Clearly indicate who is responsible for correspondence at all stages of refereeing and publication, including post-publication. The corresponding author should be identified with an asterisk and footnote. Ensure that telephone and fax numbers (with country and area code) are provided in addition to the e-mail address and the complete postal address. Full postal addresses must be given for all co-authors. Please consult a recent journal paper for style if possible.

Abstract: A self-contained abstract outlining in a single paragraph the aims, scope and conclusions of the paper must be supplied.

Keywords: Immediately after the abstract, provide a maximum of six keywords (avoid, for example, 'and', 'of'). Be sparing with abbreviations: only abbreviations firmly established in the field may be eligible.

Symbols: All Greek letters and unusual symbols should be identified by name in the margin, the first time they are used.

Units: Follow internationally accepted rules and conventions: use the international system of units (SI). If other quantities are mentioned, give their equivalent in SI.

Maths: Number consecutively any equations that have to be displayed separately from the text (if referred to explicitly in the text).

References: All publications cited in the text should be presented in a list of references following the text of the manuscript.

Text: Indicate references by number(s) in square brackets in line with the text. The actual authors can be referred to, but the reference number(s) must always be given.

List: Number the references (numbers in square brackets) in the list in the order in which they appear in the text.

Examples:

Reference to a journal publication:

[1] M.S. Mohsen, B.A. Akash, "Evaluation of domestic solar water heating system in Jordan using analytic hierarchy process". Energy Conversion & Management, Vol. 38 (1997) No. 9, 1815-1822.

Reference to a book:

[2] Strunk Jr W, White EB. The elements of style. 3rd ed. New York: Macmillan; 1979.

Reference to a conference proceeding:

[3] B. Akash, S. Odeh, S. Nijmeh, "Modeling of solar-assisted double-tube evaporator heat pump system under local climate conditions". 5th Jordanian International Mechanical Engineering Conference, Amman, Jordan, 2004.

Reference to a chapter in an edited book:

[4] Mettam GR, Adams LB. How to prepare an electronic version of your article. In: Jones BS, Smith RZ, editors. Introduction to the electronic age, New York: E-Publishing Inc; 1999, p. 281-304

Free Online Color : If, together with your accepted article, you submit usable color and black/white figures then the journal will ensure that these figures will appear in color on the journal website electronic version.

Tables: Tables should be numbered consecutively and given suitable captions and each table should begin on a new page. No vertical rules should be used. Tables should not unnecessarily duplicate results presented elsewhere in the manuscript (for example, in graphs). Footnotes to tables should be typed below the table and should be referred to by superscript lowercase letters.

Notification: Authors will be notified of the acceptance of their paper by the editor. The Publisher will also send a notification of receipt of the paper in production.

Copyright: All authors must sign the Transfer of Copyright agreement before the article can be published. This transfer agreement enables Jordan Journal of Mechanical and Industrial Engineering to protect the copyrighted material for the authors, but does not relinquish the authors' proprietary rights. The copyright transfer covers the exclusive rights to reproduce and distribute the article, including reprints, photographic reproductions, microfilm or any other reproductions of similar nature and translations.

Proof Reading: One set of page proofs in MS Word 2010 format will be sent by e-mail to the corresponding author, to be checked for typesetting/editing. The corrections should be returned within **48 hours**. No changes in, or additions to, the accepted (and subsequently edited) manuscript will be allowed at this stage. Proofreading is solely the author's responsibility. Any queries should be answered in full. Please correct factual errors only, or errors introduced by typesetting. Please note that once your paper has been proofed we publish the identical paper online as in print.

Author Benefits:

No page charges: Publication in this journal is free of charge.

Free offprints: One journal issues of which the article appears will be supplied free of charge to the corresponding author and additional offprint for each co-author. Corresponding authors will be given the choice to buy extra offprints before printing of the article.

Editorial Preface

It is my pleasure to introduce the first issue of the tenth volume of Jordan Journal of Mechanical and Industrial Engineering (JJMIE). JJMIE is a peer reviewed journal and published in a quarterly base by the Jordanian Ministry of Higher Education and Scientific Research in cooperation with the Hashemite University for mechanical and industrial engineering sciences. JJMIE covers all new theoretical and experimental topics in the fields of mechanical and industrial engineering and any closely related fields. JJMIE has succeeded in the previous volumes to provide an interdisciplinary scientific and engineering communication and to strengthen links between science and policy.

The success we have achieved in the first nine volumes was great; the number of articles we received for review from all over the world increased in steady trend. JJMIE aims to provide readers worldwide with high quality peer-reviewed articles on a wide variety of issues related to mechanical and industrial engineering. Our policy is to select papers for publication which fall within the journal's scope which make a significant contribution to the international research literature. JJMIE provides authors with high quality, helpful reviews to assist authors in improving their manuscripts. As a result of this effort, JJMIE has been indexed recenlty by ISI Thomson.

The tenth volume of JJMIE will include four issues, eigth manuscripts in each issue. In the coming year, it is my vision to have JJMIE publishes more outstanding manuscripts from distinguished scholars in the areas of mechanical and industrial engineering. Accordingly, I would like to request your participation by submitting quality manuscripts for review and encouraging your colleagues to submit quality manuscripts for review. Furthermore, I would like to thank the JJMIE Editorial Board members for their exceptional work and continuous support to JJMIE. Moreover, I would like to thank the group of outstanding reviewers for their valuable contributions they provided to authors.

Prof. Ahmed M. Al-Ghandoor

Editor–in-Chief

Hashemite University

Zarqa, Jordan

JJMIE

Volume 10 Number 1, March.2016
ISSN 1995-6665

Jordan Journal of Mechanical and Industrial Engineering

JJMIE

Volume 10 Number 1, March.2016
ISSN 1995-6665
Pages 1- 9

Jordan Journal of Mechanical and Industrial Engineering

Combined Solar-Geothermal Power Generation using Organic Rankine Cycle

Ahmad Sakhrieh[a,b *], Waleed Shreim[b], Hatem Fakhruldeen[b], Hasan Hasan[b], Ahmed Al-Salaymeh[b]

[a]*Department of Mechanical and Industrial Engineering, American University of Ras Al Khaimah, 10021 UAE*

[b]*Mechanical Engineering Department, The University of Jordan, Amman 11942, Jordan*

Received 10 June 2015 *Accepted 13 Feb 2016*

Abstract

This research investigates the possibility of power generation from geothermal and solar heat resources in Jordan using Organic Rankine Cycle (ORC). A comprehensive thermodynamic modelling and analysis is done in order to choose the appropriate fluid for the considered application.

Fluid selection process using EES software was conducted on sixteen fluids taking into account high side and low side temperature and pressure to be the most important parameters. A step by step thermodynamic modelling with the aid of both EES and CHEMCAD software was conducted simultaneously. Several improvements have been done on the cycle to achieve the most economical and efficient design. For the selected cycle, different components were sized and defined.

It was found that R600 is the most suitable fluid for application under study. The use of geothermal water as a heat source was found insufficient to generate power due to low temperature of the geothermal water. The open feed heater solar and geothermal Organic Rankine Cycle was found to be the most suitable for power generation for the selected site conditions.

Keywords: *Geothermal Energy, Solar Energy, Organic Rankine Cycle, Combined Geothermal-Solar, Organic Fluid Selection*.

1. Introduction

The Hashemite Kingdom of Jordan occupies a strategic location in the Middle East at an important crossroads for regional electrical energy integration. It is a developing non-oil producing country, where its energy requirements are obtained by importing oil from neighboring countries. The cost of importing energy creates a heavy financial burden on the national economy. Furthermore, the levels of electricity consumption are expected to double in the next 15 years. Renewable energy applications in Jordan include solar water heaters, solar photovoltaic, wind farms, hydropower and biogas. The total contribution of renewable energy in Jordan is about 3% of the total energy mix. The national energy strategy aims to integrate renewable energy in the energy system by allocating 7% of the total energy from renewable energy sources within the next 7 years. Moving forward looking for new energy technologies that can decrease our dependence on fossil fuels are needed. Organic Rankine Cycle (ORC) seems to be an important technology that can be used in future. It has a wide variety of applications that include power generation form low grade temperature energy sources. The cycle is compatible with a variety of heat sources such as exhaust, industrial process waste heat, geothermal energy sources, and solar energy.

In the past twenty years, because of its feasibility and reliability, Organic Rankine Cycle has received widespread attentions and researches [1]. ORC is a technology that can convert thermal energy at relative low temperatures in the range of 60 to 350 °C to electricity and can therefore play an important role to improve the energy efficiency of new or existing applications. Beside industrial waste heat, alternative heat sources such as solar and geothermal energy as well as biomass ORC can be applied. Zahra et al modeled and optimized an Organic Rankine Cycle for diesel engine waste heat recovery. In their work four refrigerants including R123, R134a, R245fa and R22 are selected and studied as working fluids. Then, the fast and elitist NSGA-II (Non-dominated Sorting Genetic Algorithm) is applied to maximize the thermal efficiency and minimize the total annual cost (sum of investment cost, fuel cost and environmental cost) simultaneously [2]. A two-stage organic Rankine cycle concept with internal heat recovery was presented by Dominik et al [3]. Leonardo studied a 100 kW_e hybrid plant consisting of gasification system, solid oxide fuel cells and Organic Rankine Cycle. More than hundred fluids are considered as possible alternative for the organic cycle using non-ideal equations of state (or state-of-the-art

* Corresponding author e-mail: ahmad.sakhrich@aurak.ac.ae.

equations of state). A genetic algorithm is employed to select the optimal working fluid and the maximum pressure for the bottoming cycle [4]. The technical and economic feasibility of converting waste heat from a stream of liquid kerosene which must be cooled down to control the vacuum distillation temperature was investigated by H.C. Jung et al. The operating conditions and performance of the ORC system were evaluated with eight potential refrigerants and refrigerant mixtures such as R123, R134a, R245fa, isobutane, butane, pentane, an equimolar mixture of butane and pentane, and a mixture of 40% isobutane and 50% butane on a mole basis. A financial model was established for the total plant cost [5]. The thermodynamic performance of the ORC with a wet cooling system is analyzed using hydrocarbon working fluids driven by geothermal water from 100 °C to 150 °C and reinjection temperatures not less than 70 °C [6]. A thermodynamic modelling study of the utilization of an existing geothermal low-temperature heat source situated at Waddan city in Libya showed that the suggested station can provide Waddan city and surrounding villages with their demand of electrical and thermal energy [7].

The main difference between organic fluids and water is the lower evaporation energy of the former, so less heat is needed to evaporate the organic fluid. This ensures that low temperature waste heat of 60 to 100°C can be used as a heat source to the ORC installation. Accordingly, ORC is extremely suitable for waste heat recuperation in the industry and low temperature geothermal sources.

The selection of a suitable working fluid is not that easy. For most of the organic fluids vapour tables and saturation curves are unknown. Without the knowledge of the saturation pressures and temperatures it is not possible to evaluate the suitability of a fluid in any given application. Depending on the type of heat source (hot water, exhaust gases, geothermal) and its temperature level, a suitable working fluid with appropriate evaporation and condensing temperatures has to be selected.

In order to investigate the possibility of power generation from geothermal resources in Jordan, data from literature has been analyzed. A combined low grade temperature heat resource that exists in Jordan in the form of hot water springs, average temperature and flow rates of several springs have been studied.

The location of nearly all the thermal springs and the hot boreholes are dictated by their proximity to the Dead Sea Rift. Thermal springs are distributed along the eastern escarpment of the Dead Sea Rift for distance about 200 km, from Mukheibeh thermal field in the north to Afra and Burbeitta thermal field in the south [8].

2. FLUID SELECTION

The selection of working fluids has a great effect on the system operation conditions; its efficiency and power generation. Working fluids have also environmental impact.

In this research a procedure has been proposed to compare the different working fluids. Theoretical performances as well as thermodynamic and environmental properties of 16 organic fluids have been comparatively assessed for use in low-temperature solar and geothermal Organic Rankine Cycle systems. Efficiencies, pressure ratio, toxicity, flammability, ODP and GWP were used to compare different working fluids. This process was very helpful in selecting the most suitable fluids that match design criteria.

After selecting the most appropriate fluids, a detailed analysis for these fluids including its operating pressures as well as the efficiency and expander output work and the expander pressure ratio was carried out.

2.1. Preliminary selection

The basic Rankine cycle was used as a base to compare the different working fluids, since it gives the highest possible work and efficiency that can be achieved. Boiler pressure, condenser pressure and turbine inlet temperature were varied; consequently efficiency and work output were recorded and considered as the two main parameters for working fluid selection. Heat source temperature was varied as follows 60 °C (low), 120 °C (medium) and 180 °C (high).

Boiler pressure was varied while the condenser pressure was held constant. The work and efficiency vs. boiler pressure were plotted to see the highest work output and efficiency achieved for the three respective regions. Then condenser pressure was varied over the acceptable range for condenser to be used. Finally; boiler pressure was held constant while the work and efficiency for the three regions has been drawn. This process was done for the sixteen fluids that have been chosen to find suitable fluids for ORC applications. Table (1) summarizes the ranges for the boiler pressure, condenser pressure and turbine inlet temperature.

Table 1. Organic Rankine Cycle parameters and their ranges

Parameter	Range	
	Minimum	Maximum
Boiler Pressure (kPa)	500	2500
Condenser Pressure (kPa)	50	150
Turbine Inlet Temperature (kPa)	60	180

A sample of the preliminary fluid selection is shown below as it has been applied to R410a fluid.

Refrigerant 410a:

The first organic working fluid that was explored is the refrigerant R410a. The T-s diagram of the fluid with pressure lines at 50, 150, 500, and 2500 kPa is shown in Figure (1). It is clear from the figure that R410a has low boiling points under reasonable pressure

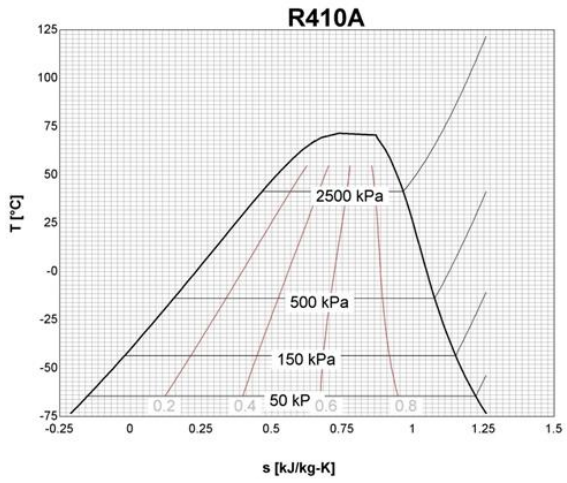

Figure 2. Temperature Entropy diagram for R410a

R410a is used to explore the parameters of the basic Rankine cycle. The sixteen fluids were also explored in the same manor. R410a will be discussed in detail in order to give an over view of the procedure used for fluid selection. For this analysis, one of the state points is pinned to the vapour dome of the working substance while the other was in the superheating region. This means that at the entrance of the expander, the fluid is in the superheating region (superheated vapour) and prior to entering the pump, it has a quality of zero (saturated liquid).

The first parameter whose effect on the cycle was studied was the boiler pressure; it was varied from 500 to 2500 kPa as shown in figure (3). The condenser pressure was kept constant at 50 kPa and a temperature of 60 °C. From figure (3) it can be seen that as the boiler pressure increases the efficiency increases. The work output reaches a maximum value then it becomes constant. The maximum efficiency that was achieved is 27.5 % while the maximum work output is around 95 kJ/kg. It can be seen that the boiler pressure and efficiency have a linear relationship but that doesn't come without drawbacks, since the increased inlet pressure requires a more expensive expander design.

The next parameter that was studied is the condenser pressure which affects the cold side temperature. The boiler pressure is held at 1500 kPa. The cold side temperature is controlled by the ambient temperature, it can be seen from figure (4) that as condenser pressure increases over the selected range the efficiency and work output decrease. This shows an expected behaviour since the difference across the expander pressure decreases. However; there is a limit to how much the pressure can be decreased. The condenser temperature which must be in an acceptable range that is close to ambient temperature.

The same procedure was performed for the medium and high temperature ranges. The results are shown in figures (5a) and (5b) respectively, where the boiler pressure was varied from 500 to 2500 kPa and the condenser pressure was held constant at 50 kPa, while the turbine inlet temperature for medium and high ranges was taken at 120 °C and 180 °C respectively. It is seen that there is a proportional relationship between the boiler pressure with the efficiency and work output, so in order to achieve the highest efficiency and work output the turbine inlet pressure must be taken as high as possible.

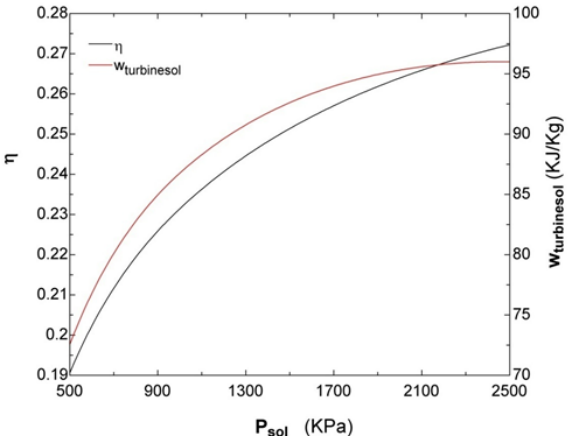

Figure 3. high side pressure versus output work and efficiency

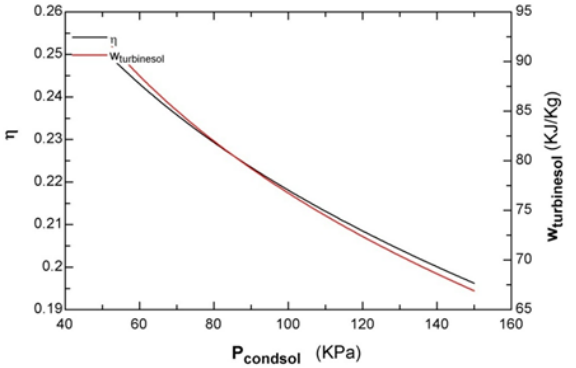

Figure 4. low side temperature versus output work and efficiency

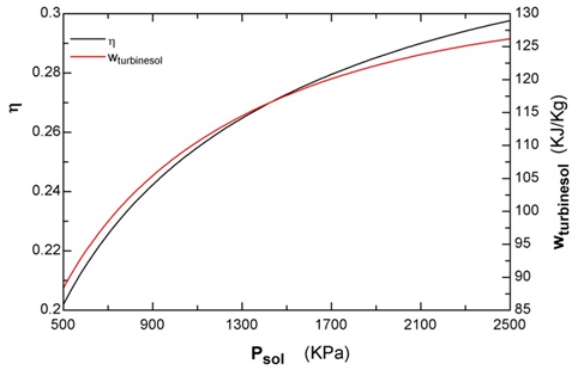

Figure 5(a). high side pressure versus output work and efficiency for medium temperature heat source.

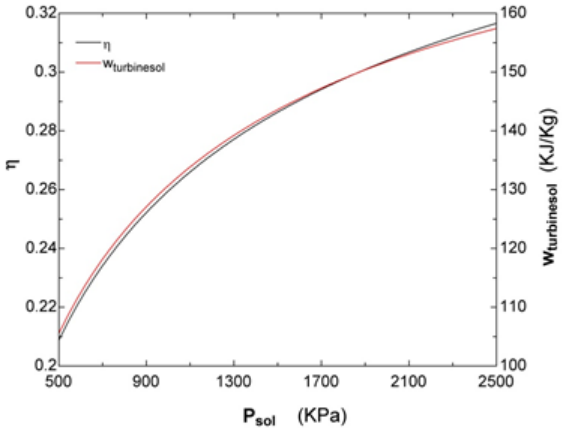

Figure 5(b).: high side pressure versus output work and efficiency for high temperature heat source.

The condenser pressure effect was studied on efficiency and work output. As it is seen in figures (6a) and (6b), the boiler pressure is kept constant while the turbine inlet temperature for medium and high ranges was taken at 120 °C and 180 °C respectively. The relationship resembles previous graphs; since it shows inverse relationship between condenser pressure and efficiency. This agrees with the previous results, which means as the condenser pressure increases, the pressure difference across the expander inlet and outlet decreases. This results in decreased efficiency and work output.

After the preliminary process has been conducted, four fluids have been selected. These fluids have also fulfilled the safety and environmental specifications set by ASHRAE. These four fluids will be deeply analysed. Additional parameters will be taken into account which seems to be important in the performance of the system under study.

These fluids are:

1. R600 (N-Butane)
2. R290 (Propane)
3. R32 (Difluoromethane)
4. R410a (Puron)

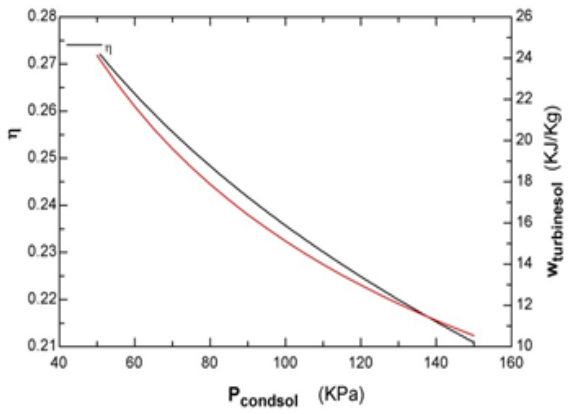

Figure 6(a). low side pressure versus output work and efficiency for high temperature heat source.

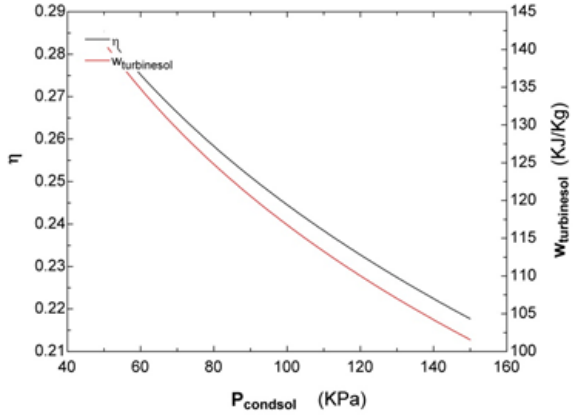

Figure 6(b). Low side pressure versus output work and efficiency for high temperature heat source

Table 2. Summary of the efficiency and output work for the sixteen fluids under different temperature heat sources.

Fluid	Efficiency %			Work (kJ/kg)		
	Low	Mid	High	Low	Mid	High
Ethanol	0.45	10	20.5	6.5	22	70
N-butane	14	16.5	24	13.5	50	164
methanol	2	10.5	18.5	7	30	60
R12	24	29.3	31	20	75	95
R22	27.5	29	32	75	102	127
R32	28	30	31	127	160	180
R114	12.5	24	25	7.5	65	70
R134a	23	27	28	65	95	115
R290	27	30	31	160	215	160
R407c	26.5	28.5	30	83	110	137
R410a	27	29.5	32	95	125	155
R502	27	30	31	62	85	108
R600	14	27	27	50	155	210
R600a	14	27	27	50	157	210
RC318	20	21	21	very low	49	85
water	very low	5	13	2.5	11	60

3. Detailed Analysis for the selected Fluids

R600 (N-Butane)

The first organic working fluid that was explored is the refrigerant R600 which is also known as n-butane. The T-s diagram of the fluid with pressure lines at 12.7, 150, 7600, 2500, and 4000 kPa is shown in Figure (7). The key feature that made R600 attractive is its low boiling points under reasonable pressure. This fluid has an inward slope for the T-S diagram in the gaseous side. This will ensure that the isentropic expansion process will have a 100 % vapour quality.

The first parameter considered was the effect of turbine inlet temperature. Figure (8) shows the effect of rising the temperature on pressure ratio of the turbine and the overall efficiency of the system. Figure (8) also shows that as the high side temperature continues to increase, the rate at which system efficiency grows trends to slow down.

Figure (8) shows the advantage of increasing the inlet temperature of the turbine. When the inlet temperature is increased, the pressure will also increase as shown in Figure (9). Unfortunately, this requires expensive turbine design.

The next parameter of the basic Rankine cycle that was investigated is the cold side temperature of the system. The high side temperature can be controlled better by varying the time of the fluid exposure to the heat source. The low side temperature is heavily dependent on ambient conditions. Figures (10) and (11) shows the importance of keeping the cold side of the cycle as low as possible to improve the performance.

Both the overall efficiency and net work produced by the expander decrease linearly as the low side temperature increases. The only benefit for having a heat sink at a higher temperature is the decreased expander ratio as shown in Figure (12). This added benefit of a lower pressure ratio only keeps the manufacturing process of the expander simple, but this also will affect the overall system negatively.

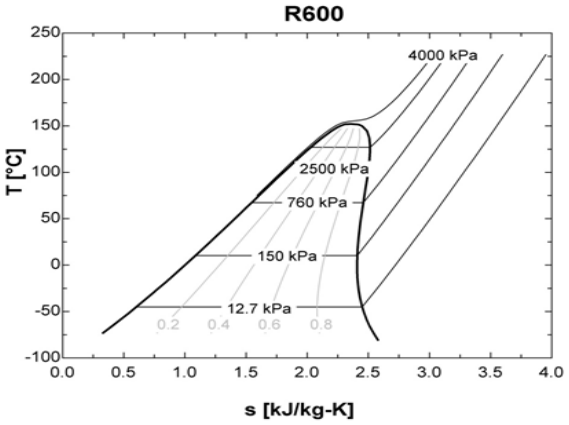

Figure 7. temperature entropy diagram

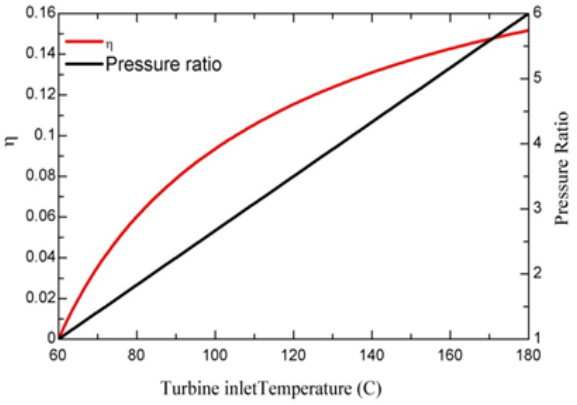

Figure 8. Effect of Expander Inlet Temperature on Pressure Ratio and Efficiency with Fixed Cold Side Temperature

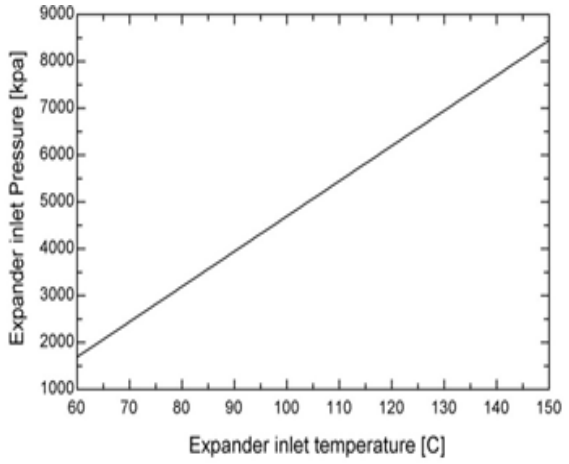

Figure 9. Effect of Expander Inlet Temperature on Inlet Pressure with Fixed Cold Side Temperature

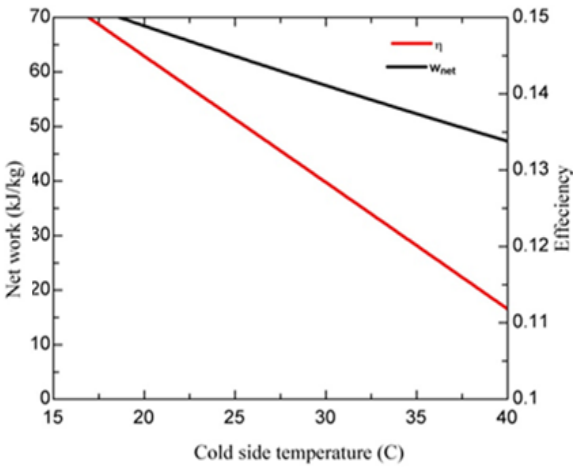

Figure 10. Effects of Cold Side Temperature on System Efficiency and Net Work

The last input of the basic Rankine Cycle to be studied is the boiler pressure. Figure (13) shows that there was a set pressure ratio of five for the expander. The input pressure was varied from 1300 to 2000 kPa to keep within the original system parameters set. The figure shows that for a fixed pressure ratio with the states pinned to the vapor dome, the inlet pressure has an almost negligible effect on the net work and efficiency of the cycle. Figure (13) shows that the relation between the inlet pressure and the expander pressure is linear. There is also an exponential relationship between the inlet pressure and the efficiency of the cycle. The figure demonstrates that the most influential factor on the simple Rankine cycle is the expander ratio.

The same parametric analysis has been done for the fluids: R32, R290, and R410a. The obtained results are summarized in Table 3.

As table (3) shows; three of the fluids have an acceptable condensing temperature that agrees with design ambient temperature. The fluid of maximum efficiency and work is R290 with values of 12.3% and 55 kJ/kg. Its safety group is A3 which means that it is a highly flammable fluid .Thus R600 becomes the first option for design consideration. As it can be seen from table (3) it has an efficiency of 11.5% and a net work of 52 kJ/kg. The use of this fluid will affect the initial cost of the turbine due to high pressure ratio.

4. Thermodynamic Analysis

It was found that R600 is the most suitable fluid for Organic Rankine Cycle, so first it will be analysed using geothermal source as main heat source for the cycle. Based on the results obtained, further optimization will be decided.

4.1. Geothermal Rankine Cycle

The geothermal Rankine cycle is presented in Figure 14. EES and CHEMCAD software are used to analyse this cycle. Table 4 shows the assumptions used.

Table 4. Assumptions made for calculations

Turbine Isentropic Efficiency	85 %
Pump Isentropic Efficiency	85 %
Heat Exchanger Efficiency	85 %
Geothermal water inlet temperature (C^0)	60

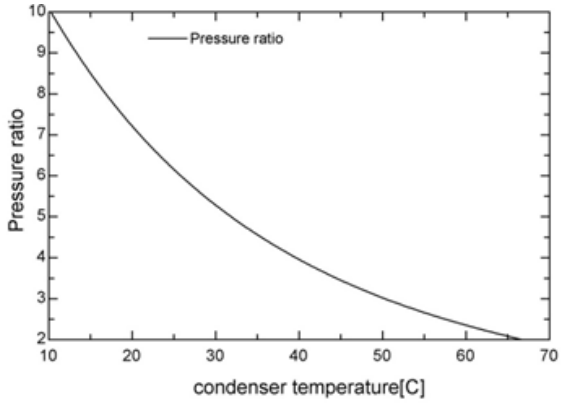

Figure 11. Relationship between Pressure Ratio and Cold Side Temperature

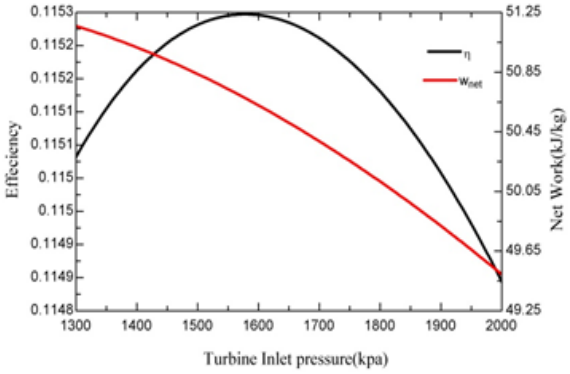

Figure 12. Effects of Expander Inlet Pressure on Efficiency and Net Work with Fixed Pressure Ratio

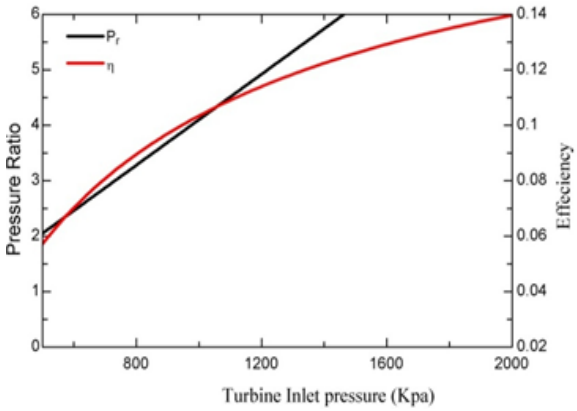

Figure 13. Effects of Expander Inlet Pressure on Efficiency and Pressure Ratio with Fixed Cold Side Temperature

Table 3. Summary for the main design parameters

Fluid	Expander inlet pressure (kPa)	Expander outlet pressure (kPa)	Pressure ratio	Hot Side Temperature (°C)	Cold Side Temperature (°C)	Net Work Output kJ/kg	Optimum Efficiency %
R600	1450	250	6	60	25	52	11.5
R32	1600	800	2	60	24	42	11.3
R290	1550	775	2	60	26	55	12.3
R410a	1600	800	2	60	0	30	11

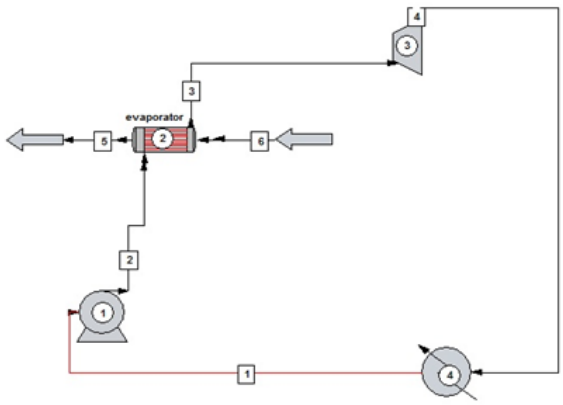

Figure 14. Simple Geothermal Rankine Cycle

4.2. Results and Observations

The results obtained using EEs and CHEMCAD software are given in tables (5) and (6):

Table 5. Streams Characteristics

Stream No.	Temperature using EES (C^0)	Temperature using Chemcad (C^0)	Pressure (KPa)
1	21.75	21.75	220
2	21.78	21.8	300
3	54.27	55	300
4	45.47	47.47	220

Table 6. Geothermal Rankine cycle Performance Characteristics

Quantity in question	Results using EES	Results using Chemcad
Turbine work (kJ/kg)	11.45	11.5
Pump work (kJ/kg)	0.14	0.16
Net work(kJ/kg)	11.31	11.34
Heat input (kJ/kg)	420.70	429.3
Heat output (kJ/kg)	409.40	417.9
Efficiency	2.70 %	2.64 %

A small difference between EES and CHEMCAD results is seen. This can be understood, since EES is more theoretically aligned and gives idealized results, while CHEMCAD simulates results that are close to the actual case; however some idealizations are assumed too.

The results show a low efficiency and work output which is expected due to the low pressure difference across the expander. This is attributed to two reasons, first one is restriction on the evaporator side temperature that is connected to the geothermal water temperature which is capped at 60 °C, and the second one is the condenser temperature, which should be close to the ambient temperature so condenser load is not too high.

It can be concluded that geothermal sources are not enough to generate power in Jordan. In order to increase the efficiency and the work output, the evaporator side temperature must be increased and the condenser side temperature must be lowered. However the condenser temperature is constrained by ambient temperature which (unfortunately) cannot be controlled, so the evaporator side temperature must be increased. However it is constrained by the geothermal side temperature which is topped at 60 °C, so another heat source is needed to be added, this source is solar energy, which is found in abundance in Jordan.

Combined Rankine Cycle

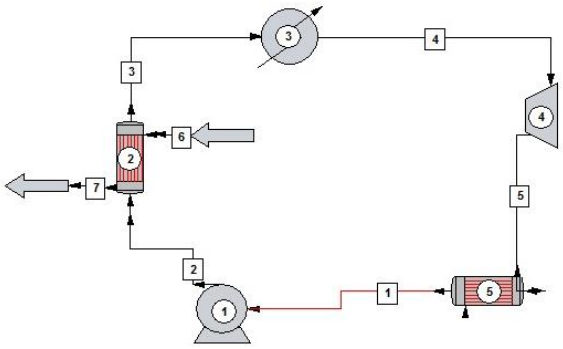

Figure 15. Simple Solar and Geothermal Rankine cycle

A basic Rankine cycle is used here with two heat sources, geothermal water is used as pre heater and solar collector is used as the primary heat source. In figure (15) solar panel is modelled as a boiler with an output temperature of 150 °C. Stream (2) is preheated using geothermal heat exchanger (2). After that stream (3) is passed through solar collector (3) to be evaporated and superheated. The superheated vapor (4) is passed through the expander (4) and its pressure is reduced to the condenser pressure, which must be selected so that condensation temperature doesn't fall below 20 °C. The wet mixture (5) is condensed to saturated liquid (1) in the condenser (5), and then stream (1) is pumped back to the boiler pressure and the cycle starts again.

The Evaporator side pressure is selected to ensure superheating the expander inlet stream, so the expander can be used efficiently with no vapor entering. Also it will be limited by the turbine design. Since we have a solar collector with temperature output of 150 °C the selected pressure is 3500 kPa, which meets the above criteria and will be used in the following cycles as the evaporator pressure. On the other hand, the condenser pressure is selected to ensure that condenser temperature doesn't fall below 20 °C Going below 20 °C requires more energy to be removed which will affect the overall efficiency of the cycle. In the case of R600, it will be 220 kPa, where this pressure will be used in the following cycles as the condenser pressure.

A further modification to the solar and geothermal Rankine cycle was applied and their effect on efficiency and work output was observed. These modifications are using regeneration techniques in the form of open feed heater and closed feed heater.

Open feed heater Solar and Geothermal Rankine cycle alternative was investigated, which showed a small improvement in the efficiency with a small decrease in work output, of 19.1 % and 84.6 KJ/Kg respectively. This behavior is expected since some of the turbine steam is extracted in order to reheat the geothermal heat exchanger inlet, which resulted in the increased efficiency.

Closed feed water heater solar and geothermal Rankine cycle was the next alternative to be studied, which showed a slight improvement from the open feed heater cycle in efficiency and work output of 20 % and 85 KJ/Kg respectively. This means that the open cycle is more feasible than this one, since it has one less component which is the closed feed heater exchanger.

Finally, using both types of regeneration and reheating between turbine stages in a cycle was investigated to its effect on efficiency and work output, surprisingly the efficiency and work output decreased from the previous cycles, where its values is 18% and 86 KJ/Kg respectively, which rendered this cycle infeasible due to its complexity and low return.

5. Conclusions

During the process of exploring different working fluids, a preliminary selection between 16 fluids was conducted. Work and efficiency are considered as key output parameters while the high side pressure, low side pressure and source temperature parameters were the varying ones. A typical behavior resulted for most of the fluids when increasing the temperature and the pressure of high side of the system. The work and efficiency revealed an improvement during that process while they suffered an exponential decrease in their magnitudes as the condenser pressure increases.

Each fluid demonstrated positive result in a given range. For the low temperature range the fluids R22, R32, R134a, R407c, R410a and R502 have show a good efficiency (approximately 27%) and work output. While in the mid range fluids R12, R22, R32, R290, R410a and R502 showed a higher efficiency (approximately 30%) and better work output. Finally in the high temperature range the fluids R12, R22, R32, R290, R410a, R502 and R600 had a slight improvement from the previous range in efficiency of approximately 31% and some fluids showed a good jump in work output.

From the previous fluids, four ones were selected based on their efficiency and power output in the different ranges, these fluids are: R600, R32, R290 and R410a.Those fluids showed very promising results at all ranges of temperature. R600 was found to be the most suitable fluid for our application.

The potential for using geothermal Rankine cycle for power generation in Jordan was studied, taking into accounts geothermal water temperature, its flow rate and the ambient temperature. It was found that this kind of cycle will have low efficiency of 2.7% and power output of 11.34 kJ/kg for geothermal springs in Jordan. This was the result of low geothermal water temperature ($60C^0$) and high ambient temperature which will require a huge amount of heat to be ejected in the condenser. This value is very low in all standards and not feasible to be constructed.

To improve the overall efficiency and power output, a combined solar geothermal cycle was tested. It was found that open feed water heater solar geothermal organic Rankine cycle is the most efficient cycle for power generation in Jordan.

REFERENCES

[1] J. Bao, L. Zhao, “A review of working fluid and expander selections for organic Rankine cycle”. Renewable and Sustainable Energy Reviews, Vol. 24 (2013), 325-342.

[2] Z. Hajabdollahi, F. Hajabdollahi, M. Tehrani, H. Hajabdollahi, “Thermo-economic environmental optimization of Organic Rankine Cycle for diesel waste heat recovery”. Energy, Vol. 63 (2013), 142-151.

[3] D. Meinel, C. Wieland, H. Spliethoff, “Effect and comparison of different working fluids on a two-stage organic Rankine cycle (ORC) concept”. Applied Thermal Engineering, Vol. 63 (2013), 246–253.

[4] L. Pierobon, M. Rokni, U. Larsen, F. Haglind, ”hermodynamic analysis of an integrated gasification solid oxide fuel cell plant combined with an organic Rankine cycle”. Renewable Energy, Vol. 60 (2013), 226-234.

[5] H.C. Jung, S. Krumdiecka, T. Vranjes, “ Feasibility assessment of refinery waste heat-to-power conversion using an organic Rankine cycle”. Energy Conversion and Management, Vol. 77 (2014), 396–407.

[6] Q. Liu, Y Duan, Z. Yang, “Performance analyses of geothermal organic Rankine cycles with selected hydrocarbon working fluids”. Energy, Vol. 63 (2013), 123–132.

[7] S. Masheiti, B. Agnew, “Thermodynamic Simulation Modelling of Low-Temperature Geothermal Source Located in Arid-Zone Area North Africa “JJMIE, Vol. 4 (2010), 61 – 68.

[8] A. Saudi, A. Swarieh, “Geothermal Energy Resources in Jordan, Country Update Report”. Proceedings World Geothermal Congress, Antalya, Turkey, 2005.

[20] Z, Guo , Z. Li, "Size effect on single-phase channel flow and heat transfer at microscale." International Journal of Heat and Fluid Flow. Vol. 24 (2003) 284–298.

[21] Y. Sui, P.S. Lee, C.J. Teo, "An experimental study of flow friction and heat transfer in wavy microchannels with rectangular cross section." International Journal of Thermal Sciences. Vol. 50 (2011), 2473-2482.

[22] H. Shokouhmand, S. Bigham, "Slip-flow and heat transfer of gaseous flows in the entrance of a wavy microchannel." International Communications in Heat and Mass Transfer. Vol. 37 (2010), 695–702.

[23] P.E. Geyer, D.F. Fletcher, B.S. Haynes, "Laminar flow and heat transfer in a periodic trapezoidal channel with semi-circular cross-section", International Journal of Heat and Mass Transfer. Vol. 50 (2007), 3471–3480.

[24] A.M. Guzmán, M.J. Cárdenas, F.A. Urzúa, P.E. Araya, "Heat transfer enhancement by flow bifurcations in asymmetric wavy wall channels". International Journal of Heat and Mass Transfer, Vol. 52 (2009), 3778–3789.

[25] M.Z. Hossain, S. Islam, "Numerical investigation of fluid flow and heat transfer characteristics in sine, triangular, and arc-shaped channels". Thermal Science Vol. (2007) No. 1, 17-26.

[26] A. Agrawal, "A comprehensive review on gas flow in microchannels". International Journal of Micro-Nano Scale Transport. Vol. 2 (2011) No.1, 1-40.

[27] J.C. Maxwell, "On stresses in rarefied gases arising from inequalities of temperature". Philosophical Transactions of the Royal Society of London, Vol. 170 (1879), 231–256.

[28] M. von Smoluchowski, U. Wärmeleitung, "Verdünnten Gasen". Annual Review of Physical Chemistry, Vo. 64 (1898), 101–130.

[29] D.A. Lockerby, J.M. Reese, D.R. Barber, "Velocity Boundary Condition at Solid Wall in Rarefied Gas Calculations". Physical Review E, Vol. 70 (2004) No. 1, 017303 (2004)

[30] Colin S, Single-phase gas flow in microchannels. In: Kandlikar S, Garimella S, Li D, Colin S, King MR, editors. Heat Transfer and Fluid Flow in Minichannels and Microchannels; Oxford, UK, Elsevier Ltd, 2006, p. 9-86.

[31] FLUENT® Inc.

[32] A. Agrawal and S.V. Prabhu, "Survey on measurement of tangential momentum accommodation coefficient". Journal of Vacuum Science and Technology A, Vol. 26 (2008) No. 4, 634-645.

JJMIE

Volume 10 Number 1, March.2016
ISSN 1995-6665
Pages 11- 18

Jordan Journal of Mechanical and Industrial Engineering

Multi-Objective Optimization of Electrical Discharge Machining Processes Using Artificial Neural Network

J. Anitha[a], Raja Das[a], Mohan Kumar Pradhan[b*]

[a] VIT University, Vellore, Tamil Nadu, India
[b] Maulana Azad National Institute of Technology, Bhopal, 462003, India.

Received 30 Jun 2015 Accepted 15 Sep 2015

Abstract

The present study provides predictive models for the functional relationship amongst the input and output variables of Electrical Discharge Machine (EDM) environment. The parametric optimization of this process can be regarded as a multi-objective task. No particular parametric combination of input parameters can offer the maximum Material Removal Rate (MRR) and a better surface finish concurrently, due to its conflicting nature. Hence, a Multi-objective optimization approach has been attempted for the best process parametric combinations by modelling EDM process using of Artificial Neural Networks (ANN). It provides an optimized input data set to EDM system and the results show an improvement with a better productivity, a reduced material removal time and product cost at the material removal rate and surface finish. Extensive experiments have been accompanied with a wide range of machining settings, for modelling and, then, for validating the model. The model is quite capable of predicting the MRR and surface roughness. Also, it is found that the quality of the surface decreases as MRR increases. The maximum MRR obtained is 51.58 mm3/min with the surface finish of 0.1466 µm.

Keywords: *Electrical-Discharge Machining, Artificial Neural Network, Material Removal Rate, Surface Roughness*.

1. Introduction

Electrical Discharge Machining (EDM) is a more widely and effectively non-conventional machining process used. It is rather the fourth in the extensively used machining methods, after milling, turning, and grinding process. Therefore, it is regarded as the most conventional Non-conventional machining process. One of the prime advantages of the process is that it can machine any material, regardless of its hardness as long as the material is electrically conductive, by the application of thermal energy. Thus, it is extensively used for manufacturing of aerospace component, forming tools, injection mould, plastic moulds, forging dies, automobile components, and surgical instruments. Generally, these are made from "difficult-to-machine" materials, such as titanium alloys, nickel-based super alloys, and hardened tool steels, etc. Amongst these materials, AISI D2 tool steel has wide varieties of applications in the die material, in tool and die making applications; furthermore, this steel can be hardened and tempered to offer a higher strength and wear resistance as compared to low carbon steels [1 - 4].

Moreover, EDM process has some limitations as well, viz. the high specific energy consumption, inferior machining performance (productivity) and accuracy of the dimensions of EDMed surface are the some major issues in the die sinking EDM process. These shortcomings mostly limit the applications of EDM. Moreover, it is very tough to control the dimensions in EDM, owing to the complexity and non-linearity of the EDM parameters. Hence, investigators are frequently fascinated with the process modelling and optimization of EDM to increase the accuracy of the process. In the past, substantial development has been dispensed to boost the productivity, and also the versatility of EDM process. Many authors [5 - 10] used the various ANN model to determine the process model considering input parameters such as Ip, Ton, V, etc. for the prediction of responses like MRR and Ra and established that they are performing with reasonable accuracy, under varying machining conditions. Recently with the developments in the soft computing techniques the researchers have paid a great deal of attention to the solution of non-linear problems. It has exhibited a great prospective in solving difficult, non-linear, real-life and complex problems in many different fields manufacturing process modelling, multi-objective optimization, pattern recognition, signal processing and control [2, 7, 11 - 14]. Baraskar *et al.* [15] used an empirical model for relating the surface roughness and MRR, RSM has been applied in developing the models. S. Joshi and S. Pande [16] reposted an intelligent approach for process modeling and optimization of EDM. Physics based process modeling using Finite Element Method (FEM) has been integrated with the soft computing techniques like Artificial Neural Networks (ANN) and Genetic Algorithm (GA) to improve

* Corresponding author e-mail: mohanrkl@gmail.com.

prediction accuracy of the model with less dependence on the experimental data. Yadav and Yadava [17] optimized the process parameters of the slotted electro discharge abrasive grinding process using a combined approach of artificial neural network and non-dominated sorting genetic algorithm II. Das *et al.* [18] used Recurrent Elman Network (REN) for the prediction of the surface roughness in Electrical Discharge Machining (EDM) of SKD 11 tool steel.

In the last two decades, with the developments in the soft computing techniques, researchers have paid a great deal of attention to the solution of non-linear problems. As it has exhibited a great prospective in solving difficult non-linear real- life complex problems in many different fields, manufacturing process modelling, multi-objective optimization, pattern recognition, signal processing and control.

The vital apprehension in EDM is the slower MRR, poor surface quality and precise duplication of the complex tool profile into the die cavity. To improve the MRR, generally a greater discharge current is essential. However, due to this, there is a deterioration of the accuracy of the machined product. The aim of the present analysis is to attain the optimum input parameters for the process by RSM. This may facilitate increasing the productivity (MRR) of the process and precision of the EDMed product. Concurrently, it may lead to the production of complex shapes accurately in shorter lead times. In this trend several efforts have been made for modelling analysing, and optimisation of the EDM process. The intension is to find the suitable parameters that increase the productivity without affecting the surface quality much. EDM process is a very complex process, it is a stochastic process too, and it is affected by many parameters; henceforth it is very difficult to select the parametric combination that could establish the greatest machining performance, i.e., higher MRR along with a decent surface finish. Moreover, these responses MRR and Surface finish are contradictory in nature. Higher MRR is required to achieve high productivity, and a lower surface roughness is required to achieve better surface quality. The aim of the current analysis is to recommend the optimum input process parameters for the process using artificial neural network. This analysis provides an optimized input data set to EDM system and the results show an enhancement and facilitate enhancing the productivity (MRR) and quality accuracy of EDMed components.

2. Experimental Environment

Experiments were conducted as per the following machining condition:

- Processing Machine : Electronica Electraplus PS 50ZNC die-sinking EDM machine Figure 1.
- Work piece material : AISI D2 (DIN 1.2379) tool steel, density 7.7 g/cc, rectangular in shape having a thickness of 4 mm. (with negative polarity).
- Electrode material : electrolytic copper with 30mm diameter with positive polarity
- Flushing : Pressure of 0.3 kg f /cm^2, side flushing technique.
- Dielectric fluid : Commercial grade EDM oil (specific gravity=0.76, freezing point = 94°C).
- Machining Time: 15 min

Figure 1. Experimental setup

Since the influencing parameters of EDM are very diverse and complex, it is therefore chosen on the basis of the literature survey, machining capability, manufactures manual, preliminary experiments and the experience. The four input process parameters, viz. *Ip, Ton, Tau*, and *V* along with the ranges are illustrated in Table 1. The parametric range of pulse current varies from 5 A to 15 A as per the availability in the machine. Pulse duration varies in the range of 50 μs to 100 μs. The duty cycle varies from 50 to 83 and voltage from 40 to 50. To reduce the significance of the unaccounted factor on the response the experiments were carried out in a random order. The responses were observed for each experiment and the results were displayed.

Table 1. Machining Parameters along with their levels.

Input Parameters	Unit	Levels and Values
Ip	A	5, 6,7,8,9,10,11,12,13,14,15
Ton	μs	50, 55, 60, 65, 70, 75, 80, 85, 90, 95, 100
τ		50, 66.5, 75, 80, 83
V	V	40, 41, 42, 43, 44, 45, 46, 47, 48, 49, 50

2.1. Measurement of Response

The response MRR is computed as the volume of material loss from the work material divided by the duration of machining. The obtained Weight loss is transferred to volumetric loss (mm^3/min) using the following equation 1. To calculate the MRR the following equation:

$$MRR = \frac{\Delta V_w}{Ta} = \frac{\Delta W_w}{\rho_w T} \quad (1)$$

where ΔV_w is the loss of volume the work material , ΔW_w is the loss of weight of the work piece, T is the machining time of the process, and ρ_w = 7700 kg/m^3 is the density of the work material. Precision balance (Sartorius, Japan) with a resolution of 0.001 gram was used to measure the weight of the work piece before and after the machining process. For an effective assessment of the EDM process, the greater MRR is considered as the best machining performance.

The other response considered for this analysis was surface roughness. It is regarded as the degree of product quality that influences the cost of the product. This response is also influenced by the input parameters.

The surface roughness of the EDMed surfaces were measured by a portable stylus type profilometer, Talysurf (Taylor Hobson, Surtronic 3+) for the quantitative valuation of the influence of EDM process parameters on the response surface finish. Generally, it is described as the arithmetic mean value of the profile calculated from centerline. It is defined as:

$$\mathrm{R_a} = \frac{1}{\mathrm{L}}\int_0^{\mathrm{L}} |\mathrm{y(x)}|\, \mathrm{dx} \quad (2)$$

where L is the total measured sampling length, y is the profile curve and x is the direction of the profile.

The instrument is set to a sampling length L = 0.8 mm, filter 2 CR, measuring speed 1 mm/s and 4 mm evaluation length. The contour obtained during the measurement was digitized and latter regulated over the dedicated advanced surface finish analysis software, Talyprofile.

The measurement of the roughness was carried out in four different direction to catch all kind of irregularities and the average of the all measurements were taken as the Ra value for the evaluation. The experimental design matrix is depicted in Table 2 along with the measured MRR and Ra, respectively.

3. Multi-objective Optimization

A multi-objective optimization problem involves more than one objective function that need to be optimized simultaneously. Generally, it is not possible to get a single solution that simultaneously optimizes each objective function. In the present paper, multi-objective optimization problem of the EDM process is solved by minimizing the surface roughness and maximizing the material removal rate.

If $MRR = f_1(I_P, T_{on}, \tau, V)$ and $R_a = f_2(I_P, T_{on}, \tau, V)$ Multi-objective optimization problem can be represented by

Maximize $f_1(I_P, T_{on}, \tau, V)$

Minimize $f_2(I_P, T_{on}, \tau, V)$

Subject to

$5 \le I_P \le 15$

$50 \le T_{on} \le 100$

$50 \le \tau \le 83$

$40 \le V \le 50$

$I_P, T_{on}, \tau, V \in Z$

Table 2. Experimental value of the responses MRR and Ra.

Run Order	*Ip* A	*Ton* µs	*Tau* %	*V* volt	MRR mm^3 /min	Ra µm
1	10	75	66.5	45	9.04	5.98
2	5	50	50	50	5.18	5.01
3	5	100	83	40	5.25	5.03
4	5	50	83	40	8.87	4.71
5	15	100	50	50	51.09	8.10
6	10	75	66.5	45	8.95	6.12
7	5	100	50	40	4.35	4.89
8	15	100	50	40	51.00	10.93
9	5	100	83	50	6.97	5.70
10	15	100	83	40	33.02	12.49
11	5	50	83	50	14.12	5.19
12	10	75	66.5	45	8.42	6.54
13	15	50	83	40	20.00	12.01
14	10	75	66.5	40	8.94	8.20
15	10	75	83	45	9.36	7.13
16	15	75	66.5	45	33.08	9.68
17	10	50	66.5	45	9.18	5.87
18	5	75	66.5	45	5.36	6.07
19	10	75	66.5	45	10.35	5.55
20	15	50	83	50	29.16	8.43
21	5	50	50	40	4.61	4.59
22	15	50	50	40	29.74	10.49
23	10	75	66.5	45	11.01	6.25
24	10	75	50	45	9.25	5.92
25	15	50	50	50	33.10	7.43
26	5	100	50	50	4.35	5.59
27	15	100	83	50	33.11	9.01
28	10	75	66.5	50	11.01	6.35
29	10	100	66.5	45	10.43	7.27
30	10	75	66.5	45	9.35	6.75

4. Artificial Neural Networks

Artificial Neural Networks (ANNs) are simple electronic devices modelled after the neural structure of the brain. ANNs are powerful tools for many complex applications such as optimization, system identification and pattern reorganization. ANNs are capable to learn from experiments and to perform non-linear mappings. The processing elements of neural networks are called artificial neurons, or nodes. ANN consists of input layers, which are multiplied by weights, and then evaluated by a mathematical mapping which computes the activation of the neuron. Another function determines the output of the artificial neuron. The artificial neurons of ANNs process the information.

Neural networks are categorized by their structure, activation functions and training algorithms. Each type of

neural networks has its own input-output characteristics; therefore, it could be applied only in some specific processes. In this one, a neural network is employed for modeling the MRR and the Ra in the EDM process. One of artificial neural networks, i.e., Back-Propagation Neural Network (BPNN) is discussed. The BPNN model consists of an input layer, one or two hidden layers, and an output layer in a forward multi-layer neural network. The architecture of a BPNN with n inputs nodes, r outputs nodes and a single hidden layer of m nodes is shown in Figure 2. All the nodes have been multiplying the weights connected with them. Therefore, the output O_k can be expressed as:

$$o_k = \sum_{j=1}^{m} W2_{kj} f\left(\sum_{i=1}^{n} W1W1_{ji} x_i + b1_j\right) + b2_k \qquad (3)$$

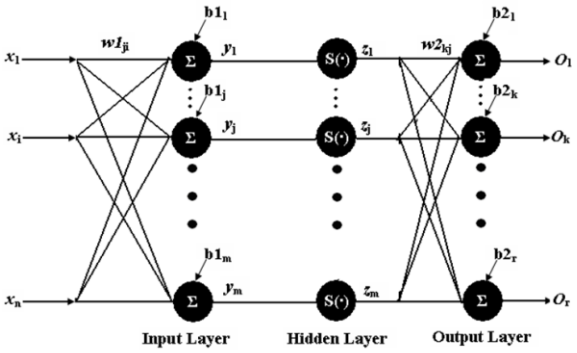

Figure 2. Back-propagation Network

where function f is the transfer function or activation function, $W1_{ji}$ is the weight between the ith input node and jth hidden, $W2_{ji}$ is the weight between the jth hidden node and kth output node, $b1_j$ is the bias at jth hidden node and $b2_k$ is the bias at kth output node.

Eq. 3 presents a kind of function to convert neuron from weighted input to output and also is a kind of network to make non-linear influence into the BPNN. The present study chooses the most general tan-sigmoid transfer function S(·) and is defined as $f(x)) = 2/(1 + \exp(-2x)) - 1$, where the range of the value is $(-1, 1)$. And if a linear function is chosen for this transfer function, such as $f(x) = x$, the whole ANN architecture will become the linear influence from the input layer to the output layer.

In case of BPNN a typical node in the input-layer receives the input vector, sums them as per their weight and bias vectors, passes it through a transfer function and gives an output. This output is then compared with the actual data, and the error is computed. This error is then propagated backwards and used for updating the weight and bias vectors of the neurons. When this process is finished for all the input vectors, it is called as 1 epoch. Once one epoch is over, the mean squared error between the actual output values and the corresponding target values is determined iteratively. The process is repeated until the mean squared error is reached to a particular tolerance value. Once the mean squared error reaches the desired tolerance level, through the training process, the weights are updated and stored so as to present the desired output, which can be used later to predict outputs for a different set of inputs. The learning is based on conjugate gradient descent algorithm. At this stage, the architecture of a network is defined and treated as the trained ANN.

5. Optimization Approach

The trained ANN model is capable of determining the response parameters as a function of four different control (input) parameters, i.e., *Ton, τ , Ip, V*. An attempt was made to generate the highest number of input, output parameter combinations to get more number of optimum points. The input parameters (four in numbers) were divided into all possible levels, as given in Table 1. These considerations resulted in 11 × 10 × 5 × 11 = 6050 possible input combinations. The developed ANN model was used to determine the MRR and Ra for all possible levels of the 6050 combinations. Finally, the results of this study proposed best of these combinations

6. Results

In the present BPNN model, the inputs of the model are *Ton, τ,Ip, V.* The outputs of the model are MRR and Ra. A set of training, validation and testing was performed by 30 data where 22 data were used for training, 6 data were used for validation and 6 for testing. The training data were applied to train the BPNN model, where the testing data were used to verify the adequacy of the trained BPNN model for the prediction of MRR and Ra. The one hidden layered BPNN and two hidden layered BPNN were trained with a different number of neurons. After data training, through different combinations of number of neurons, the comparison results of the actual versus the ANN were obtained. The Mean Absolute Error (MAE) and Mean Percentile Error (MPE), as the difference between actual and ANN, was determined for each MRR and Ra value. Finally, the graphs at hidden neurons were plotted for comparison MRR (actual vs. ANN) and Ra (actual vs. ANN). These graphs are presented in Figures 4 and 5. The most agreeable hidden layers neurons were found 2 and 3 for BPNN model, as shown in Figure 3. The satisfactory MAE and MPE of the trained BPNN for training, validation and testing data sets are given in Tables 3 and 4. Figures 6 and 7 indicate the variation in ANN model values and it can be observed that all the MRR and Ra values through ANN model are coinciding with the actual experimental values. Further, no abnormality in actual Vs ANN data comparison is apparent in the Figures 6 and 7. The Figures show that the performance of ANN model is very close to the actual MRR and Ra, which, in comparison, indicates that the ANN model results are closer to actual outputs. Here, it can be concluded that the ANN model provides better results in the EDM process using D2 steel.

Another parameter, which we have considered to compare the proposed ANN model result with experimental result, is the regression analysis or the R-value. Figure 8 shows the R values based on ANN model and the experimental data for the MRR and Ra. The solid line represents the best possible regression fit between targets and outputs for training, validation, testing and all data sets. The value of R, which is shown on the top of Figure 8, represents the relation-ship between those two. In neural networks, R=1 indicates the perfect match between targets and outputs. Since the net-works cannot be made to learn perfectly, the general value of R lies near to 1. The closer its value to 1, the better the neural network is. On the other hand, the value of R close to 0 indicates the

nonlinear relationship between targets and outputs. For the present study, the input parameters were divided into all possible levels within their working range as illustrated in Table 1. The ANN model was developed to predict the MRR and Ra for all combination levels of the input parameters. The neural network was simulated with 6050 the data set. After training, a list of 50 optimized input-output parameter combinations was obtained through ANN and is presented in Table. 5. Table 5 indicates the output parameter, the MRR in decreasing order and corresponding Ra at 50 optimized input parameter combinations. It also helps to select the input parameter combination at the required MRR.

Table 3. Error for MRR

Error	Training data	Validation data	Testing data
MAE	0.580003721	2.421624627	0.827826794
MPE	7.626796553	16.92452563	9.800317507

Table 4. Error for Ra

Error	Training data	Validation data	Testing data
MAE	0.864459133	0.849570064	0.815860784
MPE	12.1634995	14.11580632	10.8702371

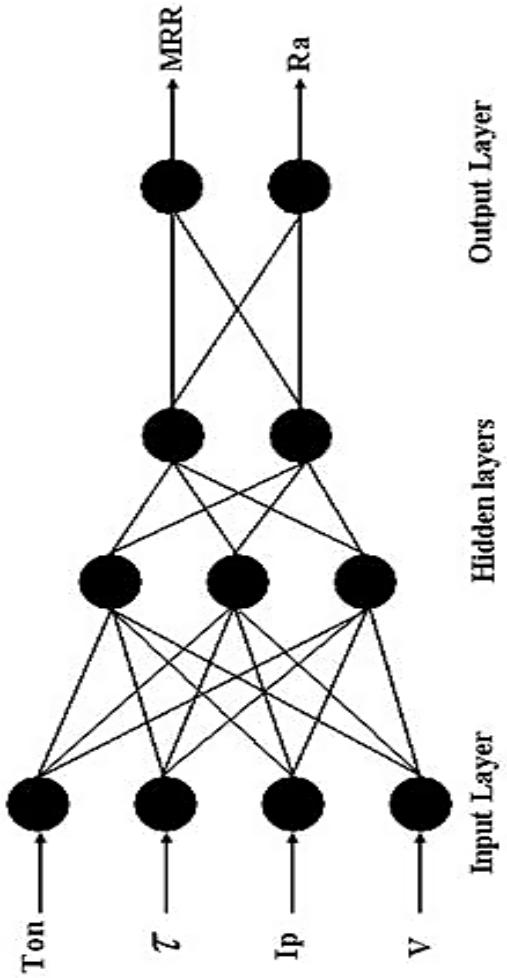

Figure 3. BPNN for prediction of MRR and Ra

Table 5. Sorted out list of optimum input-output parameter combinations

Sl. No.	*Ip* A	*Ton* µs	*Tau*	*V*	MRR mm^3/min	Ra µm
1	15	100	50	40	51.59	10.47
2	15	100	50	41	51.51	10.43
3	15	100	50	42	51.43	10.40
4	15	100	50	43	51.34	10.36
5	15	100	50	44	51.25	10.32
6	15	100	50	45	51.15	10.27
7	15	100	50	46	51.04	10.23
8	15	95	50	40	50.94	10.51
9	15	100	50	47	50.92	10.18
10	15	95	50	41	50.87	10.48
11	15	100	50	48	50.80	10.13
12	15	95	50	42	50.80	10.44
13	15	95	50	43	50.72	10.41
14	15	100	50	49	50.67	10.07
15	15	95	50	44	50.64	10.37
16	15	95	50	45	50.55	10.33
17	15	100	50	50	50.54	10.01
18	15	95	50	46	50.45	10.28
19	15	95	50	47	50.35	10.24
20	15	95	50	48	50.24	10.19
21	15	95	50	49	50.13	10.13
22	15	90	50	40	50.07	10.55
23	15	90	50	41	50.01	10.52
24	15	95	50	50	50.01	10.08
25	15	90	50	42	49.95	10.48
26	15	90	50	43	49.88	10.45
27	15	90	50	44	49.81	10.41
28	15	90	50	45	49.73	10.38
29	15	90	50	46	49.65	10.34
30	15	90	50	47	49.56	10.29
31	15	90	50	48	49.47	10.24
32	15	90	50	49	49.36	10.19
33	15	90	50	50	49.26	10.14
34	15	85	50	40	48.93	10.58
35	15	85	50	41	48.89	10.56
36	15	85	50	42	48.84	10.53
37	15	85	50	43	48.78	10.49
38	15	85	50	44	48.72	10.46
39	15	85	50	45	48.66	10.43
40	14	100	50	40	48.63	10.08
41	15	85	50	46	48.59	10.39
42	15	85	50	47	48.51	10.35
43	14	100	50	41	48.50	10.02
44	15	85	50	48	48.43	10.30
45	14	100	50	42	48.36	9.96
46	15	85	50	49	48.34	10.25
47	15	85	50	50	48.25	10.20
48	14	100	50	43	48.21	9.89
49	14	100	50	44	48.05	9.82
50	14	100	50	45	47.89	9.75

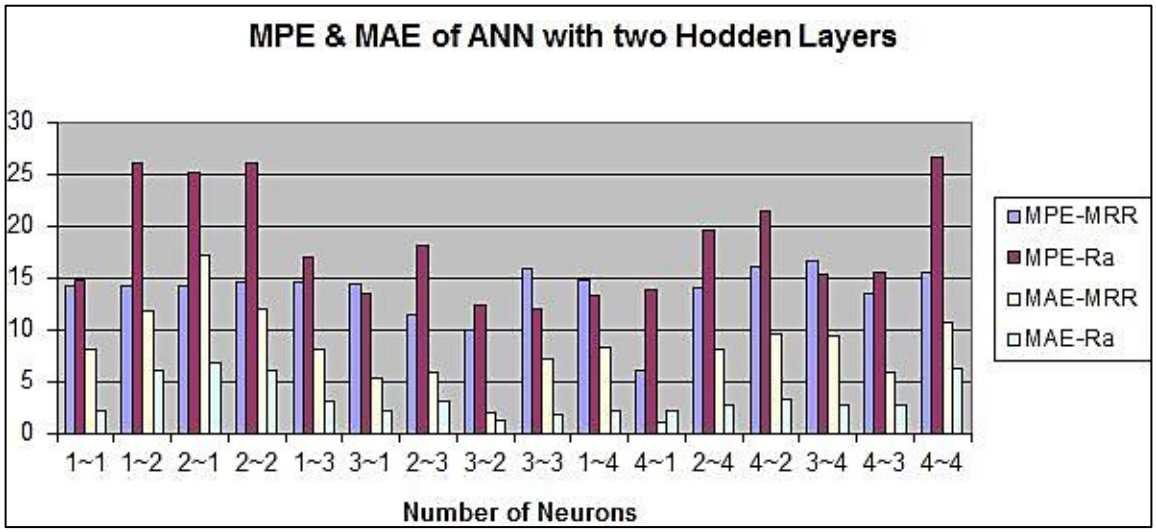

Figure 4. MPE & MAE of ANN with Single Hidden Layer

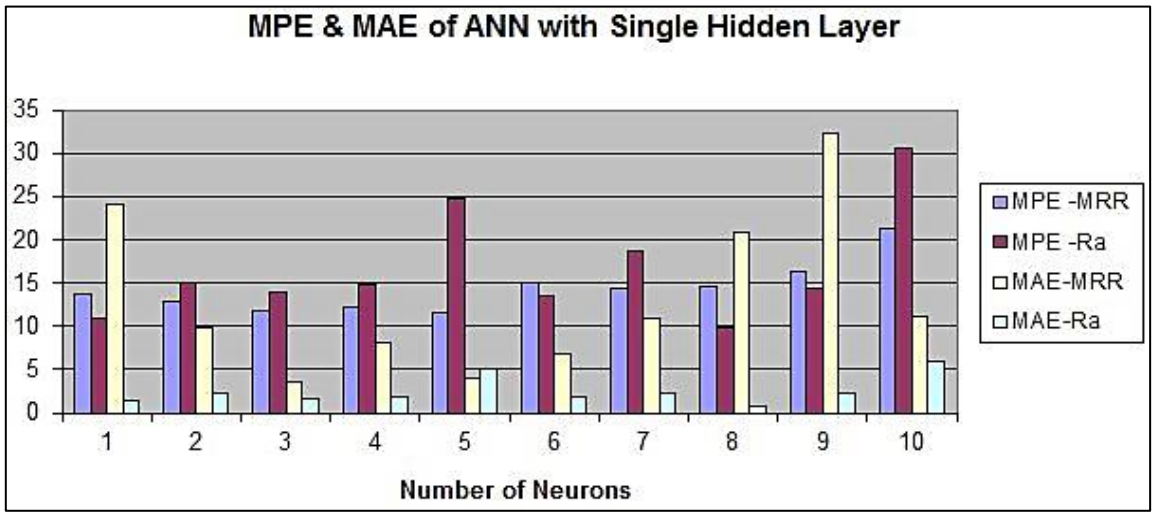

Figure 5. MPE & MAE of ANN with Two Hidden Layer

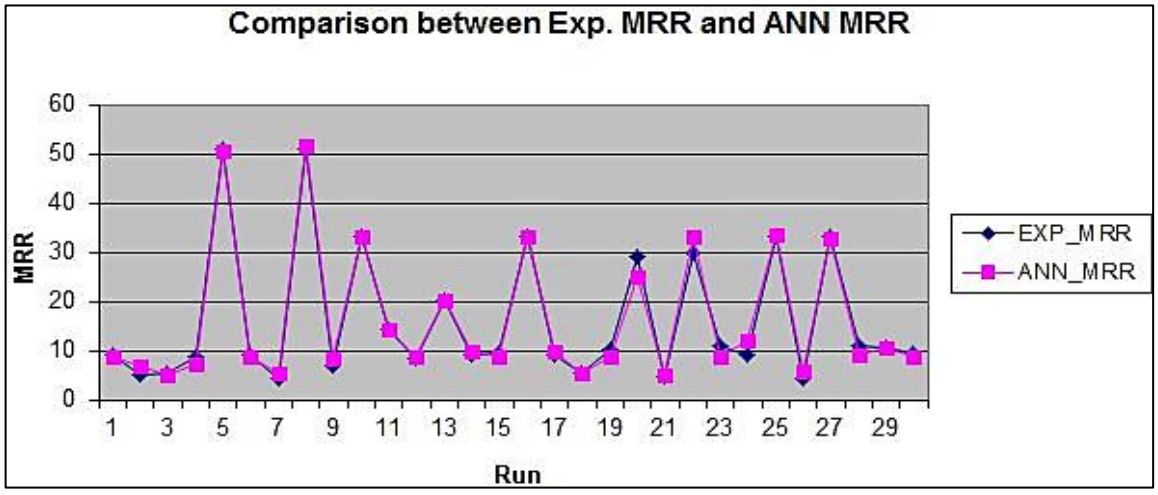

Figure 6. Comparison between Exp. MRR and ANN MRR

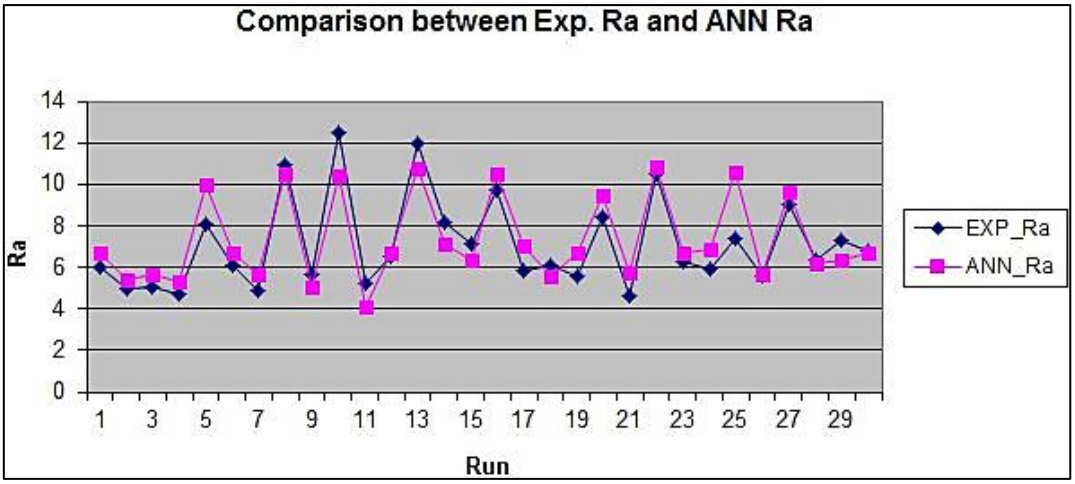

Figure 7. Comparison between Exp. Ra and ANN Ra

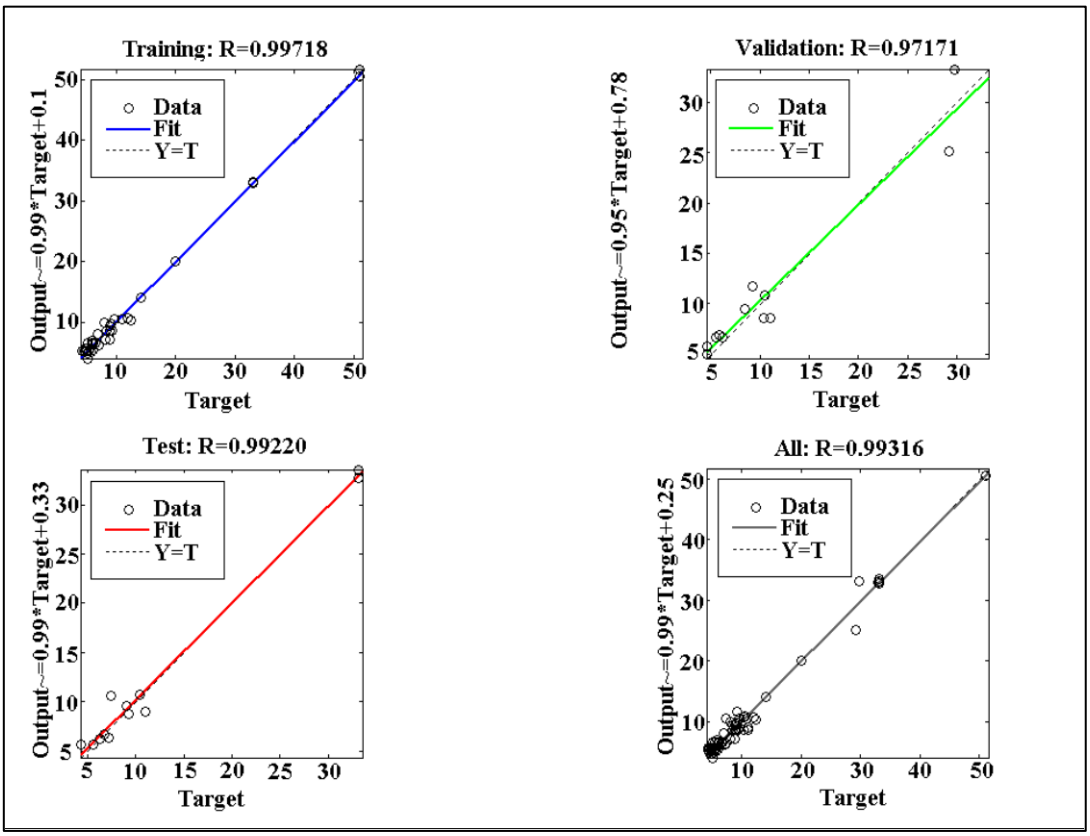

Figure 8. Compression between Target and Output of ANN

7. Discussions

The present work proposes a methodology to determine the optimal combination of control parameters in the EDM process using D2 steel. The ANN model was applied to predict the process performance. It is always a difficult task to find an optimal configuration of BPNN. There is no exact rule for setting the proper number of neurons in a hidden layer to avoid over-fitting or under-fitting to make the learning phase convergent. For the best performance of the BPNN, the proper number of nodes in the hidden layer is selected through a trial and error method based on the number of epochs needed to train the network. It is compared with the results obtained from the experiments and the average absolute error obtained for the network. For the input data, the BPNN has almost an identical generalization ability. A BPNN was developed to model the process parameters. Optimal process parameter combinations, corresponding to different MRR and Ra, were determined out of 6050 possible combinations. The presented list of 50 optimum parameter combinations can act as guidelines for effective and efficient machining of D2 steel using EDM process. Through an optimized input data set, the improved output results will enhance the productivity with a better machining surface quality.

Furthermore, the production cost and machining time will be saved through the optimum machining speed in every run. This work in the area of machining D2 steel, through EDM process and ANN application, will solve various challenging problems faced by the engineers and technocrats in the field of modern manufacturing systems. Present manufacturing industries can achieve the ultimate goals of higher productivity (higher MRR), better quality (required surface finish) and lower production cost (reduced material removal time), which would help manufacturers to compete in the world market.

8. Conclusion

The present research paper provides an effective and a novel approach for modelling and the optimisation of the machining conditions of EDM process for attaining the maximum material removal rate and the minimum surface roughness. The extensive experiments were carried out initially and were simulated to generate a huge data. The different parametric combination was used to generate the experimental data. After training, a list of optimized input-output parameter combinations was obtained through ANN and presented. This attempt provides an optimized input data set to EDM system and the results show an improvement, with a better productivity, a reduced material removal time and a product cost at the desired surface finish. The optimised value of the present research is found to be 51.588 mm^3/min with a level of surface finish of 0.0955 µm.

References

[1] Abbas, Norliana Mohd, Darius G. Solomon, and Md Fuad Bahari, "A review on current research trends in electrical discharge machining (EDM)". International Journal of machine tools and Manufacture, Vol. 47 (2007) No.7, 1214-1228.

[2] Ho, K. H., and S. T. Newman, "State of the art electrical discharge machining (EDM)." International Journal of Machine Tools and Manufacture, Vol. 43 (2003) No. 13, 1287-1300.

[3] M. K. Pradhan, "Experimental investigation and modelling of surface integrity, accuracy and productivity aspects in EDM of AISI D2 steel". Ph.D. Dissertation. 2010.

[4] Pradhan, M. K., and C. K. Biswas. "Neuro-fuzzy model on material removal rate in electrical discharge machining in AISI D2 steel." *Proceedings of the 2nd International and 23rd All India Manufacturing Technology, Design and Research Conference*, IIT Madras, India, 2008.

[5] Assarzadeh, S., and M. Ghoreishi. "Neural-network-based modelling and optimization of the electro-discharge machining process". The International Journal of Advanced Manufacturing Technology, Vol. 39 (2008) No.5-6, 488-500.

[6] D. Mandal, S. K. Pal, and P. Saha, "Modeling of electrical discharge machining process using back propagation neural network and multi-objective optimization using non-dominating sorting genetic algorithm-II". Journal of Materials Processing Technology, Vol. 186(2007) No.1, 154-162.

[7] M. K. Pradhan and C. K. Biswas "Neuro-fuzzy and neural network-based prediction of various responses in electrical discharge machining of AISI D2 steel", The International Journal of Advanced Manufacturing Technology", Vol 50 (2010) No.5-8, 591-610.

[8] D. K. Panda and R. K. Bhoi, Panda, "Artificial neural network prediction of material removal rate in electro discharge machining". Materials and Manufacturing Processes, Vol. 20(2005) No.4, 645-672.

[9] Gopal and K. Rajurkar, "Artificial neural network approach in modeling of EDM process". Proceedings of Artificial Neural Networks in Engineering (ANNIE'92) Conference, St. Louis, Missouri, USA, 1992.

[10] K. S. Sangwan, S. Saxena, and G. Kant, "Optimization of Machining Parameters to Minimize Surface Roughness using Integrated ANN-GA Approach." Procedia CIRP, Vol. 29 (2015), 305-310.

[11] Markopoulos, Angelos P., Dimitrios E. Manolakos, and Nikolaos M. Vaxevanidis. "Artificial neural network models for the prediction of surface roughness in electrical discharge machining." Journal of Intelligent Manufacturing, Vol. 19 (2008) No.3, 283-292.

[12] M.K. Pradhan, R. Das, and C. K. Biswas, "Comparisons of neural network models on surface roughness in electrical discharge machining." Proceedings of the Institution of Mechanical Engineers, Part B: Journal of Engineering Manufacture, Vol. 223(2009) No.7, 801-808.

[13] S. Shakeri, A. Ghassemi, M. Hassani, and A. Hajian, Shakeri, Saeid, et al., "Investigation of material removal rate and surface roughness in wire electrical discharge machining process for cementation alloy steel using artificial neural network." The International Journal of Advanced Manufacturing Technology , (2015), 1-9.(In press)

[14] J. Sahu, S. S. Mahapatra, and C. P. Mohanty, "Multi–response optimisation of EDM parameters using data envelopment analysis". International Journal of Productivity and Quality Management, Vol. 15 (2015) No.3, 309-334.

[15] S. S. Baraskar, S. Banwait, and S. Laroiya, "Multi-objective optimization of electrical discharge machining process using a hybrid method. "Materials and Manufacturing Processes, Vol. 28(2013) No.4, 348-354.

[16] S. Joshi and S. Pande "Intelligent process modeling and optimization of die-sinking electric discharge machining". Applied Soft Computing, Vol. 11 (2011) No.2, 2743-2755.

[17] R. N. Yadav and V. Yadava,"Multi objective optimization of slotted electrical discharge abrasive grinding of metal matrix composite using artificial neural network and non-dominated sorting genetic algorithm." Proceedings of the Institution of Mechanical Engineers, Part B: Journal of Engineering Manufacture Vol. 227 (2013) No. 10, 1442-1452

[18] R. Das, M K Pradhan and C. Das, Prediction of surface roughness in Electrical Discharge Machining of SKD 11 TOOL steel using Recurrent Elman Networks, Jordan Journal of Mechanical and Industrial Engineering, Vol.7, (2013) No.1, pp:97-104.

JJMIE

Volume 10 Number 1, March.2016
ISSN 1995-6665
Pages 19- 26

Jordan Journal of Mechanical and Industrial Engineering

The Effect of Adding Different Percentages of Manganese (Mn) and Copper (Cu) on the Mechanical Behavior of Aluminum

Lina M. Shehadeh[1] , Issam S. Jalham[2 *]

[1] MSc student Industrial Engineering Dept, University of Jordan, Amman 11942 Jordan
[2] Professor in the Industrial Engineering Dept, University of Jordan, Amman 11942 Jordan.

Received 11 May 2015 Accepted 1 Oct 2015

Abstract

In the present investigation, aluminum cast alloys were produced, age hardened, and tested after adding a varying manganese content (from 0.1to 0.5%) and Cu content from (1.5-7%) with constant Mg-Si-Fe composition and Al as the dominant constituent. Results showed that the addition of Mn to the alloy increased the tensile properties and hardness up to 0.6 percent for both the as-cast and age-hardened conditions, while their impact energies decreased. On the other hand, the addition of Cu to the alloy increased the tensile and hardness properties and decreased the impact energy.

Keywords: *Hardness, Artificial Hardening, Impact, Toughness, Tensile*.

1. Introduction

Aluminum alloys are widely used in the production of automotive components, buildings and constructions, containers and packaging, marine, aviation, aerospace and electrical industries because of their light weights, corrosion resistance in most environments or combination of these properties. Aluminum based alloys also have a high thermal conductivity and a low coefficient of linear expansion values, and, based on these two properties, they can be forged to the desired shapes at elevated temperatures and then solution treated and aged hardened to obtain desired microstructures and excellent mechanical properties [1,2]. All alloying elements that are used for aluminum alloy design can be classified into three principal groups: basic alloying elements, ancillary additions (or dopants), and impurities. Depending on the nature of an alloy, the same elements could play different roles. The widely used elements to improve the properties of Aluminum alloys are magnesium, zinc, copper; and silicon. These chemical elements are called "basic'', or "principal'', because they are introduced into aluminum alloys in (relatively) large amounts and define their microstructure and properties. When added to Al–Mg alloys, Mn generally combines with Al, Si (and Fe) during ingot preheating or homogenization to form sub-micron sized, semi-coherent or incoherent dispersions. The level of Mn also affects the type, size and volume fraction of the coarse constituent, Fe-containing, particles. Additions of Fe and Si also affect the type, size and volume fraction of the coarse constituent particles, and increasing levels of both elements were shown to be detrimental to O-temper sheet formability, through their effect on increasing the size and volume fraction of these particles [3].

Copper is added to Al mainly to increase strength. As the Cu content increases, there is a continuous increase in hardness, but strength and especially ductility depend on how the Cu is distributed. Manganese is added to most commercial Al-Cu alloys. It forms Al_{20} Cu_2 Mn_3 dispersion particles which provide some dispersion strengthening, and also serve to nucleate precipitates during aging on dislocations which emanate from the particle matrix interface during quenching. Si increases fluidability and resistance to hot cracking during casting, even though Fe reduces hot cracking in Al-Cu alloys. But both Fe and Si can form constituent phases (e.g., Al_7Cu_2Fe and Mg_2Si) which reduce fracture toughness [4].

A lot of studies were conducted on aluminum and its alloys. Most of the studies aimed at discovering its mechanical, and other, properties. The change of the composition was one of the areas which were taken into consideration. Many researchers concentrated on the change of manganese content on the properties of Al alloys or on the change of the content of copper or other elements. The interaction of the change of the percentages of these two elements (Mn and Cu) together on the properties of Al was not considered. As these elements have a considerable effect on the properties of Al alloys, it was decided to study the influence of adding different percentages of Mn and Cu together on the mechanical properties of Aluminum to bring a clear picture of the effect of the interaction of different percentages of Mn and Cu on the mechanical properties of Aluminum.

* Corresponding author e-mail: jalham@ju.edu.jo.

2. Literature Review

In this section, some of the research contribution will be discussed. The main focus of this survey will be the mechanical properties of aluminum such as tensile, hardness and impact properties.

Various alloying elements are added to aluminum to enhance its mechanical properties. Copper has been the most common alloying element almost since the beginning of the aluminum industry, and a variety of alloys in which copper is the major addition were developed. Magnesium (Mg) used to strengthen and harden aluminum castings. Nafsin N. and Rashed H. M. M. A. [5] emphasized the establishment of a relationship between microstructureand cold deformation behavior of aluminum-copper magnesium alloys. Aluminum-copper-magnesium alloys with varying Cu% and Mg% were casted and their chemical compositions were determined using Optical Emission Spectroscopy (OES). These alloys underwent cold deformation after homogenization and their microstructures were examined using optical microscope. Finally, the effects of deformations were studied by measuring the hardness of those alloys. The microstructure and mechanical properties of Al–14.5 Si – 0.5 Mg alloy by the addition of different percentages of Cu, mainly 4.65 wt.% and 0.52 wt.% were studied by Chih-Ting Wu *et al* [6]. After examining the microstructure, they concluded that an acicular Al_5FeSi was found in the high-Cu content alloy while in the low-Cu content alloy, $Al_8Mg_3FeSi_6$ was found in the Fe-bearing phase. Furthermore, tensile testing indicated that the low-Cu alloy containing $Al_8Mg_3FeSi_6$ had higher Ultimate Tensile Strength (UTS) and elongation than the high-Cu alloy containing the acicular Al_5FeSi. On the other hand, it was believed that the presence of the acicular_Al_5FeSi in the high-Cu alloy is responsible for the increased number of crack initiators and brittleness of the alloy. This also indicated that the hardness of the high-Cu alloy exceeded that of low-Cu alloy.

Nine Al–(1–3)Mg–(0–0.4)Cu–0.15Si–0.25Mn (in wt.%) alloys with potential applications in both packaging and automotive industries were investigated by Zhu *et al.* [7]. The results of their tensile testing showed that the solution strengthening is, in good approximation, linearly proportional to the Mg content. Mechanical testing and microstructural examinations of aged samples indicate that Mg_2Si phase precipitates contribute to age hardening of Cu-free alloys whilst both Mg_2Si phase and (Al_2CuMg) phases contribute to that of Cu-containing alloys. The age hardening capability is critically influenced by solution treatment temperature. Increasing the solution treatment temperature from 500 to 550°C results in a marked increase in rate of hardening for Cu-containing alloys and solution treatment at about 550°C or higher is needed to allow Mg_2Si phase precipitation during ageing in Cu-free alloys with Mg content of about 2% or higher.

Yield strength of an Al–3.7Cu–1.5Li–0.50Zn–0.37Mg–0.30Mn–0.14Zr alloy aged at 165°C as a function of time was examined by Hongying Li *et al*. [8]. Existing phases in this alloy were identified by selected area electron diffraction analysis and the microstructural evolution was examined by Transmission Electron Microscopy (TEM). It was found that the peak ageing time determined is 50 h leads to a yield strength of 453 MPa. The strength of the alloy increases rapidly during the 24 h of ageing and an additional strengthening was obtained for further ageing up to 50 h due to evolution of T1 and plates.

Mechanical properties of age-hardened Al alloys consisting of a varying manganese content with a constant Si-Fe composition were studied by Abdulwahab [1]. He concluded that the addition of Mn to the alloy increased the tensile properties and the hardness subject to 0.4 percent for both the as-cast and age-hardened conditions. Moreover, he concluded that the addition of Mn to the alloy decreases the impact energies for the age-hardened samples. On the other hand, Hwang *et al*. [9] studied the effect of Mn (Mn content is increased up to 0.65 wt%) on the microstructure and mechanical properties of Type 319 (Al–7wt.%Si–3.8wt.%Cu–0.5wt.%Fe) aluminum casting alloys. They found that the plate-like inter-metallic phase is completely converted to the Chinese script phase resulting in improved tensile properties. Excess amounts of Mn, however, deteriorate the mechanical properties by increasing the total amount of iron-containing inter-metallic phases. The porosity and volume percent of inter-metallic phases are correlated with the tensile properties in order to determine the role of Mn on Type 319 casting alloys.

The effects of individual and combined additions of Be, Mn, Ca and Sr on the solidification, structure and mechanical properties of Al–7Si–0.3Mg–0.8Fe alloy were investigated by Kumari *et al*. [10]. Their thermal analysis revealed that all additions, except for Be, show a peak corresponding to β-Fe intermetallic phase formation and the eutectic temperature decreased after the addition of Ca and Sr by 6.6 and 8.7 K, respectively, compared to the untreated alloy and lead to modification of eutectic Si from platelet to fibrous form. The peak corresponding to Be–Fe phase has been identified by DTA. Mn (0.4%) and Be (0.2%) additions to Al–7Si–0.3Mg–0.8Fe alloy change the morphology of platelet β-phase to script form leading to significant improvement in tensile . In another work, Ma *et al*. [11] studied the effect of-iron intermetallics and porosity on the tensile properties in cast Al–Si–Cu and Al–Si–Mg alloys. The results showed that the alloy ductility and UTS were subject to deterioration as a result of an increase in the size of iron intermetallics. An increase in the size of the porosity was also deleterious to alloy ductility and UTS. The co-addition of Re, Mn and Fe proves to be an effective method to enhance the high-temperature strength of A390. The high-temperature strength of A390 is increased by 25% in this article using this method. Moreover, they investigated the effects of the cooling rate, heat treatment as well as additions of Mn and Sr on hardness and hardening characteristics in Al–11Si–2.5Cu–Mg alloys. The results of scanning electron microscopy reveal that the age-hardening behavior is related to the precipitation sequence of alloy. An energy dispersive spectroscopy analysis was used to identify the precipitated phases. The results also show that the hardness of the solution heat-treated samples is higher in air-cooled alloys than in furnace cooled ones. Furthermore, the hardness observed in solution heat-treated samples is higher than in those of the cast samples for air-cooled alloys, with the highest hardness level in the non-modified alloys. The highest hardness levels, among the artificially

aged samples, were observed in the non-modified, air-cooled alloys. These levels occur after aging for longer times at lower temperatures (e.g., 30 h at 155°C). The alloys studied did not display any softening after 44 h at 155° C, whereas at 180°C, softening was noted to occur after 10–15 h. At short aging times of 5–10 h, high hardness values may be obtained by aging at180°C. At aging temperatures of 200°C, 220° C and 240°C, softening began after 2 h had elapsed.

The influence of Cu content on the ageing behavior of Al–8Si–0.4Mg–xCu alloys was investigated by Zhang *et al.* [12]. They conducted hardness measurement, Differential Scanning Calorimeter (DSC) and Transmission Electron Microscopy (TEM) analysis for Al–8Si–0.4Mg–xCu alloys with 1 wt%Cu, 2 wt%Cu, 3 wt%Cu, and 4 wt%Cu produced in permanent molds. Hardness has been estimated for ageing times varying from 1 h to 100 h. The results indicate that the maximum hardness increases clearly with the increase of Cu content, but the total increase in hardness during ageing (DHVmax) decreases with the addition of 1 wt%Cu and has a little increase with Cu content from 1 wt% to 4 wt%. In other words, the addition of Cu decreases the age hardening rate.

The addition of Cu to Al alloys were also investigated. For example, Basavakumar *et al*. [13] studied the microstructures and impact toughness of Al–7Si and Al–7Si–2-5Cu cast alloys after various melt treatments like grain refinement and modification. The results indicate that the combined grain refined and modified Al–7Si–2 5Cu alloys have microstructures consisting of uniformly distributed -Al grains, interdendritic network of fine eutectic silicon and fine $CuAl_2$ particles in the interdendritic region. These alloys exhibited an improved impact toughness as cast condition when compared to those treated by individual addition of grain refiner or modifier. The improved impact toughness of Al–7Si–2 5Cu alloys are related to breakage of the large aluminum grains and uniform distribution of eutectic silicon and fine $CuAl_2$ particles in the interdendritic region resulting from combined refinement and modification. The present paper attempts to investigate the influence of microstructural changes in the Al–7Si and Al–7Si–2 5Cu cast alloys by grain refinement, modification and combined action of both on the impact toughness.

The effect of copper and silicon content on the mechanical properties in Al–Cu–Si–Mg alloys was studied by Muzaffer Zeren [14]. Al–Cu–Si–Mg alloys with 1, 3, 4.5, 6% Cu and 0, 5, 7, 12, 18% Si were utilized for this purpose. After melting and Na modification, alloys were cast in metal molds at 780°C and solidified. They were solution treated at 490°C for 4 h and then quenched. Samples were aged at 180°C for 5, 10, 15, 20 h to observe the effect of aging on mechanical properties. While in their work [15], Muzaffer and others studied the influence of Cu content on the microstructure and hardness of near-eutectic Al-Si-*x*Cu (x = 2%, 3%, 4% and 5%). After melting Al-based alloys with different Cu contents, alloys were cast in green sand molds at 690°C and solidified. The solution treatment was performed at 500°C for 7 h and then the specimens were cooled by water quenching. The samples were respectively aged at 190°C for 5, 10 and 15 h to observe the effect of aging time on the hardness of matrix. Also differential thermal analysis was used to obtain the transition temperature of the equilibrium phases at cooling rate of 30 K/min and to determine the effect of Cu content on the formation of quaternary eutectic phases and the melting point of α(Al) + Si. The results showed that as Cu content in the alloy increases, the hardness of matrix increases due to precipitation hardening. On the other hand, factors necessary to obtain an optimal heat treatment that influence the hardness and resistivity of Al-6Si-0.5Mg casting alloys with Cu or/and Ni additions were investigated by Hossain A. *et al.* [16]. The alloys were homogenized (24hr at 500°C), solutionized (2hr at 540°C) and artificially ageing at various times and temperatures. The alloys were aged isochronally for 60 minutes at temperatures up to 400°C and isothermally at 150, 175, 200, 225, 250 & 300°C for different periods in the range 15 to 360 minutes. The hardness and electrical resistivity of the alloys were measured for various artificial ageing times and temperatures. From the isochronal ageing treatment, hardness found maximum ageing at 225°C. And from the isothermal ageing treatment, hardness found maximum for 60 minutes at 225°C. So the optimal heat treatment consists of 60 minutes ageing at 225°C. It is worth mentioning that Nurul Razliana Abdul Razak *et al.* [17] studied Effect of Aluminum Addition on Microstructure and Microhardness of Sn-0.7 Cu-xAl Lead-free Alloy. They found that the microhardness was improved by 19% as the weight percentage of Al particls was increased up to 1.0%.

Unlike the works mentioned above, the present investigation differs in that it studies the effect of the interaction of different percentages of Mn and Cu on the mechanical properties of Aluminum.

3. Materials, Equipments and Experimental Procedure

3.1. Materials

Materials that are used in the present investigation are: commercially pure Aluminum (its composition is shown in Table 1), pure Copper and pure Manganese as a master alloy, and etching agent of the following composition: (0.5% HF, 2.5%HCL, 1.5%HNO_3).

Table 1. Chemical compositions of commercially pure aluminum

Elements	Al	Mg	Si	Fe
Percentage (%)	94.45	1.06	1.2	3.29

The composition of alloys which were manufactured and tested in the present study is shown in Table 2.

3.2. Equipment

Equipment used in the present study are: Electrical Resistance Furnace of EAFt Type, graphite crucible, permanent brass mold in the form of cylindrical castings (size: 15mm in diameter, 150 mm long), BUEHLER Type grinder/Polisher machine to prepare the samples to microstructural examination, MEIJI Type optical microscope to reveal the microstructure, Aleitz-Amr 1000 Type scanning electron microscope to determine the chemical composition of the alloys, computerized SHIMADZU Type electro hydraulic servo universal testing machine to determine the tensile properties, digital

An MVK-11, MITUTOYO Type micro hardness Vickers tester to determine the hardness properties, and PIT-C Metal Type pendulum Charpy Impact Testing Machine to determine the impact properties.

Table 2. Chemical compositions of manufactured Al-base alloys.

Alloy No.	Elements (wt. %)		
	Cu	Mn	Al
1	1.5	0.2	Balance
2	1.5	0.4	Balance
3	1.5	0.6	Balance
4	1.5	0.8	Balance
5	1.5	1	Balance
6	3	0.2	Balance
7	3	0.4	Balance
8	3	0.6	Balance
9	3	0.8	Balance
10	3	1	Balance
11	4.5	0.2	Balance
12	4.5	0.4	Balance
13	4.5	0.6	Balance
14	4.5	0.8	Balance
15	4.5	1	Balance
16	6	0.2	Balance
17	6	0.4	Balance
18	6	0.6	Balance
19	6	0.8	Balance
20	6	1	Balance
21	7.5	0.2	Balance
22	7.5	0.4	Balance
23	7.5	0.6	Balance
24	7.5	0.8	Balance
25	7.5	1	Balance

3.3. Experimental Procedure

The experimental procedure used in the present project comprises three stages: manufacturing, microstructural examination, and testing. In the manufacturing stage, twenty five alloys were prepared by melting commercially pure aluminum in an electrical resistance furnace using a graphite crucible. Copper with a range between (1.5-7%), and Mn with a range between (0.2-1%) were sequentially added to the melt to produce alloys with the compositions shown in Table (2) above. Then the melt was poured into permanent brass mold.

Specimens with Cu percentages less than 6 %, which were numbered (1-15), were solution heat treated at 488°C for 8 h, quenched into warm water (70°C) and then aged to a T6 condition at 193°C for 8 h (artificial age-hardening).

To conduct the microstructural examination, samples were ground and polished by using grinder/polisher machine. The polished samples were etched using etching agent of (0.5% HF, 2.5% HCL, 1.5 % HNO_3) composition. The etched alloys were examined by using optical microscope at different magnification and scanning electron microscope.

Tensile, hardness, and impact tests were also conducted using the UTM and pendulum type Charpy testing machine. To accomplish the tensile test, specimens with 15 mm diameter, 45 mm length were prepared and subjected to the test to get the stress strain behavior.

To perform Vickers hardness test, specimens with 15 mm diameter, 15mm length were prepared, ground and polished. At least 5 impressions were made to determine the mean value of the hardness at different locations.

At the end, Charpy impact test was conducted using a standard V-notch impact samples having the dimensions of 10x10x55 mm which are prepared according to ASTM E 23 by using the Charpy impact testing machine.

4. Results and Discussions

4.1. Microstructural Observations

In this section, the influence of the addition of Mn and Cu to the microstructure of Aluminum is investigated. The microstructure of the tested samples was revealed using optical microscope and scanning electron microscope. It was found that α-Al solid solution is the predominant phase in the microstructure of these alloys (Figure 1). It forms dendritic network, and also precipitate in several multiphase eutectic reactions. This in agreement with Muzaffer *et al.* [16].

During the solution heat treatment, most of eutectic Al_2Cu and intermetallic particles dissolve into the Al matrix in the low- Cu alloy. So Al_2Cu was not observed clearly by using optical microscope but the EDS detector on SEM identifies the presence of this phase. This can be seen by the EDS detector spectra analysis (shown in Table 3).

The addition of Mn with percentage between 0.1&0.6 transforms the β- Al_5FeSi into α- Al_5FeSi, increasing the amount of Mn to (0.8 &1)% results in the formation of polyhedral α-Al_5FeSi, as shown in Figure 2. These results are in agreement with J.Y. Hwang H.W [?]. The increase in Mn and Cu content affects the size of the dendritic arm spacing (SDAS). The size of SDAS was calculated by measuring the distance between adjacent side branches on the longitudinal section of primary dendritic as a function of distance from the dendritic tip, following the method described by Muzaffer Z. [15]. Figure (3) shows the results of these calculated values. It is clear from the figure that the size of SDAS decreases until 0.6% μm and start increasing after that; this is explained in Figure 2.

In non-heat treated alloys, optical microscope reveals all phases clearly for specimens contain a high percentage of Cu. EDS results, shown in Table 4, supports these results.

The addition of Mn with percentage between 0.1&0.6 transforms the β- Al_5FeSi into α- Al_5FeSi, increasing the amount of Mn to (0.8 &1)% results in the formation of polyhedral α-Al_5FeSi Figure 4. These results are in agreement with Hwang [13]. The increase in Mn and Cu content affects the size of the dendritic arm spacing (SDAS). The size of SDAS was calculated by measuring the distance between adjacent side branches on the longitudinal section of primary dendritic as a function of distance from the dendritic tip, following the method described by Muzaffer Z. [15]. Figure 5 shows the results of these calculated values. It is clear from the figure that the size of SDAS decreases until 0.6% μm and start increasing after that; this can be explained by Figure 4.

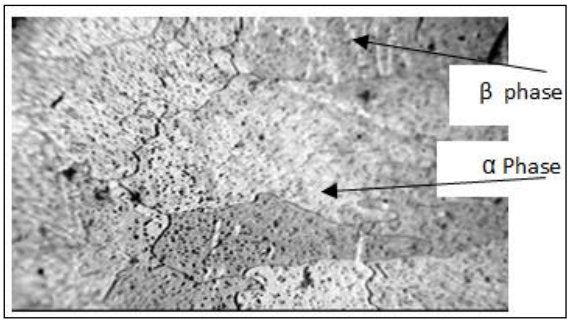

Figure 1. Optical microstructures observed in Al sample before addition Mn and Cu at magnification 250x

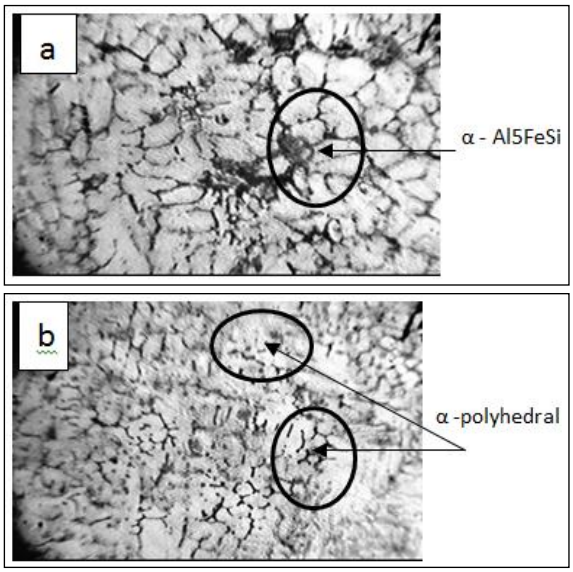

(a) Optical microstructures observed in samples (14) at magnification 400x

(b) Optical microstructures observed in samples (15) at magnification 400x

Figure 2.

Table 3: Results of EDS analysis of alloy 15.

Element	Weight%	AT%	K-Value
Al	85.993	92.262	0.75941
Si	1.988	2.050	0.00649
Mn	2.972	1.566	0.03240
Cu	9.047	4.122	0.09918

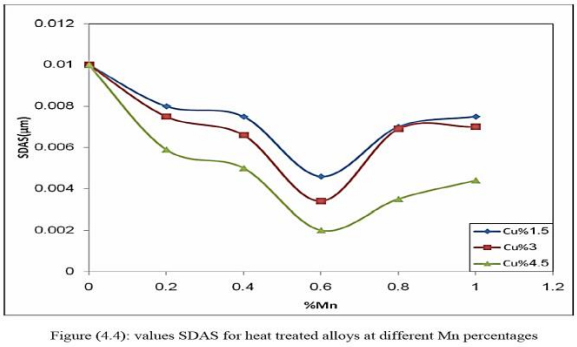

Figure (4.4): values SDAS for heat treated alloys at different Mn percentages

Figure 3. Values SDAS for heat treated alloys at different Mn percentages

Table 4. Results of EDS analysis of alloy 24.

Element	Weight%	AT%	K-Value
Mg	0.958	1.161	0.00441
Al	83.560	91.207	0.42480
Mn	1.043	0.559	0.00698
Fe	5.960	3.143	0.02972
Cu	8.479	3.930	0.05619

In non-heat treated alloys optical microscope reveals all phases clearly for specimens contain a high percentage of Cu. EDS results, shown in Table 4, supports this result. The addition of Mn with percentage between 0.1&0.6 transforms the β- Al_5FeSi into α- Al_5FeSi, increasing the amount of Mn to (0.8 &1)% results in the formation of polyhedral α-Al_5FeSi (Figure 4). These results are in agreement with Hwang *et al.* [13]. The increase in Mn and Cu content affects the size of the dendritic arm spacing SDAS. The size of SDAS was calculated by measuring the distance between adjacent side branches on the longitudinal section of primary dendritic as a function of distance from the dendritic tip, following the method described by Muzaffer Zeren [15].

Figure 5 shows the results of these calculated values. It is clear from the figure that the size of SDAS decreases until 0.6% μm and start increasing after that. This can be explained by Figure 4.

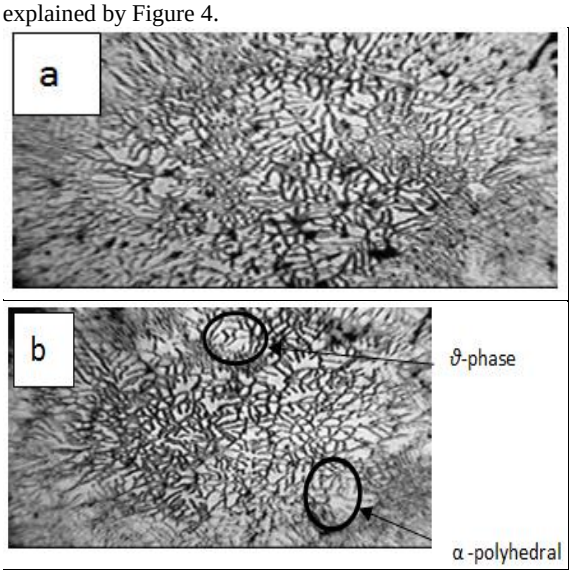

(a): Optical microstructures observed in samples (23) at magnification 250x

(b): Optical microstructures observed in samples (24) at magnification 250x

Figure 4. Results in the formation of polyhedral α-Al5FeSi

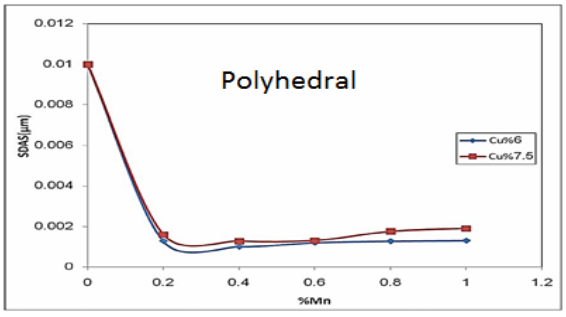

Figure 5. The values of SDAS for non-heat treated alloys at different Mn percentages

4.2. Tensile tests

True stress-strain diagram of Al alloy before adding Cu and Mn is shown in Figure 6. It is clear that the magnitude of ultimate tensile stress (UTS) of Al equal 143 Mpa.

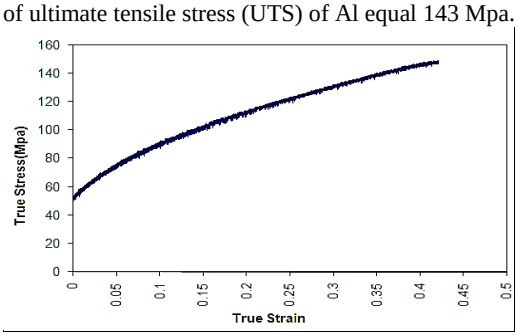

Figure 6. True stress strain diagram for pure Al

It is known that the UTM gives a load-displacement data. After getting these data, manipulation of them is needed to get the true stre;ss-true strain data. The following formula will help in this matter:

True stress $\sigma_T = P/A$ (1)

True strain $\varepsilon_T = ln(\delta / l_0) = ln[(l_f - l_0) / l_0]$ (2)

where, σ -Engineering stress, σ_T –True stress, and δ is the Change in length or difference between final (l_f) and initial length (l_0).

In the present study, UTS and elongation increased with Mn content up to 0.6 wt.%. The β phase completely converted to the Chinese script α phase by adding 0.6 wt.% Mn in sample alloys, which results in decreasing the value of UTS, as shown in Figures 7 and 8. The reason refers to the presence of the polyhedral phase (Figure 4). This result is in agreement with Hwang H.Y. *et al.* [13]. It can also be observed that the size of SDAS decreases at 0.6%Mn, and then starts increasing at (0.8 & 1)%, which leads to the increase of the UTS at 0.6% Mn and then start to decrease at 0.8 and 1 % Mn.

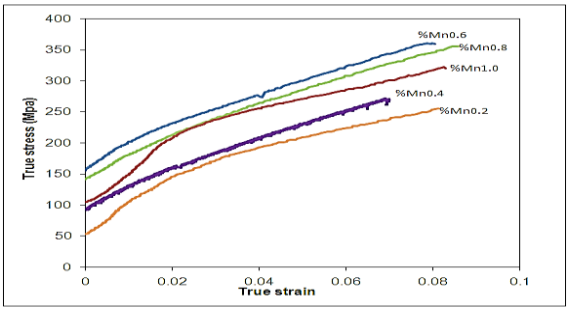

Figure 7. True stress strain diagram for alloys from (16-20) at 6wt.%Cu

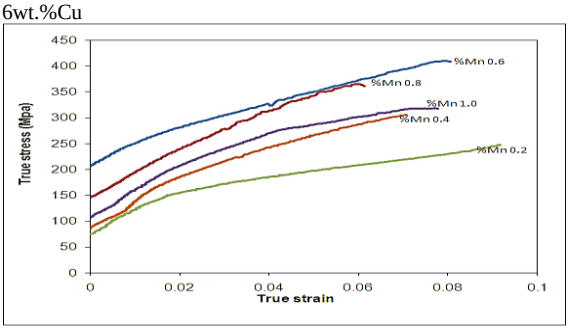

Figure 8. True stress strain diagram for alloys from (21-25) at 7.5wt.%Cu

In heat treated alloys, the tensile strength (UTS) and elongation of the 4.5% Cu alloys that contains high percentage of precipitates of dendritic structures are higher than the alloys contain a low percentages (Figures 9 to 11). The reason behind this is the solution heat treatment which resulted in dissolving back of some particles into Al matrix, yielding to solid-solution strengthening. The degree of solid-solution strengthening depends on the number of solute atoms in the Al matrix. This is in agreement with Chih-Ting [6]. Moreover, the size of SDAS decreases at 0.6%Mn, and then starts increasing at (0.8 & 1)%, which leads to increasing the UTS at 0.6% Mn and then starts to decrease at 0.8 and 1 % Mn.

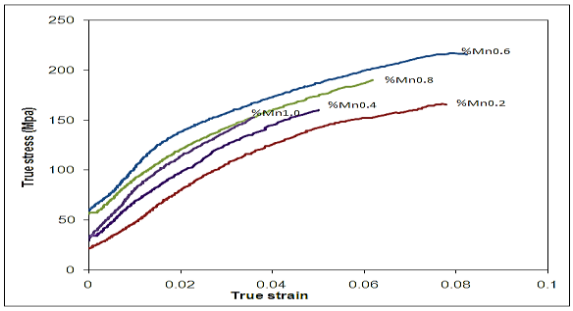

Figure 9. True stress strain diagram for alloys from (1-5) at 1.5wt.%Cu

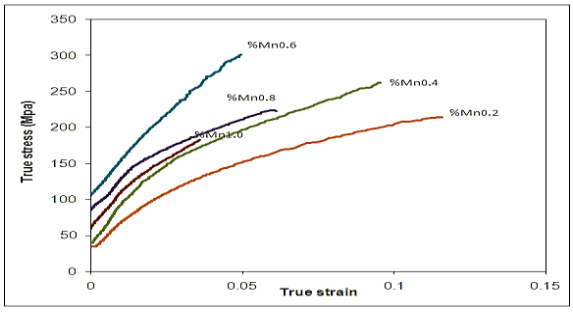

Figure 10. True stress strain diagram for alloys from (6-10) at 3wt.%Cu

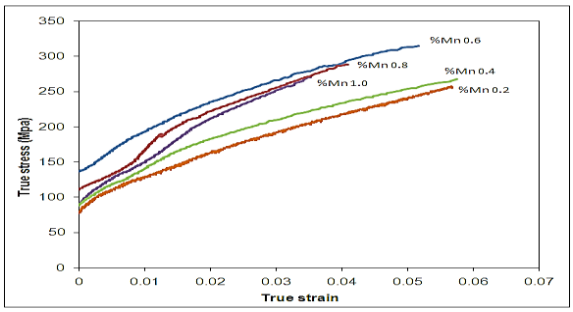

Figure 11. True stress strain diagram for alloys from (11-15) at 4.5wt.%Cu

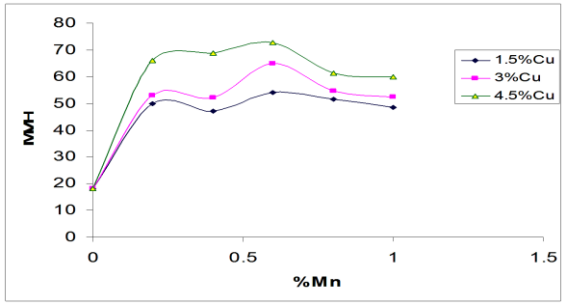

Figure 12. The relationship between the vickers hardness and % of Mn for alloy from (1-15)

4.3. Hardness test

Hardness measurements were performed on all heat-treated specimens and not heat treated alloys. The highest hardness number may be observed to correspond to highest Cu –0.6%Mn conditions. The hardening of Al-%Cu alloy is attributed to the formation of (Al_2Cu) zones, and this zone shows a higher fraction at alloy (7% Cu and 0.6% Mn). At the same time, the amount of the iron content influences the size and amount of the Chinese script α-Al15(Fe,Mn)3Si2 phase appear in the same alloy.

For the composition of 0.8 and 1 % Mn, the value of VH begins to decrease due to the presence of polyhedral α-phase. This polyhedral α phase has been described as "sludge" and has been shown to have a detrimental effect on mechanical properties. The results can be seen in Figures 12, 13 and 14.

4.4. Impact test

It has been found that Mn and Cu does not improve the impact properties at all, as shown in Figures 15, 16 and 17. This may be due to the presence of both acicular eutectic silicon and hard Mn–Fe intermetallic phases in the Mn added alloy and the distortion of the lattice during the precipitation hardening which lead to brittleness in the Cu added alloy. This result is in agreement with Kumari *et al.* [10].

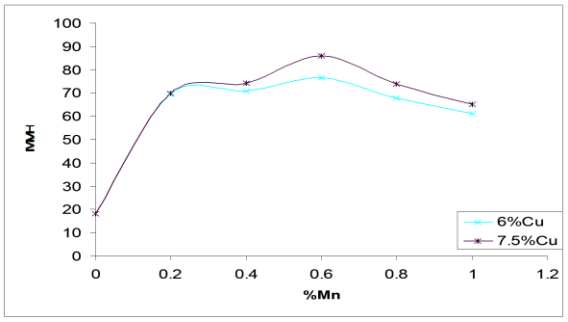

Figure 13. The relationship between the Vickers hardness and % of Mn for alloy from (16-25)

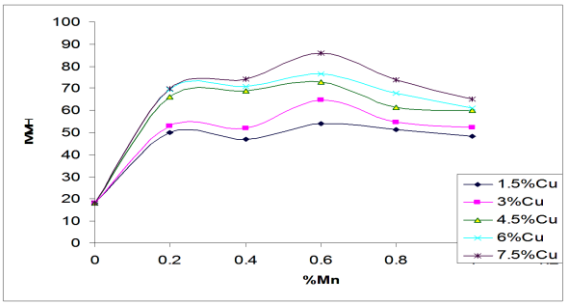

Figure 14. The relationship between the Vickers hardness and % of Mn for all alloy

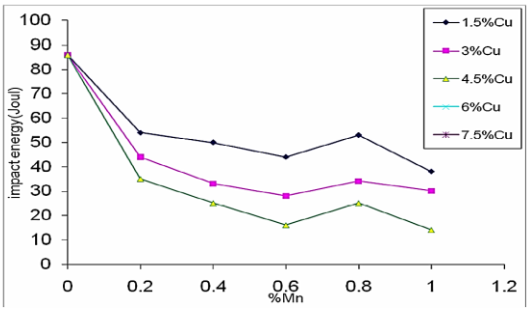

Figure (4.17): the relationship between the impact energy and %of Mn for alloy from (1-15)

Figure 15. The relationship between the impact energy and % of Mn for alloy from (1-15)

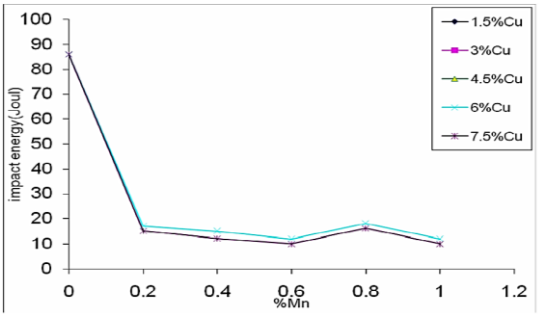

Figure (4.18): the relationship between the impact energy and %of Mn for alloy from (16-25

Figure 16. The relationship between the impact energy and % of Mn for alloy from (16-25)

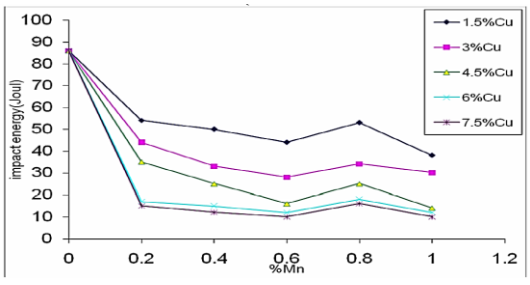

Figure (4.19): the relationship between the impact energy and %of Mn for all alloys

Figure 17. The relationship between the impact energy and % of Mn for all alloys

5. Conclusions

Referring to the results and the discussion above, the following can be concluded:

- The effect of addition of Mn on the microstructure is changing the morphology of platelet iron phase to script form at percentages from (0.2-0.6) %, and decreases the SDAS then transforms to polyhedral form at percentages (0.8-1) %, and SDAS begins to increase.
- The effect of the addition of Cu on the microstructure is the formation of Al_2Cu as a colony, and the percentage of Al_2Cu increases as the Cu content increases.
- The tensile strength (UTS) increased with the increase in Mn percentages from (0.2 to 0.6) then started decreasing after 0.6% for the heat treated alloys.
- The tensile strength (UTS) increased with the increase in Mn percentages from (0.2 to 0.6) then started decreasing after 0.6% for the non-heat treated alloys.
- The tensile strength (UTS) increased with the increase in Cu percentages for the heat treated alloys.
- The tensile strength (UTS) increased with the increase in Cu percentages for the non-heat treated alloys.
- The hardness properties (MVH) increased with the increase in Mn percentages from (0.2 to 0.6) then started decreasing after 0.6% for the heat treated alloys.
- The hardness properties (MVH) increased with the increase in Mn percentages from (0.2 to 0.6) then started decreasing after 0.6% for the non-heat treated alloys.
- The hardness properties (MVH) increased with the increase in Cu percentage for the heat treated alloys.
- The hardness properties (MVH) increased with the increase in Cu percentage for the non-heat treated alloys.
- The impact properties decreased with the increase in Mn and Cu percentages for the heat treated alloys.
- The impact properties decreased with the increase in Mn and Cu percentages for the non-heat treated alloys.

References

[1] M. Abdulwahab "Studies of the Mechanical Properties of Age-hardened Al-Si-Fe-Mn Alloy", Australian Journal of Basic and Applied Sciences, Vol. 2 (2008), No.4, 839-843.

[2] R. S. Rana; Rajesh Purohit, and S Das, "Reviews on the Influences of Alloying elements on the Microstructure and Mechanical Properties of Aluminum Alloys and Aluminum Alloy Composites", International Journal of Scientific and Research Publications, Vol. 2, (2012), No. 6, 3145-3153.

[3] D. J. Lloyd; S. A. Court, Influence of grain size on tensile properties of Al-Mg alloys, Materials Science and Technology Vol. 19, (2003), No. 10 ,1349-1354.

[4] E. *George* Totten, D. Scott MacKenzie, "*Handbook of Aluminum*: Vol. 2: Alloy Production and Materials Manufacturing", (2003).

[5] N. Nafsin and H. M. M. A. Rashed ,"Effects of Copper and Magnesium on Microstructure and Hardness of Al-Cu-Mg Alloys,International Journal of Engineering and Advanced Technology (IJEAT)", Vol. 2 (2013), No.5, 547-533.

[6] Chih-Ting Wu, Sheng-Long Lee, Meng-Hsiung Hsieh, and Jing-Chie Lin, "Effects of Cu content on microstructure and mechanical properties of Al–14.5Si–0.5Mg alloy", Materials characterization, Vol. 61 (2010), 1074–1079.

[7] Z. Zhu, M.J. Starink, " Solution strengthening and age hardening capability of Al–Mg–Mn alloys with small additions of Cu", Materials Science and Engineering A 488, (2007), 125–133.

[8] Li. Hongying ,Y i Tang, Zaide Zeng , Ziqiao Zheng , Feng Zheng, "Effect of ageing time on strength and microstructures of an Al–Cu–Li–Zn–Mg–Mn–Zr alloy", Materials Science and Engineering A ,498 , (2008), 314–320.

[9] J. Y. Hwang, H.W. Doty, M. J. Kaufman, "The effects of Mn additions on the microstructure and mechanical properties of Al–Si–Cu casting alloys", Materials Science and Engineering A 488, (2007), 496–504.

[10] S.S. Kumari, "Effects of individual and combined additions of Be, Mn, Ca and Sr on the solidification behaviour, structure and mechanical properties of Al–7Si–0.3Mg–0.8Fe alloy", Materials Science and Engineering: A, Vol. 460-461, (2007), 561-573.

[11] Z. Ma, A.M. Samuel, F.H. Samuel, H. W. Doty, S. Valtierra, "A study of tensile properties in Al–Si–Cu and Al–Si–Mg alloys: Effect of-iron intermetallics and porosity", Materials Science and Engineering A 490, (2008), 36–51.

[12] G.J. Zhang, R. H. Wang, S.P. Yuan, G. L. Scudino, J.Chen K. H. Sun, "Influence of constituents on the ductile fracture of Al–Cu–Mg alloys: Modulated by the aging treatment", Materials Science and Engineering A 526, (2009),171–176.

[13] K. G. Basavakumar, P. G. Mukunda And M. Chakraborty, "Effect of melt treatment on microstructure and impact properties of Al–7Si and Al–7Si–25Cu cast alloys", Bull. Mater. Sci., Vol. 30 (2007), No. 5, 439–445.

[14] Z. Muzaffer, "Effect of copper and silicon content on mechanical properties in Al–Cu–Si–Mg alloys", Journal of Materials Processing Technology Vol. 169 (2005), 292–298.

[15] Z. Muzaffer, Karakulak Erdem, GÜMÜŞ Serap, "Influence of Cu addition on microstructure and hardness of near-eutectic Al-Si-*x*Cu-alloys", Trans. Nonferrous Met. Soc. China vol. 21, (2011), 1698-1702.

[16] Hossain, A. S. W. Kurny, "Optimization of Artificial Ageing Time and Temperature on Evaluation of Hardness and Resistivity of Al-Si-Mg (Cu or/& Ni) Alloys", International Journal of Chemical, Materials Science and Engineering, Vol. 8 (2014), No: 4, 291-296.

[17] Nurul Razliana Abdul Razak, Nisrin Adli, Norainiza Saud, and Sayyaidah Amnah Musa, "Effect of Aluminum Addition on Microstructure and Microhardness of Sn-0.7 Cu-xAl Lead-free Solder Alloy", Applied mechanics and Materials, Vol. 754-755 (2015), 166-170.

JJMIE

Volume 10 Number 1, March.2016
ISSN 1995-6665
Pages 27- 38

Jordan Journal of Mechanical and Industrial Engineering

Using DEA Window Analysis to Measure the Efficiencies of Blowing Machines in Plastics Industry

Abbas Al-Refaie [a *], Ruba Najdawi[b], Erin Sy[c]

[a] Department of Industrial Engineering, University of Jordan, Amman, 11942, Jordan.
[b] Received Master degree in Industrial Engineering, University of Jordan.
[c] Instructor, Ateneo de Manila University. 1108, Metro Manila, Philippines.

Received 25 Feb 2015 Accepted 17 Sep 2015

Abstract

Efficiency evaluation is vital in determining whether a production line can achieve its goals or not. The present study aims at assessing the efficiency of five blowing machines in a plastics industry using DEA window analysis in both day and night shifts for the period Feb., 2014 to Jun., 2014. The production quantity is set as the output, whereas the defect quantity and idle time (units) are set as the inputs for all windows. Utilizing the DEA models, the technical, pure technical and scale efficiency values are then calculated in both day and night shifts for each machine. A comparison is conducted between the day and night shifts for each machine. Moreover, comparisons are performed among the efficiency of five machines in both day and night shifts. Improvement actions are then suggested to reduce the inefficiency. Results showed that significant differences exist between day and night shifts for each machine. Directions for improvement are then suggested, which requires managerial as well as operational actions to improve process performance. In conclusions, the thorough analysis and discussion of the results in the present paper provide a valuable evaluation to production managers for improving the performance of blowing processes.

Keywords: *Window Analysis, Plastics Industry, Pure Technical Efficiency, Scale Efficiency.*

1. Introduction

Plastics are one of the most used materials on a volume basis in the industrial and commercial life of the countries. Plastics are broadly integrated in today's life style and make a major, irreplaceable contribution to virtually all product areas. Measurement of a production unit-performance is vital in determining whether it has achieved its goals or not [1-2].

Data Envelopment Analysis (DEA) is a management tool employed to estimate the efficiency of number of decision making units (DMU's). DEA is a non-parametric approach that can be used to calculate the efficiency measures, and has a wide applicability in various service and industry sectors [3-6]. This approach has been widely used in cases which have been resistant to other approaches and it is related to the complex and unknown nature of the relations between the multiple inputs and multiple outputs involved in many of these activities [7-10].

1.1. The CCR and BCC Models

The CCR Model considers a fixed or constant return to scale (CRS), which means that a proportional increase in all inputs results in the same proportional increase in outputs [11]. The efficiency of a given DMU_o is calculated using the CCR model as follows:

$$Min\ \theta \tag{1}$$

Subject to:

$$\sum_{j=1}^{n} \lambda_j x_{ij} \le \theta x_{io} \qquad i = 1.....m \tag{1a}$$

$$\sum_{j=1}^{n} \lambda_j y_{kj} \ge y_{ko} \qquad k = 1.....s \tag{1b}$$

$$\lambda_j \ge 0 \qquad j = 1.....n \tag{1c}$$

where θ represents the technical efficiency score of unit DMU_o, λ_j represents the dual variables that identify the benchmarks for inefficient units. If θ^* is equal to a value of one, then the examined DMU is considered technically efficient and lies on the efficiency frontier that is composed of the set of efficient units, DEA measures the efficiency of each observation relative to the frontier that envelopes all the observations. Inefficient DMUs can be improved (moved to the efficient frontier) with proposed directions for improvement which are the points

* Corresponding author e-mail: Abbas.alrefai@ju.edu.jo.

along the frontier. The distance to the efficiency frontier provides a measure for the efficiency.

On the other hand, the BCC model by Banker-Charnes-Cooper changed the Constant Return to Scale (CRS) concept to Variable Return to Scale (VRS). The DMU operates under variable returns to scale if it is suspected that an increase in inputs does not result in a proportional change in the outputs. The BCC is represented as follows [12]:

$$Min\ \theta \tag{2}$$

Subject to:

$$\sum_{j=1}^{n} \lambda_j x_{ij} \le \theta x_{io} \qquad i = 1.....m \tag{2a}$$

$$\sum_{j=1}^{n} \lambda_j y_{kj} \ge y_{ko} \qquad k = 1.....s \tag{2b}$$

$$\sum_{j=1}^{n} \lambda_j = 1 \qquad j = 1.....n \tag{2c}$$

$$\lambda_j \ge 0 \tag{2d}$$

The BCC model divides the Technical Efficiency (TE) derived from the CCR model into two parts [13-16]: (*i*) Pure Technical Efficiency (PTE), which ignores the impact of scale size by only comparing a DMU to a unit of similar scale and measures how a DMU utilizes its sources under exogenous environment and (*ii*) Scale Efficiency (SE), which measures how the scale size affects efficiency. If after applying both CRS, VRS model on the same data, there is a difference in the two technical efficiencies, this indicates that DMU has a scale efficiency, and can be calculated by:

$$SE = TE/PTE \tag{3}$$

1.2. DEA Window Analysis

DEA window analysis is a non-parametric panel approach, which is a suitable tool technique to measure the efficiency level of a number of DMUs with respect to its own performance over time, as well as the performance of the relatively most productive decision units within the sample set [17-20]. The arrangement of the results in DEA window analysis facilitates the identification of trends in performance, the stability of reference sets and other possible insights. If *N* represents the number of DMUs (*n* = 1,2, 3 …..*N*) that all use *m* inputs to produce *s* outputs and are observed in *T* (*t* = 1, 2, 3 …..*T*) periods [20-24]. Let DMU_n^t represent an observation *n* in period *t* with input vector $\boldsymbol{X_n^t}$ and output vector $\boldsymbol{Y_n^t}$ respectively. Then,

$$\mathbf{X}_n^t = \begin{bmatrix} x_n^{1t} \\ \vdots \\ x_n^{mt} \end{bmatrix} \tag{4}$$

and

$$\mathbf{Y}_n^t = \begin{bmatrix} y_n^{1t} \\ \vdots \\ y_n^{st} \end{bmatrix} \tag{5}$$

If the window starts at time *k* (1≤ *k* ≤*T*) with width *w* (1≤*w*≤ *T-k*), then the matrices of inputs and outputs, X_{kw} , are denoted respectively as follows:

$$X_{kw} = \begin{bmatrix} x_1^k & x_2^k & \cdots & x_N^k \\ x_1^{k+1} & x_2^{k+1} & \cdots & x_N^{k+1} \\ \vdots & \vdots & \ddots & \vdots \\ x_1^{k+w} & x_2^{k+w} & \cdots & x_N^{k+w} \end{bmatrix} \tag{6}$$

and

$$Y_{kw} = \begin{bmatrix} y_1^k & y_2^k & \cdots & y_N^k \\ y_1^{k+1} & y_2^{k+1} & \cdots & y_N^{k+1} \\ \vdots & \vdots & \ddots & \vdots \\ y_1^{k+w} & y_2^{k+w} & \cdots & y_N^{k+w} \end{bmatrix} \tag{7}$$

DEA window analysis is conducted by substituting inputs and outputs of DMU_n^t into the CCR or the BCC models [25-28]. In the present study, a plant specialized in the production of plastic containers seeks assessing the performance of blowing machines and determines opportunities for performance improvements. To achieve this objective, the present study utilizes DEA window analysis to measure the efficiency of the five identical blowing machines at both day and night shifts over the period February to July, 2014. The research results can provide a helpful guidance to product/process engineers in assessing existing process performance and help in deciding appropriate improvement actions. The remaining part of the study, including the introduction, is outlined in the following sequence: Section two is for Data Collection; Section three conducts DEA window analysis; Section four discusses and summarizes the research results; and finally, conclusions are provided in section five.

2. Data Collection

Data are obtained from the production report over a period of six months for both day and night shifts for the five blowing machine: M1, M2, M3, M4, and M5. The choice between input and output orientation depends on the unique characteristic of the set of DMUs under study. The input oriented model is deemed to be more appropriate in the present paper because there is only one output while multiple inputs are used; this model tends to minimize the inputs while satisfying at least the given output levels, and for this reason the Defect Quantities (DQ) and Idle Time (IT) are considered as inputs and need to be minimized while the Production Quantity (PQ) needs to be maintained at the same level. To compute efficiency scores, each month was divided into two periods and each period consisted of two weeks where (H1) represents the first half of the month and (H2) represents the second half of the month. Inputs and outputs data are presented in Table 1; Table 6 lists the descriptive statistics of the inputs and the output for both day and night shifts.

Table 1. The inputs and output data for M1 Day and Night shift.

Period	Day Shift				Night Shift			
	Inputs			Output	Inputs			Output
	PP (units)	DQ (units)	IT (units)	PQ (units)	PP (units)	DQ (units)	IT (units)	PQ (units)
Feb. H1	24,192	192	1,446	22,000	24,192	185	1,426	22,300
Feb. H2	24,192	241	8,975	14,834	24,192	94	7,996	15,731
Mar. H1	24,192	251	5,202	18,763	24,192	69	3,149	21,419
Mar. H2	24,192	236	8,274	15,781	24,192	97	6,414	18,359
Apr. H1	20,736	197	2,329	18,000	20,736	176	1,935	17,221
Apr. H2	27,648	201	569	26,960	27,648	142	51	27,720
May H1	24,192	242	4,116	19,984	24,192	120	3,420	19,456
May H2	20,736	264	2,481	20,042	20,736	53	2,081	19,616
Jun. H1	13,824	79	1,621	11,955	13,824	32	678	13,500
Jun. H2	10,368	76	3,016	7,740	10,368	73	2,855	8,318
Jul. H1	15,552	118	3,609	12,600	15,552	115	2,962	13,350
Jul. H2	22,646	240	3,054	19,370	22,464	245	2,339	20,750

3. Application of DEA Window Analysis

The window analysis considers each blowing machine as a different machine in each of the halves listed at the top of the table in order to obtain the scores listed in the rows that constitute the window, while the stub on the left side indicates the window length and the periods covered. For example, the first row extends from the first half of February (Feb. H1) to the second half of April (Apr. H2) for a window length of six halves that is exhibited in the first row. The next row starts in second half of February (Feb. H2) and extends to the first half of May (May H1) which represents another window and so on. This results in seven windows (w) for each shift. Then, there are 210 different data points in each shift to which the DEA model is applied to obtain the efficiency scores. Firstly, the Technical Efficiency (TE) and Pure Technical Efficiency (PTE) are computed using CCR and BCC models, respectively. The Scale Efficiency (SE) is then calculated. Tables 2 and 3 present the TE, PTE and SE values for machine M1 in the day and night shifts, respectively. To illustrate, for machine M1 in the day shift (M1d) the first window extends from first half of February (Feb. H1) to the second half of April (Apr. H2) for a window length of 6 half's, TE (= 0.9326**)** in Table 2 is calculated using the CCR model as follows:

$$Min\,\theta$$

Subject to:

$$-24,192\lambda_1 - 24,192\lambda_2 - 24,192\lambda_3 - 24,192\lambda_4 - 20,736\lambda_5 - 27,648\lambda_6 + 24,192\theta \geq 0$$

$$-192\lambda_1 - 241\lambda_2 - 251\lambda_3 - 236\lambda_4 - 197\lambda_5 - 201\lambda_6 + 192\theta \geq 0$$

$$-1,446\lambda_1 - 8,975\lambda_2 - 5,202\lambda_3 - 8,274\lambda_4 - 2,329\lambda_5 - 569\lambda_5 + 1,446\theta \geq 0$$

$$22,000\lambda_1 + 14,834\lambda_2 + 18,763\lambda_3 + 15,781\lambda_4 + 18,000\lambda_5 + 26960\lambda_6 \geq 22000$$

$$\lambda_j \geq 0,\ j = 1,2,3$$

The corresponding PTE (= 1.00) for M1d is calculated using BCC model as follows:

$$Min\,\theta$$

Subject to:

$$-24,192\lambda_1 - 24,192\lambda_2 - 24,192\lambda_3 - 24,192\lambda_4 - 20,736\lambda_5 - 27,648\lambda_6 + 24,192\theta \geq 0$$

$$-192\lambda_1 - 241\lambda_2 - 251\lambda_3 - 236\lambda_4 - 197\lambda_5 - 201\lambda_6 + 192\theta \geq 0$$

$$-1,446\lambda_1 - 8,975\lambda_2 - 5,202\lambda_3 - 8,274\lambda_4 - 2,329\lambda_5 - 569\lambda_5 + 1,446\theta \geq 0$$

$$22,000\lambda_1 + 14,834\lambda_2 + 18,763\lambda_3 + 15,781\lambda_4 + 18,000\lambda_5 + 26960\lambda_6 \geq 22000$$

$$\lambda_1 + \lambda_2 + \lambda_3 + \lambda_4 + \lambda_5 + \lambda_6 = 1$$

$$\lambda_j \geq 0,\ j = 1,2,3$$

Finally, the SE for M1d is calculated as:

$$SE = TE/PTE = \frac{0.9326}{1} = 1$$

The TE, PTE, and SE for the other windows in day shift and the windows in the night shift are calculated in a similar manner. The TE, PTE, and SE for the M2-M5 in the day and night shifts are calculated similarly.

4. Results and Discussions of DEA Window

An inefficient DMU can be made more efficient by projection onto the frontier, and in the input orientation the efficiency can be improved through proportional reduction of inputs. For practical considerations, a classification of all TE scores in all windows produced three categories; the first category is the highly efficient category (H-efficient), which includes the DMUs that have a value of efficiency equals to or larger than 95%; the second category is the efficient category (Efficient) and includes machines that have a value of efficiency between (90% - <95%); the third category is the inefficient category (Inefficient) and includes DMUs that have a value of efficiency less than 90%. Applying this classification means that the first four windows are (Inefficient) and the last three windows are (Efficient). The results in Table 4 are used for determining extra inputs and deficiency of efficiency for M1d and the specific quantity of input that inefficient machine needs to decrease in order to become efficient in order to stand on the efficiency frontier line for the smallest and largest TE and PTE average values.

Table 2. DEA window analysis for TE, PTE and SE over February-July 2014 for M1/day shift

TE	Feb. (H1)	Feb. (H2)	Mar. (H1)	Mar. (H2)	Apr. (H1)	Apr. (H2)	May (H1)	May (H2)	Jun. (H1)	Jun. (H2)	Jul. (H1)	Jul. (H2)	Avg.	Std.	CV	Min.	Max.
Feb. H1-Apr. H2	0.9326	0.6288	0.7954	0.6690	0.8902	1.0000							0.8193	0.1483	0.1810	0.6288	1.0000
Feb. H2-May H1		0.6288	0.7954	0.6690	0.8902	1.0000	0.8471						0.8051	0.1391	0.1727	0.6288	1.0000
Mar. H1-May H2			0.7954	0.6690	0.8902	1.0000	0.8471	0.9912					0.8655	0.1252	0.1447	0.6690	1.0000
Mar. H2-Jun. H1				0.6690	0.8902	1.0000	0.8471	0.9912	1.0000				0.8996	0.1301	0.1446	0.6690	1.0000
Apr. H1-Jun. H2					0.8902	1.0000	0.8471	0.9912	1.0000	0.7656			0.9157	0.0978	0.1068	0.7656	1.0000
Apr. H2-Jul. H1						1.0000	0.8471	0.9912	1.0000	0.7656	0.8309		0.9058	0.1037	0.1037	0.7656	1.0000
May H1-Jul. H2							0.8911	1.0000	1.0000	0.8405	0.9083	0.9204	0.9267	0.0630	0.0630	0.8405	1.0000
Avg.	0.9326	0.6288	0.7954	0.6690	0.8902	1.0000	0.8544	0.9930	1.0000	0.7906	0.8696	0.9204					
PTE	Feb. (H1)	Feb. (H2)	Mar. (H1)	Mar. (H2)	Apr. (H1)	Apr. (H2)	May (H1)	May (H2)	Jun. (H1)	Jun. (H2)	Jul. (H1)	Jul. (H2)	Avg.	Std.	CV	Min.	Max.
Feb. H1-Apr. H2	1.0000	0.8571	0.8815	0.8571	1.0000	1.0000							0.9326	0.0744	0.0797	0.8571	1.0000
Feb. H2-May H1		0.8571	0.8815	0.8571	1.0000	1.0000	0.9204						0.9194	0.0666	0.0725	0.8571	1.0000
Mar. H1-May H2			0.8626	0.8571	1.0000	1.0000	0.9006	1.0000					0.9367	0.0709	0.0757	0.8571	1.0000
Mar. H2-Jun. H1				0.7066	0.9235	1.0000	0.8650	1.0000	1.0000				0.9159	0.1163	0.1270	0.7066	1.0000
Apr. H1-Jun. H2					0.9235	1.0000	0.8650	1.0000	1.0000	1.0000			0.9648	0.0577	0.0598	0.8650	1.0000
Apr. H2-Jul. H1						1.0000	0.8650	1.0000	1.0000	1.0000	0.9243		0.9649	0.0575	0.0596	0.8650	1.0000
May H1-Jul. H2							1.0000	1.0000	1.0000	1.0000	0.9243	1.0000	0.9874	0.0309	0.0313	0.9243	1.0000
Avg.	1.0000	0.8571	0.8752	0.8195	0.9694	1.0000	0.9027	1.0000	1.0000	1.0000	0.9243	1.0000					
SE	Feb. (H1)	Feb. (H2)	Mar. (H1)	Mar. (H2)	Apr. (H1)	Apr. (H2)	May (H1)	May (H2)	Jun. (H1)	Jun. (H2)	Jul. (H1)	Jul. (H2)	Avg.	Std.	CV	Min.	Max.
Feb. H1-Apr. H2	0.9326	0.7336	0.9023	0.7805	0.8902	1.0000							0.8732	0.0988	0.1131	0.7336	1.0000
Feb. H2-May H1		0.7336	0.9023	0.7805	0.8902	1.0000	0.9204						0.8712	0.0975	0.1119	0.7336	1.0000
Mar. H1-May H2			0.9221	0.7805	0.8902	1.0000	0.9406	0.9912					0.9208	0.0803	0.0872	0.7805	1.0000
Mar. H2-Jun. H1				0.9468	0.9639	1.0000	0.9793	0.9912	1.0000				0.9802	0.0214	0.0218	0.9468	1.0000
Apr. H1-Jun. H2					0.9639	1.0000	0.9793	0.9912	1.0000	0.7656			0.9500	0.0914	0.0962	0.7656	1.0000
Apr. H2-Jul. H1						1.0000	0.9793	0.9912	1.0000	0.7656	0.8990		0.9392	0.0932	0.0993	0.7656	1.0000
May H1-Jul. H2							0.8911	1.0000	1.0000	0.8405	0.9827	0.9204	0.9391	0.0659	0.0701	0.8405	1.0000
Avg.	0.9326	0.7336	0.9089	0.8221	0.9197	1.0000	0.9483	0.9930	1.0000	0.7906	0.9408	0.9204					

Table 3. DEA window analysis for TE, PTE and SE over February-July 2014 for M1/night shift

TE	Feb. (H1)	Feb. (H2)	Mar. (H1)	Mar. (H2)	Apr. (H1)	Apr. (H2)	May (H1)	May (H2)	Jun. (H1)	Jun. (H2)	Jul. (H1)	Jul. (H2)	Avg.	Std.	CV	Min.	Max.
Feb. H1-Apr. H2	0.9194	0.6929	1.0000	0.8032	0.8283	1.0000							0.8740	0.1214	0.1389	0.6929	1.0000
Feb. H2-May H1		0.6929	1.0000	0.8032	0.8283	1.0000	0.8094						0.8556	0.1215	0.1420	0.6929	1.0000
Mar. H1-May H2			0.9295	0.7760	0.8283	1.0000	0.8052	1.0000					0.8898	0.0998	0.1121	0.8052	1.0000
Mar. H2-Jun. H1				0.7648	0.8283	1.0000	0.8034	0.9665	1.0000				0.8938	0.1067	0.1194	0.7648	1.0000
Apr. H1-Jun. H2					0.8283	1.0000	0.8034	0.9665	1.0000	0.8002			0.8997	0.0988	0.1099	0.8002	1.0000
Apr. H2-Jul. H1						1.0000	0.8034	0.9665	1.0000	0.8002	0.8562		0.9044	0.0954	0.1055	0.8002	1.0000
May H1-Jul. H2							0.8235	0.9687	1.0000	0.8215	0.8790	0.9459	0.9064	0.0762	0.0841	0.8215	1.0000
Avg.	0.9194	0.6929	0.9765	0.7868	0.8283	1.0000	0.8081	0.9736	1.0000	0.8073	0.8676	0.9459					
PTE	**Feb. (H1)**	**Feb. (H2)**	**Mar. (H1)**	**Mar. (H2)**	**Apr. (H1)**	**Apr. (H2)**	**May (H1)**	**May (H2)**	**Jun. (H1)**	**Jun. (H2)**	**Jul. (H1)**	**Jul. (H2)**	**Avg.**	**Std.**	**CV**	**Min.**	**Max.**
Feb. H1-Apr. H2	0.9954	0.9703	1.0000	0.9669	1.0000	1.0000							0.9888	0.0158	0.0159	0.9669	1.0000
Feb. H2-May H1		0.9703	1.0000	0.9669	1.0000	1.0000	0.9413						0.9798	0.0243	0.0248	0.9413	1.0000
Mar. H1-May H2			1.0000	0.8571	1.0000	1.0000	0.8571	1.0000					0.9524	0.0738	0.0775	0.8571	1.0000
Mar. H2-Jun. H1				0.7669	0.8411	1.0000	0.8108	1.0000	1.0000				0.9031	0.1087	0.1204	0.7669	1.0000
Apr. H1-Jun. H2					0.8411	1.0000	0.8108	1.0000	1.0000	1.0000			0.9420	0.0904	0.0960	0.8108	1.0000
Apr. H2-Jul. H1						1.0000	0.8108	1.0000	1.0000	1.0000	0.8825		0.9489	0.0824	0.0868	0.8108	1.0000
May H1-Jul. H2							0.8497	1.0000	1.0000	1.0000	0.8825	1.0000	0.9554	0.0699	0.0732	0.8497	1.0000
Avg.	0.9954	0.9703	1.0000	0.8895	0.9364	1.0000	0.8468	1.0000	1.0000	1.0000	0.8825	1.0000					
SE	**Feb. (H1)**	**Feb. (H2)**	**Mar. (H1)**	**Mar. (H2)**	**Apr. (H1)**	**Apr. (H2)**	**May (H1)**	**May (H2)**	**Jun. (H1)**	**Jun. (H2)**	**Jul. (H1)**	**Jul. (H2)**	**Avg.**	**Std.**	**CV**	**Min.**	**Max.**
Feb. H1-Apr. H2	0.9236	0.7141	1.0000	0.8307	0.8283	1.0000							0.8828	0.1125	0.1274	0.7141	1.0000
Feb. H2-May H1		0.7141	1.0000	0.8307	0.8283	1.0000	0.8599						0.8722	0.1109	0.1271	0.7141	1.0000
Mar. H1-May H2			0.9295	0.9054	0.8283	1.0000	0.9394	1.0000					0.9338	0.0644	0.0690	0.8283	1.0000
Mar. H2-Jun. H1				0.9973	0.9848	1.0000	0.9909	0.9665	1.0000				0.9899	0.0129	0.0130	0.9665	1.0000
Apr. H1-Jun. H2					0.9848	1.0000	0.9909	0.9665	1.0000	0.8002			0.9571	0.0778	0.0813	0.8002	1.0000
Apr. H2-Jul. H1						1.0000	0.9909	0.9665	1.0000	0.8002	0.9702		0.9546	0.0770	0.0807	0.8002	1.0000
May H1-Jul. H2							0.9692	0.9687	1.0000	0.8215	0.9960	0.9459	0.9502	0.0661	0.0696	0.8215	1.0000
Avg.	0.9236	0.7141	0.9765	0.8910	0.8909	1.0000	0.9569	0.9736	1.0000	0.8073	0.9831	0.9459					

From Tables 2 and 4, the following results are obtained:

- In Table 2, the TE relates to processing inputs to achieve the output as supposed when compared to its maximum potential for doing so. The second window of TE for M1d (Feb. H2-May H1) produced the smallest TE average value (= 0.8051). The TE for M1d in Feb. H2 (= 0.6288) implies that the same level of output could be produced with 62.88% of the resources if this machine was performing on the frontier. It could be interpreted also that 37.12% of overall resources could be saved by raising the performance of this machine to the highest level. In Table 4, in order for M1d in this half to become efficient, it needs to decrease 41 units of the Defect Quantity (DQ) in addition to decrease 5331 units of the Idle Time (IT). On the one hand, M1d in Apr. H2 stands on the efficiency frontier line and does not need to decrease any of the inputs. On the other hand, the last window of TE for M1d (May H1-Jul. H2) produced the largest TE average value (= 0.9267), TE for M1d in May H1 (= 0.8911) implies that the same level of output could be produced by 89.11% of the resources if this machine was performing on the frontier, it could be interpreted also that 10.89% of the overall resources could be saved by raising the performance of this machine to the highest level. In order for M1d in this half to become more efficient and to stand on the efficiency frontier, it needs only to decrease the idle time (IT) by 1109 units.
- In window DEA, the columns define the stability. The columns in window DEA are used to examine stability properties. The TE values of M1d in Table 2 showed a stable performance for all periods. For example, the TE in Mar. H2 equals 0.7954 for three windows; also TE in Apr. H1 was (=0.8902) for five windows. But, the row window is monitored to identify the performance trends. For example, in the first row the TE average is 0.8193 and a standard deviation equals to 0.1483. It is found that the Coefficient of Variation (CV) for TE values in all of the windows for M1d are larger than 5%, which means that indicates the existence of trends in the efficiencies of the same window. Finally, the technical inefficiency (TIE) average values for M1d over February-July 2014 are depicted in Fig. 1, where a decreasing trend in the TIE average values is observed starting Feb. H2-May H1 window. This means that the M1d is improved in processing the inputs to achieve the output as supposed when compared to its maximum potential for doing so through the covered period. Nevertheless, the minimal and maximal TE average values indicate that the performance of the machine M1 alternates between inefficient and efficient. None of the windows indicates a highly-efficient performance. On the other hand, M1d in Apr. H2 and Jun. H1 stand on the efficiency frontier line and do not need to decrease any of their inputs.

Table 4. The TE, PTE, inputs, output and slacks for of M1/d.

Smallest TE average= 0.8051													
DMU	θ	Input 1:PP	Input 2:DQ	Input 3:IT	Output 1:PQ	Variables				Slack/Surplus			
						u1	u2	u3	v	PP	DQ	IT	PQ
Feb. H2	0.6288	24,192	241	8,975	14,834	0.4134E-04	0	0	0.4239E-04	0	40.9	5330.6	0
Mar. H1	0.7954	24,192	251	5,202	18,763	0.4134E-04	0	0	0.4239E-04	0	59.7	3741.6	0
Mar. H2	0.6690	24,192	236	8,274	15,781	0.4134E-04	0	0	0.4239E-04	0	40.2	5201.9	0
Apr. H1	0.8902	20,736	197	2,329	18,000	0.4823E-04	0	0	0.4946E-04	0	41.2	1693.4	0
Apr. H2	1.0000	27,648	201	569	26,960	0.3617E-04	0	0	0.3709E-04	0	0	0	0
May H1	0.8471	24,192	242	4,116	19,984	0.4134E-04	0	0	0.4239E-04	0	56.0	3065.1	0
Largest TE average= 0.9267													
DMU	θ	Input 1:PP	Input 2:DQ	Input 3:IT	Output 1:PQ	Variables				Slack/Surplus			
						u1	u2	u3	v	PP	DQ	IT	PQ
May H1	0.8911	24,192	242	4,116	19,984	0.3487E-04	0.6465E-03	0	0.4459E-04	0	0	1108.5	0
May H2	1.0000	20,736	264	2,481	20,042	0.3902E-04	0.7234E-03	0	0.4989E-04	0	0	0	0
Jun. H1	1.0000	13,824	79	1,621	11,955	0.6541E-04	0.1213E-02	0	0.8365E-04	0	0	0	0
Jun. H2	0.8405	10,368	76	3,016	7,740	0.8491E-04	0.1574E-02	0	0.1086E-03	0	0	1508.3	0
Jul. H1	0.9083	15,552	118	3,609	12,600	0.5637E-04	0.1045E-02	0	0.7209E-03	0	0	1612.7	0
Jul. H2	0.9204	22,646	240	3,054	19,370	0.3691E-04	0.6843E-03	0	0.4719E-04	0	0	329.9	0
Smallest PTE average= 0.9159													
DMU	θ	Input 1:PP	Input 2:DQ	Input 3: IT	Output: PQ	Variables				Slack/Surplus			
						u1	u2	u3	v	PP	DQ	IT	PQ
Mar. H2	0.7066	24,192	236	8,274	15,781	0.4134E-04	0	0	0.3533E-04	0	0.2	3818.6	0
Apr. H1	0.9235	20,736	197	2,329	18,000	0.4624E-04	0.2088E-03	0	0.4429E-04	0	0	310.1	0
Apr. H2	1.0000	27,648	201	569	26,960	0.3502E-04	0.1581E-03	0	0.3354E-04	0	0	0	0
May H1	0.8650	24,192	242	4,116	19,984	0.3955E-04	0.1786E-03	0	0.3789E-04	0	0	1723.9	0
May H2	1.0000	20,736	264	2,481	20,042	0.4560E-04	0.2059E-03	0	0.4369E-04	0	0	0	0
Jun. H1	1.0000	13,824	79	1,621	11,955	0.7234E-04	0	0	0	0	0	0	0
Largest PTE average= 0.9874													
DMU	θ	Input 1:PP	Input 2:DQ	Input 3: IT	Output: PQ	Variables				Slack/Surplus			
						u1	u2	u3	v	PP	DQ	IT	PQ
May H1	1.0000	24,192	242	4,116	19,984	0.1533E-04	0.2599E-02	0	0.7257E-04	0	0	0	0
May H2	1.0000	20,736	264	2,481	20,042	0.4823E-04	0	0	0.4122E-04	0	0	0	0
Jun. H1	1.0000	13,824	79	1,621	11,955	0.5605E-04	0	0.1389E-03	0	0	0	0	0
Jun. H2	1.0000	10,368	76	3,016	7,740	0.5605E-04	0	0.1389E-03	0	0	0	0	0
Jul. H1	0.9243	15,552	118	3,609	12,600	0.6430E-04	0	0	0.5496E-04	0	15.3	1646.3	0
Jul. H2	1.0000	22,646	240	3,054	19,370	0.1608E-04	0.3497E-02	0.4063E-04	0.8572E-04	0	0	0	0

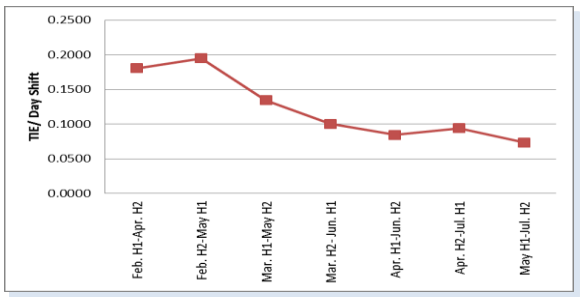

Figure 1. The TIE values for M1 in day shift over February-July 2014

Further, the PTE is a measure obtained by estimating the efficient frontier under the assumption of variable returns-to-scale and measures the technical efficiency without scale efficiency by comparing a production machine only to other machines of similar scale. In practice, the PTE purely reflects the managerial performance to organize the inputs in the production process. In Table 2 for the PTE values, the following results are obtained:

- The PTE for M1d in Mar. H2 (= 0.7066) implies that the same level of output could be produced by 70.66% of the resources if this unit was performing on the frontier taking into consideration that the scale size is ignored, also it is interpreted that 29.34% of overall resources could be saved by raising the performance of this machine to the highest level. In order for M1d in this half to become efficient, it needs to decrease one unit of Defect Quantity (DQ) and to decrease 3819 units of the Idle Time (IT). Finally, Apr. H2, May H2, Jun. H1, Jun. H2, and Jul. H2 lie on the efficiency frontier line and do not need to decrease any of the inputs. It is noticed that the number of periods identified efficient by BCC model are larger than that using CCR model.
- The PTE for Mar. H2-Jun. H1 incurs the smallest PTE average value (= 0.9159), the specific quantity of inputs that inefficient unit needs to decrease in order to become efficient are determined to stand on the efficiency frontier line ignoring the scale size. However, the May H1-Jul. H2 window corresponds to the largest PTE average value (= 0.9874). Using the BCC model some windows are identified highly-efficient, whereas none of the windows is found using the CCR model.
- The PTE for M1d in Jul. H1 (= 0.9243) implies that the same level of output could be produced by 92.43% of the resources if this unit was performing on the frontier taking into consideration that the scale size is ignored, also it is interpreted that 7.57% of overall resources could be saved by raising the performance of this machine to the highest level. In order for M1d in this half to become efficient, it needs to decrease 16 units of the Defect Quantity (DQ) and decrease 1647 units of the idle time in units (IT). M1d in May H1, May H2, Jun. H1, Jun. H2 and Jul. H2 lie on the efficiency frontier line and doesn't need to decrease any of the inputs. The columns in window DEA are used to

examine stability properties, the values for PTE of M1d showed a stable performance for all windows, for example PTE in Apr. H2 is (= 1.00) and frequented with the same value for three windows, also PTE in Jul. H1 is (= 0.9243) frequented with the same value for three windows.

- In Window DEA, the row window is monitored to identify the performance trends. For example, in the first row PTE average is (= 0.9326) with a standard deviation that is equal to (= 0.0744). The corresponding Coefficient of Variation (CV) for PTE values in all windows are larger than 5% except in the last window (May H1-Jul. H2), which means that there is a trend in the efficiencies of the same window.
- Applying the classification on PTE scores means that the first four windows are (Efficient) and the last three windows are (H-efficient). Figure 2 presents the pure technical inefficiency (PTIE) average values for M1d over February-July 2014. In this figure, a fluctuation in the PTIE average values during the first four windows then a decreasing trend in PTIE average values is observed starting March H2-Jun.H1 window. The maximum PTIE average value corresponds to March H2-Jun. H1. Typically, PTE is used to measure how a firm utilizes its resources under exogenous environments, hence the results reveal than M1d effectively utilizes its resources over the covered period; in other words, the managerial performance in organizing the inputs in the production process has been improved.

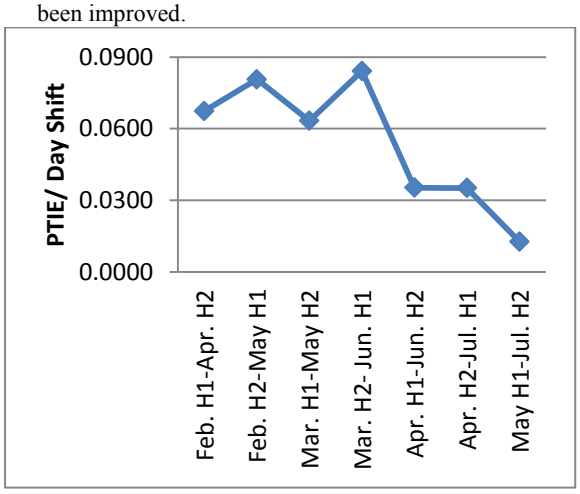

Figure 2. PTIE values for M1 in day shift over February-July 2014.

Furthermore, the SE measure provides the ability of the management to choose the optimum size of resources in order to choose the scale of production that will attain the expected production level. From Table 2, the following results are found:

- The largest SE average for M1d was (= 0.9802), which occurs in the fourth window (Mar. H2- Jun.H1), whereas the smallest SE average was (= 0.8712) which corresponds to the second window (Feb. H2-May H1). Applying the classification on SE scores, the first and the second windows are (Inefficient), the third window is (Efficient), the fourth and fifth windows are (H-efficient) and finally the sixth and last window are (Efficient).
- The values for SE of M1d showed a stable performance for all windows. For example, the SE in Mar. H2 of 0.7805 frequented repeated for three windows. In addition, the coefficient of variation (CV) for SE values in all of the windows for M1d was larger than 5% except in the fourth window (Mar. H2- Jun.H1) which means that there is a trend in the efficiencies of the same window.
- Figure 3 displays the scale inefficiency (SIE) average values for M1d over Feb.-July 2014, in which a decreasing trend in SIE average values starting Feb. H2-May H1 window till Mar. H2-Jun H2 window after which a slight increase in SIE average values is observed. Practically, the SE provides the ability of management to choose the optimum size of operations. Hence, the results reveal that the management reconsidered the scale of production that attained the maximum expected production level over the covered period.

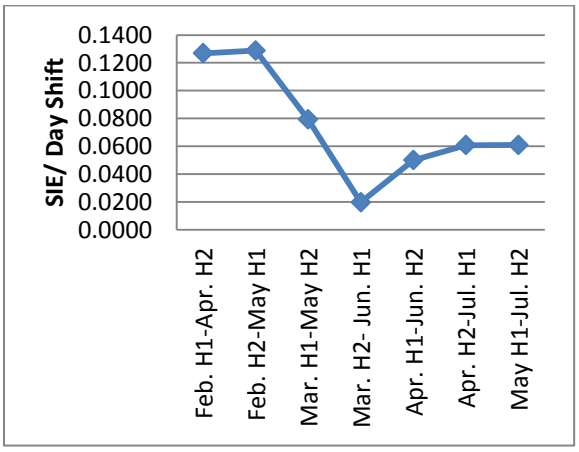

Figure 3. SIE values for M1 in day shift over February-July 2014.

In a similar manner, the TE, PTE, SE values in Table 3 are analyzed for M1 in the night shift. Table 5 displays the obtained results for the smallest and largest TE and PTE values, where the needed reductions in which window inputs can be determined. The corresponding TIE, PTIE, and SIE values are depicted in Figure 4, where similar patterns to day shift are observed in the night shift. Finally, Table 6 displays the efficiency categories for M1 in the day and night shifts over Feb.-July 2014.

Table 5. The TE, PTE, inputs, output and slacks for of M1/n.

Smallest TE average= 0.8556													
DMU	θ	Input 1:PP	Input 2:DQ	Input 3:IT	Output 1:PQ	Variables				Slack/Surplus			
						u1	u2	u3	v	PP	DQ	IT	PQ
Feb. H2	0.6929	24,192	94	7,996	15,731	0.3255E-04	0.2261E-02	0	0.4405E-04	0	0	4331.9	0
Mar. H1	1.0000	24,192	69	3,149	21,419	0.3450E-04	0.2396E-02	0	0.4667E-04	0	0	0	0
Mar. H2	0.8032	24,192	97	6,414	18,359	0.3233E-04	0.2246E-02	0	0.4375E-04	0	0	3886.3	0
Apr. H1	0.8283	20,736	176	1,935	17,221	0.4823E-04	0	0	0.4810E-04	0	57.6	1571.9	0
Apr. H2	1.0000	27,648	142	51	27,720	0.3617E-04	0	0	0.3608E-04	0	0	0	0
May H1	0.8094	24,192	120	3,420	19,456	0.3074E-04	0.2135E-02	0	0.4160E-04	0	0	2538.8	0
Largest TE average= 0.9064													
DMU	θ	Input 1:PP	Input 2:DQ	Input 3:IT	Output 1:PQ	Variables				Slack/Surplus			
						u1	u2	u3	v	PP	DQ	IT	PQ
May H1	0.8235	24,192	120	3,420	19,456	0.4134E-04	0	0	0.4233E-04	0	52.7	1839.3	0
May H2	0.9687	20,736	53	2,081	19,616	0.4823E-04	0	0	0.4938E-04	0	4.8	1030.7	0
Jun. H1	1.0000	13,824	32	678	13,500	0.7234E-04	0	0	0.7407E-04	0	0	0	0
Jun. H2	0.8215	10,368	73	2,855	8,318	0.9645E-04	0	0	0.9877E-04	0	40.3	1927.7	0
Jul. H1	0.8790	15,552	115	2,962	13,350	0.6430E-04	0	0	0.6584E-04	0	69.4	1933.2	0
Jul. H2	0.9459	22,464	245	2,339	20,750	0.4416E-04	0	0	0.4522E-04	0	180.7	1152.5	0
Smallest PTE average= 0.9031													
DMU	θ	Input 1: PP	Input 2: DQ	Input 3: IT	Output: PQ	Variables				Slack/Surplus			
						u1	u2	u3	v	PP	DQ	IT	PQ
Mar. H2	0.7669	24,192	97	6,414	18,359	0.4134E-04	0	0	0.4018E-04	0	4.8	4453.8	0
Apr. H1	0.8411	20,736	176	1,935	17,221	0.4823E-04	0	0	0.4688E-04	0	87.3	113.6	0
Apr. H2	1.0000	27,648	142	51	27,720	0.3617E-04	0	0	0.3516E-04	0	0	0	0
May H1	0.8108	24,192	120	3,420	19,456	0.4134E-04	0	0	0.4018E-04	0	19.2	2356.4	0
May H2	1.0000	20,736	53	2,081	19,616	0.4409E-04	0.1619E-02	0.7663E-03	0.5538E-04	0	0	0	0
Jun. H1	1.0000	13,824	32	678	13,500	0.3476E-04	0	0	0	0	0	0	0
Largest PTE average= 0.9888													
DMU	θ	Input 1: PP	Input 2: DQ	Input 3: IT	Output: PQ	Variables				Slack/Surplus			
						u1	u2	u3	v	PP	DQ	IT	PQ
Feb. H1	0.9554	24,192	185	1,426	22,300	0.4134E-04	0	0	0.2721E-04	0	24.6	395.79	0
Feb. H2	0.9703	24,192	94	7,996	15,731	0.3673E-04	0.1186E-02	0	0	0	0	4861.9	0
Mar. H1	1.0000	24,192	69	3,149	21,419	0.2740E-04	0.1681E-02	0.7019E-04	0	0	0	0	0
Mar. H2	0.9669	24,192	97	6,414	18,359	0.3659E-04	0.1182E-02	0	0	0	0	3333.9	0
Apr. H1	1.0000	20,736	176	1,935	17,221	0.2740E-04	0.1681E-02	0.7019E-04	0	0	0	0	0
Apr. H2	1.0000	27,648	142	51	27,720	0.3617E-04	0	0	0.2381E-04	0	0	0	

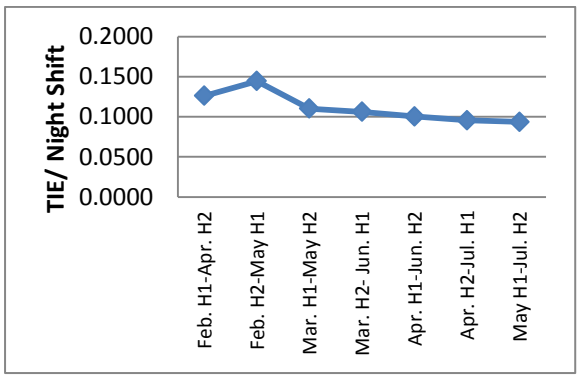

(a) TIE values

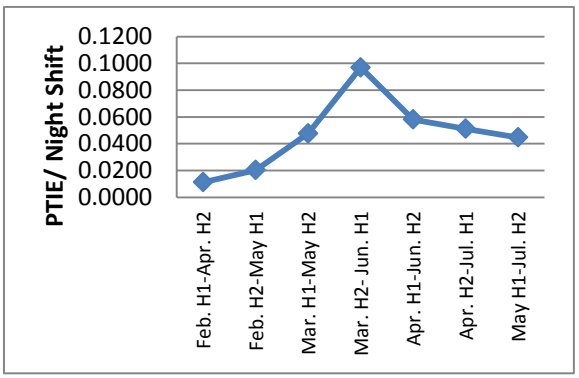

(b) PTIE values

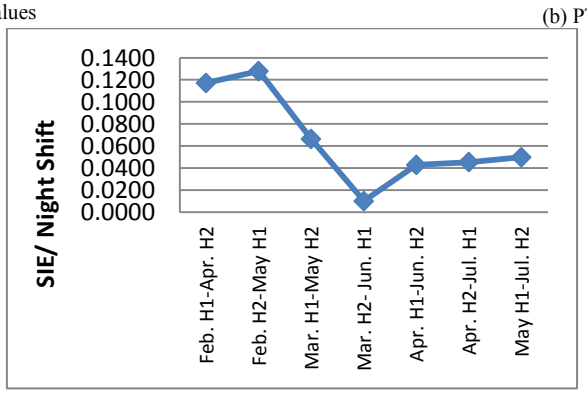

(c) SIE values.

Figure 4. SIE values for M1 in night shift over February-July 2014.

Table 6 displays a classification of TE, PTE, and SE efficiency values in each window for M1 in the day and night shifts. Figure 5 suggests the recommended actions to improve the efficiency values. Decomposing technical efficiency scores into PTE and SE provides guidance on what can be achieved in the short and long terms. If the majority of inefficiency in any production machine is due to low value of SE which means a small size of operations, then the machine needs to be expanded. On the other hand, the PTE value can be usually addressed in the short term without changing the scale of operations; low value of PTE is due to managerial underperformance problem in organizing the inputs in the production process. It should be noted that it is easier to reduce the TIE than to reduce SIE; only when a production machine becomes technically efficient does it make sense to deal with SIE, so production manager should focus on removing the TIE of those production machines before addressing ways to restructure the scale of operation. Following this reasoning, the five blowing machines that were not efficient can be evaluated based on the PTE and SE scores. For example, in Table 6, the TE for M1d in the first window (Feb. H1-Apr. H1) of 0.8193 is considered inefficient because of low SE (= 0.8732), PTE in this window is 0.9326. Then, the low TE value in this window is attributed to the low performance in scale efficiency and the expansion is the solution in this case. Moreover, the TE for M1n in the fourth window of 0.8938 is inefficient because of low PTE (= 0.9031), SE in this window is 0.9899. Then, the low TE value in this window is attributed to the low performance in PTE due to low utilization of the inputs or a problem in transforming inputs into outputs and the number of actual production quantity of the product should be increased. To summarize, for M1 in the day shift the TE values of the first four windows are inefficient due to the low values of SE. However, the TE values are improved in the last three windows due to an improvement in TE values, i.e., reflected through the decrease of DQ and IT plus the increase of output PQ, due to the improvement in the PTE and SE values.

Table 6. Efficiency categories for M1 in the day and night shifts over February-July 2014.

	M1 / Day Shift						M1 / Night Shift					
Window	TE Avg.	Category	PTE Avg.	Category	SE Avg.	Category	TE Avg.	Category	PTE Avg.	Category	SE Avg.	Category
Feb. H1-Apr. H2	0.8193	Inefficient	0.9326	Efficient	0.8732	Inefficient	0.8740	Inefficient	0.9888	H-Efficient	0.8828	Inefficient
Feb. H2-May H1	0.8051	Inefficient	0.9194	Efficient	0.8712	Inefficient	0.8556	Inefficient	0.9798	H-Efficient	0.8722	Inefficient
Mar. H1-May H2	0.8655	Inefficient	0.9367	Efficient	0.9208	Efficient	0.8898	Inefficient	0.9524	H-Efficient	0.9338	Efficient
Mar. H2-Jun. H1	0.8996	Inefficient	0.9159	Efficient	0.9802	H-Efficient	0.8938	Inefficient	0.9031	Efficient	0.9899	H-Efficient
Apr. H1-Jun. H2	0.9157	Efficient	0.9648	H-Efficient	0.9500	H-Efficient	0.8997	Inefficient	0.9420	Efficient	0.9571	H-Efficient
Apr. H2-Jul. H1	0.9058	Efficient	0.9649	H-Efficient	0.9392	Efficient	0.9044	Efficient	0.9489	Efficient	0.9546	H-Efficient
May H1-Jul. H2	0.9267	Efficient	0.9874	H-Efficient	0.9391	Efficient	0.9064	Efficient	0.9554	H-Efficient	0.9502	H-Efficient

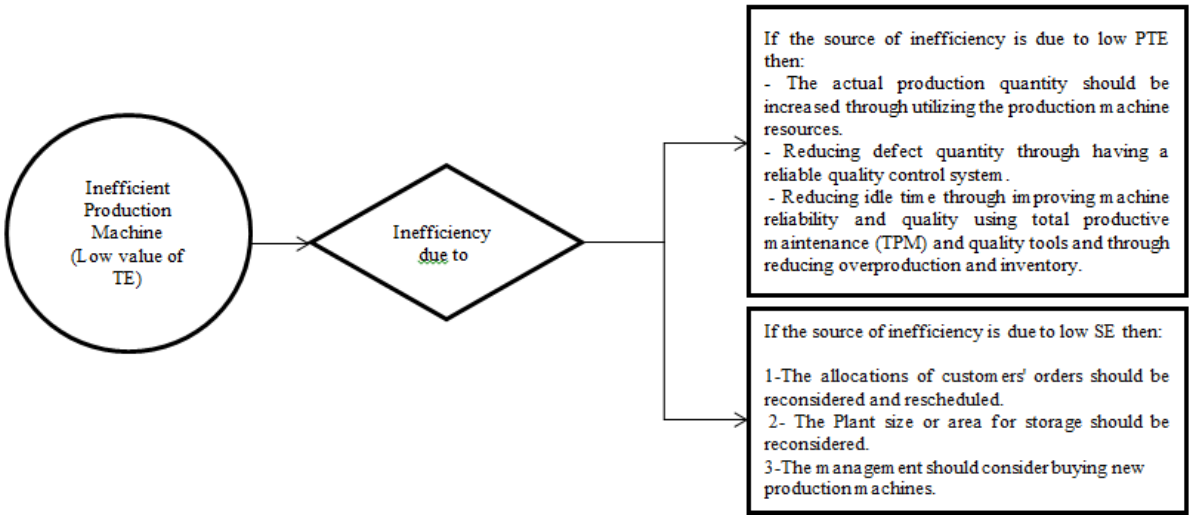

Figure 5. Recommended actions for inefficiency reduction

Finally, a comparison of the TE, PTE, and SE values between the day and night shifts are presented in Figure 6. Obviously, there are slight differences in the TE, PTE, and SE values between the day and night shifts; that is, simalr patterns are exibited in both work shifts.

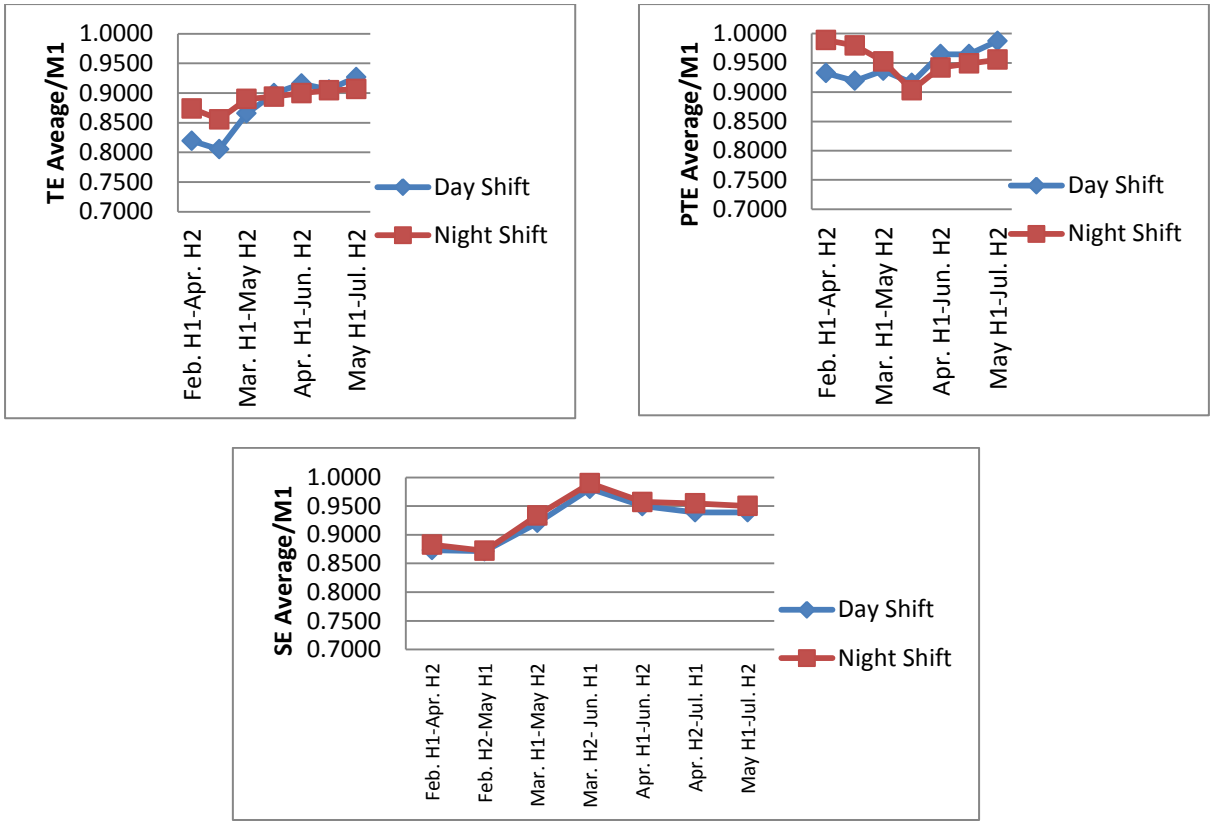

Figure 6. The TE, PTE, and SE average for M1 in day and night shifts over February-July 2014.

In a similar manner, the DEA window analysis is conducted for M2 to M5. The related classification of machine TE, PTE, and SE values in both day and night shifts are displayed in Tables 7 to 10, respectively.

Table 7. Efficiency categories for M2 in the day and night shifts over February-July 2014

	M2 / Day Shift						M2 / Night Shift					
Window	TE Avg.	Category	PTE Avg.	Category	SE Avg.	Category	TE Avg.	Category	PTE Avg.	Category	SE Avg.	Category
Feb. H1-Apr. H2	0.9601	Hi-Efficient	0.9968	Hi-Efficient	0.9633	Hi-Efficient	0.9719	Hi-Efficient	0.9837	Hi-Efficient	0.9881	Hi-Efficient
Feb. H2-May H1	0.9605	Hi-Efficient	0.9912	Hi-Efficient	0.9690	Hi-Efficient	0.8459	Inefficient	0.9192	Efficient	0.9222	Efficient
Mar. H1-May H2	0.9605	Hi-Efficient	0.9912	Hi-Efficient	0.9690	Hi-Efficient	0.8859	Inefficient	0.9397	Efficient	0.9421	Efficient
Mar. H2-Jun. H1	0.9605	Hi-Efficient	0.9910	Hi-Efficient	0.9692	Hi-Efficient	0.8852	Inefficient	0.9423	Efficient	0.9386	Efficient
Apr. H1-Jun. H2	0.8945	Inefficient	0.9585	Hi-Efficient	0.9332	Efficient	0.9164	Efficient	0.9270	Efficient	0.9885	Hi-Efficient
Apr. H2-Jul. H1	0.8767	Inefficient	0.9782	Hi-Efficient	0.8967	Inefficient	0.9150	Efficient	0.9627	Hi-Efficient	0.9517	Hi-Efficient
May H1-Jul. H2	0.8767	Inefficient	0.9861	Hi-Efficient	0.8891	Inefficient	0.9217	Efficient	0.9696	Hi-Efficient	0.9515	Hi-Efficient

Table 8. Efficiency categories for M3 in the day and night shifts over February-July 2014

	M3 / Day Shift						M3 / Night Shift					
Window	TE Avg.	Category	PTE Avg.	Category	SE Avg.	Category	TE Avg.	Category	PTE Avg.	Category	SE Avg.	Category
Feb. H1-Apr. H2	0.9583	Hi-Efficient	0.9792	Hi-Efficient	0.9786	Hi-Efficient	0.9576	Hi-Efficient	0.9797	Hi-Efficient	0.9773	Hi-Efficient
Feb. H2-May H1	0.9374	Efficient	0.9635	Hi-Efficient	0.9735	Hi-Efficient	0.9283	Efficient	0.9647	Hi-Efficient	0.9630	Hi-Efficient
Mar. H1-May H2	0.9114	Efficient	0.9397	Efficient	0.9705	Hi-Efficient	0.9352	Efficient	0.9647	Hi-Efficient	0.9700	Hi-Efficient
Mar. H2-Jun. H1	0.8862	Inefficient	0.9275	Efficient	0.9560	Hi-Efficient	0.9336	Efficient	0.9717	Hi-Efficient	0.9615	Hi-Efficient
Apr. H1-Jun. H2	0.9063	Efficient	0.9441	Efficient	0.9598	Hi-Efficient	0.9502	Hi-Efficient	0.9857	Hi-Efficient	0.9639	Hi-Efficient
Apr. H2-Jul. H1	0.8858	Inefficient	0.9495	Efficient	0.9340	Efficient	0.9262	Efficient	0.9838	Hi-Efficient	0.9406	Efficient
May H1-Jul. H2	0.9248	Efficient	0.9693	Hi-Efficient	0.9536	Hi-Efficient	0.9219	Efficient	0.9552	Hi-Efficient	0.9652	Hi-Efficient

Table 9. Efficiency categories for M4 in the day and night shifts over February-July 2014

	M4 / Day Shift						M4 / Night Shift					
Window	TE Avg.	Category	PTE Avg.	Category	SE Avg.	Category	TE Avg.	Category	PTE Avg.	Category	SE Avg.	Category
Feb. H1-Apr. H2	0.9703	Hi-Efficient	0.9958	Hi-Efficient	0.9744	Hi-Efficient	0.9755	Hi-Efficient	1.0000	Hi-Efficient	0.9755	Hi-Efficient
Feb. H2-May H1	0.9353	Efficient	0.9789	Hi-Efficient	0.9555	Hi-Efficient	0.9582	Hi-Efficient	0.9953	Hi-Efficient	0.9628	Hi-Efficient
Mar. H1-May H2	0.9441	Efficient	0.9845	Hi-Efficient	0.9593	Hi-Efficient	0.9581	Hi-Efficient	0.9832	Hi-Efficient	0.9748	Hi-Efficient
Mar. H2-Jun. H1	0.9556	Hi-Efficient	0.9841	Hi-Efficient	0.9712	Hi-Efficient	0.9688	Hi-Efficient	0.9825	Hi-Efficient	0.9862	Hi-Efficient
Apr. H1-Jun. H2	0.9473	Efficient	0.9851	Hi-Efficient	0.9618	Hi-Efficient	0.9639	Hi-Efficient	0.9822	Hi-Efficient	0.9816	Hi-Efficient
Apr. H2 -Jul. H1	0.9033	Efficient	0.9753	Hi-Efficient	0.9230	Efficient	0.9661	Hi-Efficient	0.9862	Hi-Efficient	0.9798	Hi-Efficient
May H1-Jul. H2	0.9681	Hi-Efficient	0.9739	Hi-Efficient	0.9940	Hi-Efficient	0.9727	Hi-Efficient	0.9796	Hi-Efficient	0.9930	Hi-Efficient

Table 10. Efficiency categories for M5 in the day and night shifts over February-July 2014

	M5 / Day Shift						M5 / Night Shift					
Window	TE Avg.	Category	PTE Avg.	Category	SE Avg.	Category	TE Avg.	Category	PTE Avg.	Category	SE Avg.	Category
Feb. H1-Apr. H2	0.9819	Hi-Efficient	0.9851	Hi-Efficient	0.9965	Hi-Efficient	0.9299	Efficient	0.9775	Hi-Efficient	0.9510	Hi-Efficient
Feb. H2-May H1	0.9797	Hi-Efficient	0.9841	Hi-Efficient	0.9953	Hi-Efficient	0.9523	Hi-Efficient	0.9888	Hi-Efficient	0.9631	Hi-Efficient
Mar. H1-May H2	0.9604	Hi-Efficient	0.9990	Hi-Efficient	0.9614	Hi-Efficient	0.9410	Efficient	1.0000	Hi-Efficient	0.9410	Efficient
Mar. H2-Jun. H1	0.9645	Hi-Efficient	0.9787	Hi-Efficient	0.9853	Hi-Efficient	0.9272	Efficient	0.9500	Hi-Efficient	0.9761	Hi-Efficient
Apr. H1-Jun. H2	0.9385	Efficient	0.9646	Hi-Efficient	0.9726	Hi-Efficient	0.9272	Efficient	0.9500	Hi-Efficient	0.9761	Hi-Efficient
Apr. H2-Jul. H1	0.9140	Efficient	0.9369	Efficient	0.9747	Hi-Efficient	0.9444	Efficient	0.9653	Hi-Efficient	0.9785	Hi-Efficient
May H1-Jul. H2	0.9346	Efficient	0.9553	Hi-Efficient	0.9774	Hi-Efficient	0.9490	Efficient	0.9698	Hi-Efficient	0.9788	Hi-Efficient

5. Conclusions

The present research study successfully evaluated the efficiency of five blowing machines in a plastics industry using DEA window analysis in both day and night shifts during the period Feb., 2014 to Jun., 2014. The production quantity is set as the output, whereas the defect quantity and idle time (units) are set as the inputs for all windows. The technical, pure technical, and scale efficiency values are then calculated. A comparison is conducted between the day and night shifts for each machine. Moreover, comparisons are performed among the efficiency of the five machines in both day and night shifts. Improvement actions are finally suggested to reduce the inefficiency. It is found that there exist significant differences between day and night shifts for each machine. Thus, managerial as well as operational actions are required to improve the process performance. If the source of inefficiency is due to low PTE, then production engineers should increase the actual production quantity through utilizing the production machine resources, reduce defect quantity through having a reliable quality control system, and/or reduce idle time through improving machine reliability and quality using Total Productive Maintenance (TPM) and quality tools and through reducing overproduction and inventory. On the other hand, if the source of inefficiency is due to low SE, then the production engineer should reconsider and reschedule the allocations of customers' orders, the plant size or the area for storage, and/or purchase new production machines.

The thorough analysis and discussion of the results in the present paper provide a valuable evaluation to production managers for improving the performance of blowing processes.

References

[1] Al-Refaie, O. Ghnaimat, & M.H. Li. "Effects of ISO 9001 certification and KAAE on performance of Jordanian firms." *Jordan Journal of Mechanical and Industrial Engineering*, Vol. 6 (2012), No. 1, 45-53.

[2] Al-Refaie, N. Bata, D. Eteiwi, & I. Jalham, " Examining Factors that Affect Passenger's Overall Satisfaction and Loyalty: Evidence from Jordan Airport. *JJMIE*, *Vol. 8*(2014) No. 2, 94-101.

[3] Al-Refaie, "Optimizing SMT performance using comparisons of efficiency between different systems technique in DEA". IEEE Transactions, Electronic Packaging Manufacturing, Vol. 32(2009) No.4, 256-264.

[4] M. H. Li, A. Al-Refaie, M. Jarbo, C.H. Yeh, 2014, "IDEA approach for solving multi-responses fuzziness problem in robust design" Journal of Quality, Vol. 21(2014) No.6, 455-479.

[5] Al-Refaie, M. H. Li, M. Jarbo, C. H. Yeh,, N. Bata, "Imprecise data envelopment analysis model for robust design with multiple fuzzy quality responses". *Advances in Production Engineering & Management*, Vol. 9 (2014) No.2, 83-94.

[6] Al-Refaie, "Optimizing performance with multiple responses using cross-evaluation and aggressive formulation in data envelopment analysis." *IIE Transactions*, Vol. 44 (2014) No.4, 262-276.

[7] Al-Refaie, "Super-Efficiency DEA approach for optimizing multiple quality characteristics in parameter design". International Journal of Artificial Life Research, Vol. 1(2010) No.2, 58-71.

[8] Al-Refaie, "Optimising correlated QCHs in robust design using principal components analysis and DEA techniques". Production Planning and Control, Vol. 22(2011) No.7, 676-689.

[9] Al-Refaie, M. Al-Tahat, "Solving the multi-response problem in Taguchi method by benevolent formulation in DEA". Journal of Intelligent Manufacturing, Vol. 22(2011) No. 4, 505-521.

[10] Al-Refaie, R. Fouad, M.H. Li, M. Shurrab, "Applying simulation and DEA to improve performance of emergency department in a Jordanian hospital". Simulation Modeling Practice and Theory, Vol. 41(2014) No. 2, 59-72.

[11] W.W. Charnes, A. Cooper, A. Lewin, and L.M. Seiford, "Data Envelopment Analysis: Theory, Methodology, and Application". Third ed., Boston: Kluwer Academic publishers, 1994.

[12] W. W. Cooper, L. M. Seiford, J. Zhu, " Handbook on Data Envelopment Analysis". Boston: Kluwer Academic publishers, 2004.

[13] G.M. Shi, J. Bi, J.N. Wang, "Chinese regional industrial energy efficiency evaluation based on a DEA model of fixing non-energy inputs". Energy Policy, Vol. 38 (2010) No.10, 6172-6179.

[14] W.W. Cooper, L.M. Seiford, J. Zhu "Handbook on Data Envelopment Analysis". Boston: Kluwer Academic publishers, 2003.

[15] S.N. Hwang, T.Y. Chang, "Using data envelopment analysis to measure hotel managerial efficiency change in Taiwan". Tourism Management, Vol. 24(2003) No. 4, 357-369.

[16] T. Ertay, D. Ruan, "Data envelopment analysis based decision model for optimal operator allocation in CMS". EJOR, Vol. 164 (2005) No. 3, 800-810.

[17] G. Halkos, N. Tzeremes, "Exploring the existence of Kuznets curve in countries' environmental efficiency using DEA window analysis". Ecological Economics, Vol. 68 (2009) No. 1, 2168-2176.

[18] W.W. Cooper, L.M. Seiford, K. Tone "A Comprehensive Text with Models, Applications, References and DEA-Solver Software". Boston: Kluwer Academic publishers, 2000.

[19] C.-J. Chen, H.-L. Wu, B.W. Lin, "Evaluating the development of high-tech industries: Taiwan's science park". Technological Forecasting & Social Change, Vol. 73(2006) No. 4, 452-465.

[20] J.L. Hu, S.C. Wang, "Total-factor energy efficiency of regions in China". Energy Policy, Vol. 34 (2006) No.17, 3206-3217.

[21] Zhang, J. Bi, Z. Fan, Z. Yuan, J. Ge, " Eco-efficiency analysis of industrial system in china: A data envelopment analysis approach". Ecological Economics, Vol. 68 (2008) No. 1-2, 306-316.

[22] M. Asmild, J. Paradi, V. Aggarwall, C. Schaffnit, " Combining DEA window analysis with the Malmquist index approach in a study of the Canadian banking industry. Journal of Productivity Analysis, Vol. 21 (2004) No. 1, 67-89.

[23] W. W. Cooper, L. M. Seiford, K. Tone, J. Zhu, " Some models and measures for evaluating performances with DEA: past accomplishments and future prospects". Journal of Productivity Analysis, Vol. 28 (2007) No. 3, 151-163.

[24] M. Pulina, C., Detotto, A. Paba, "An investigation into the relationship between size and efficiency of the Italian hospitality sector: A window DEA approach". European Journal of Operational Research, Vol. 204 (2010) No. 3, 613-620.

[25] H.H. Yang, C.-Y. Chang, "Using DEA window analysis to measure efficiencies of Taiwan's integrated telecommunication firms". Telecommunications Policy, Vol. 33 (2009) No.1-2, 98-108.

[26] Hemmasi, M. Talaeipour, H. Khademi-Eslam, R. Farzipoor, S.H. Pourmousa, " Using DEA window analysis for performance evaluation of Iranian wood panels industry". African Journal of Agricultural Research, Vol. 6 (2011) No. 7, 1802-1806.

[27] X.P. Zhang, Cheng, X.-J. Gao, "Total-factor energy efficiency in developing countries". Energy Policy, Vol. 39 (2011) No.2, 644-650.

[28] Z.H. Wang, H.L. Zeng, Y.M. Wei, Y.-X. Zhang, " Regional total factor energy efficiency: An empirical analysis of industrial sector China". Applied Energy, Vol. 97 (2012) No. 1, 115-123.

JJMIE

Volume 10 Number 1, March.2016
ISSN 1995-6665
Pages 39- 49

Jordan Journal of Mechanical and Industrial Engineering

Optimal Design of PV System in Passive Residential Building in Mediterranean Climate

Samar Jaber[a *], Ali Abul Hawa[b]

[a] Mechanical Engineering Department, American University of Madaba, Madaba – Jordan

[b] Eectrical Engineering Department, American University of Madaba, Madaba – Jordan

Received 31 March 2015 Accepted 22 Oct 2015

Abstract

Energy is a crucial element for prosperity and improving the standard of living. Fossil fuels are not an everlasting source of energy. However, the sun is the only eternally sustainable source of energy.

In this the present study, feasibility and reliability analyses of a PV grid-connected system are conducted in Mediterranean climate. MATLAB is used to model the energy system and examine its technical and economic performances. Life Cycle Cost (LCC) and Payback Period (PbP) criterion are also used to determine the optimum system design.

The present study shows that incorporating an optimum system of solar PV with a grid system (oriented at 26° from the horizontal) is feasible in Mediterranean region. It can reduce 6,075 kWh (83.7%) from the annual electricity bill. Moreover, LCC over a 30-year period is found to be US$ 19,524 while the PbP for the initial investment is 5.88 years. Furthermore, carbon dioxide emissions, associated with thermal power plants generated electricity, are expected to reduce by about 3.6 Tons annually. Thus, to move toward energy independence and energy security, favorable policies and incentives should be set to accelerate the use of such energy systems.

Keywords: *Energy; Grid-Connected; Optimization; Life Cycle Cost.*

1. Introduction

There are two global problems facing the scientific community; the first is the main source of energy, fossil fuels, is being rapidly exhausted. The second problem concerns the environment, where the combustion of hydrocarbon fuels has deteriorating effects on the environment. Therefore, there is an urgent need to use renewable energy instead of fossil fuels [1].

The total primary energy consumption was 7.979 M TOE in 2012, which cost around 6.52 Billion US Dollars (USD). Most of the energy used in buildings is in the form of electricity. Statistical studies showed that the residential sector consumed 43% of the total electricity consumption in Jordan in 2012 [2]. "On the other hand, Jordan has abundant supplies of solar energy, which is relatively high with an average daily solar radiation of 5.5 kWh/m^2. The average annual sunshine days are about 300 days. Thus, the need for passive and climatic design, energy efficiency measures, and utilizing renewable energy has emerged" [3].

Hammad *et al.* [4] presented a full description of a pilot photovoltaic station with thin-film modules on the Hashemite University campus. The pilot station is installed and tested as a canopy covering four car parking slots. The results showed that system efficiency is within the normal range for this type of tested technology in other countries.

Hybrid systems, such as wind/solar-Diesel, PV-Diesel with battery as a backup, are being used in urban and remote areas for uninterrupted power generation and meeting the energy demands in summer [5-9]. These studies recommended to use such system.

Solar Photovoltaic reduces the environmental impact of burning fossil fuels. The potential of using solar photovoltaic system for industrial processes was discussed by Iyappan *et al.* [10].

The hybrid power systems either as standalone or on-grid systems are more reliable and cheaper than single source energy systems [11, 12]. Moreover, it is showed in a number of studies that the hybrid power system could produce fewer greenhouse gases when compared with fossil-fuel conventional energy systems [11-13].

The main goal of the present study is to investigate the techno-economic viability of solar PV grid-connected energy system for a passive Jordanian household. A MATLAB code is written to simulate the hourly performance of a PV-grid interconnected system throughout the year. The simulation code is used to find the optimum size of the PV system at minimum Life Cycle

* Corresponding author e-mail: s.jaber@aum.edu.jo.

Cost (LCC). In addition, optimum PV array tilt angle is determined by analyzing the optimum energy gain throughout the year. Finally, the amount of CO_2 emission reduction due to the optimization is calculated.

2. Design Parameters

PV system sizing and performance strongly depend on electrical demand and metrological variables such as solar energy and ambient temperature. Therefore, to optimize a PV system, extensive studies related to the metrological variables have to be done [14].

The selected building is a passive Jordanian building located in Amman, location of the building is shown in Figure 1.

Figure 1. Building Location

2.1. Metrological Data

Amman, the capital city of Jordan, has a mountainous topography and lies in the "global Sunbelt" at a latitude of 31.93° North and a longitude of 36° East. This location has abundant supplies of solar energy, with a relatively high average daily solar radiation. The annual sunshine is more than 300 days [15].The climate of Amman is predominantly of the Mediterranean type. It is marked by sharp seasonal variations in both temperature and precipitation. The climate can be cold to very cold in winter and warm to hot in summer. Summer starts around mid of May and winter starts around mid of November, with two short transitional periods in between (autumn and spring).

The yearly average temperature is 17.2°C, with lowest mean temperature of 3.6°C in January and highest mean temperature of 32.6°C in August. Figure 2 represents the hourly outdoor temperature profile all over the year [16].

The highest solar radiation is 7.56 kWh/m^2.day in June, while the lowest solar radiation is 2.71 kWh/m^2.day in December [16]. Figure 3 reflects that Amman has a very good solar energy potential, which makes PV systems a practical solution for this region.

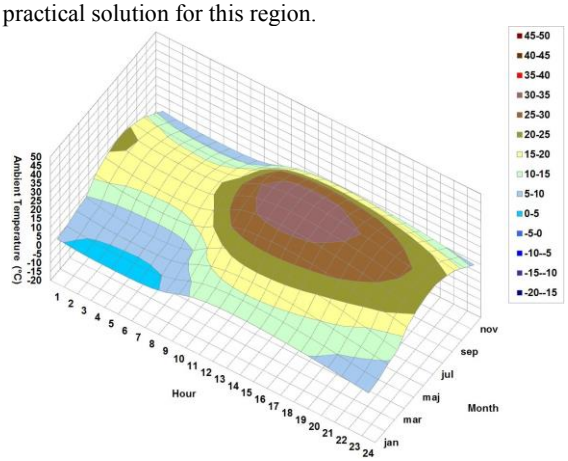

Figure 2. Outdoor Temperature Profile

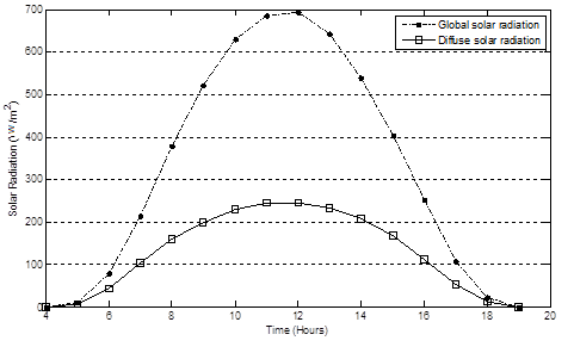

Figure 3. Average Daily Global and Diffuse Solar Radiations onto horizontal for Amman

2.2. Electric Demand

To begin sizing a PV system, the energy consumption is determined as indicated in Table 1, which lists most electrical devices and their daily consumption in a passive household in Amman. In the present study, the hourly demand is used in calculating the optimum size of the PV system. The simulated hourly demand profile has been simulated in MATLAB. It varies from one day to another throughout the year, since the energy consumption of a building varies according to the period of the year, the compartmental behavior and so on.

From Table 1, the total daily AC demand is about 20.4 kWh. Taking into consideration the efficiency of the inverter (94%), the daily DC demand is about 21.7 kWh. Furthermore, the peak AC power demand is about 10.95 kW.

Table 1. Household Appliances and Lighting Load

Demand	Power (W)	Total Peak (kW)	Usage (Hour/day)	kWh/day
Energy Saving Lamps × 15	11	0.165	7	1.155
TV set × 2	100	0.200	10	2.000
Satellite TV System × 2	15	0.030	10	0.300
Computer × 2	90	0.180	10	1.800
Refrigerator	150	0.150	10	1.500
Water Cooler/Heater	400	0.400	6	2.400
Hair dryer	1000	1.000	0.2	0.200
Iron	1500	1.500	0.5	0.107
Microwave	900	0.900	0.2	0.180
Water Heater	1200	1.200	1	1.200
Vacuum Cleaner	1000	1.000	0.3	0.129
Battery Charger × 4	2	0.008	0.5	0.004
Air Conditioning × 3	1005	3.014	3	9.043
Washing machine	1200	1.200	1	0.343
Total		10.947		20.361

2.3. PV System Design

The optimization of two PV system types has been discussed in the open literature; firstly, a stand-alone (off-grid) system [17-23], which is mostly used in remote areas as an isolated small power generation for essential electric power [24-33]. This system is shown in Figure 5;

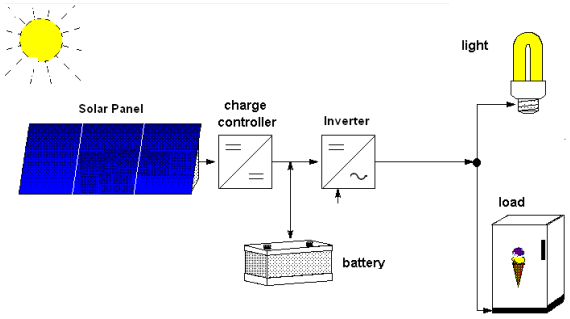

Figure 5. Stand-alone system Components

secondly, a grid-connected PV system [34-37], as shown in Figure 6. This system is used in areas with a grid system; energy storage facility can be removed, and instead, the grid system can be used as storage. PV energy storage system produces more energy than needed; the surplus energy is fed into the grid and, energy is taken from the grid when the PV system produces less energy than needed as outlined by Mondal and Islam [38].

A grid-connected PV system reduces the amount of purchased electricity from the utility each month. In addition, it reduces the capital cost of the system due to not using of batteries.

In the past, hybrid systems were selected as the prioritized choice for remote systems, especially at sites far away from conventional power system [39-42]. Nowadays, there is a trend to update an existing hybrid system for grid-connection applications [43].

In order to design a suitable grid-connected PV system a numerical method will be used. The numerical method is the most used method for sizing hybrid PV system [44]. This process starts by modeling the system using mathematical relations and then using a weather data and demand. Then, the calculation is performed. During the simulation, the amount of the generated energy each time step, usually a day or an hour, is predicted and compared with the demand. After that, the cost of each part of the system is calculated and based on the minimum LCC (capital cost, operating and maintains cost and salvage cost), the optimum system size is determined.

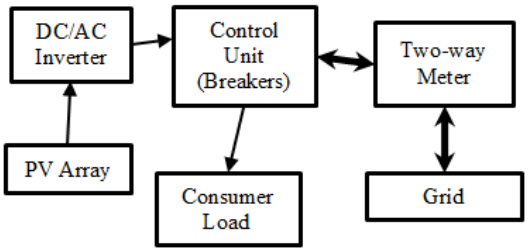

Figure 6. Block diagram of PV grid-connected system

2.3.1. PV Array Sizing

A mono-crystalline silicon PV module is selected in a different situation in order to find the optimum position, and to avoid shade. The module specification is listed in Table 2.

Table 2. Technical specification of PV module under nominal operating cell temperature [45]

Parameter		**Specification**
Nominal maximum power		300 Wp
Voltage at nominal power		36.58 V
Current at nominal power		8.21 A
Open-circuit voltage		45.36 V
Short-circuit current		8.78 A
Efficiency, η_{PV}		15.4 %
Operating module temperature		-40 to +85°C
Temperature coefficients:	Pmax	-0.41 %/°C
	Voc	-2.11 mV/cell°/C
	Isc	4.62 mA/cell/°C
Dimension		1965 mm × 990 mm × 45 mm

The number of panels is determined according to energy demand and its initial cost. The optimum number of panel is designed using MATLAB based on simulated hourly demand.

The hourly energy taken from the grid (E_{Grid}) in kWh is calculated taking into consideration the inverter efficiency (η_{inverter}) of 94%. In addition to losses due to system components, and high normal operating PV cell temperature, which are represented by a typical Safety Factor (S.F) of about 20%, thus,

$$E_{Grid} = E_{Demand} - E_{PV} \quad (1)$$

where, E_{PV} is the total energy generated from the PV array (kWh), E_{Demand} is the demand seen by the PV array (kWh) and it is calculated based on Figure 5 as follow:

$$E_{Demand} = \sum \frac{\text{Simulated Hourly Demand} \times \text{S.F}}{\eta_{\text{inverter}}} \quad (2)$$

It can be noticed from equation (1) that the energy taken from the grid could be positive or negative or zero. A negative value indicates an excess PV energy that is fed to the grid. Furthermore, the net energy taken from the grid is used in calculating the energy bill at the end of each month.

2.3.2. Inverter Sizing

The inverter input voltage is 12 V, so the total AC Ampere hours per day (Ah/day) used by AC demand is

$$\text{Total Ah/day used by AC Demand} = \frac{\text{Total AC Demand}}{\text{Inverter Input Voltage}} \quad (3)$$

3. Optimal Sizing Of PV Tilt Angle

The tracking system is a mechanical device used to maximize the solar energy intake by changing the tilt angle of PV panels as the sun sweeps across the sky automatically. Using tracking systems is costly, as they require energy for their operation and are not always applicable [46]. Therefore, it is often practical to orient the solar collector at an optimum tilt angle and correct the tilt angle manually from time to time. Thus, hourly, daily, monthly, seasonal or yearly changing the tilt angle for a PV system could be more feasible than applying an active sun tracker. It is reported in the literature that, in the northern hemisphere, the optimum orientation is south facing, and the optimum tilt angle depends only on the location latitude. Researchers did not define any value for the optimum tilt angle. The open research shows that there is a wide range of optimum tilt angle for precise locations as recommended by different researchers [47-56].

In general, solar radiation data are described in terms of incident global solar radiation, solar energy is one of the combinations of the global, direct (beam), diffuses, and ground reflected solar energy. To calculate the solar energy on a tilted surface, the solar energy on a horizontal surface and geometrical models are considered. The following equation describes solar energy components on a tilted surface mathematically [57]:

$$G_{TLT} = (G - D)R_B + DR_D + G\rho R_R \quad (4)$$

where G_{TLT} is the solar radiation on a tilted surface (kWh/m2). G and D are the ground solar radiation (kWh/m2) and the diffuse solar radiation (kWh/m2), respectively. ρ is the Albedo ground reflection, which equals around 0.3 for a ground similar to Amman [58]. R_B,R_D, and R_R are radiation coefficients.

$$R_B = \frac{\cos(L-\beta)\cos\delta\cos\omega_{ss} + \sin(L-\beta)\sin\delta}{\cos L\cos\delta\cos\omega_{ss} + \sin L\sin\delta} \quad (5)$$

where L is the location latitude (rad), β is the tilt angle (rad), and ω_{ss} is the hour angle (rad).

The declination angle (δ) is calculated from [58]:

$$\delta = 23.45\sin\left(360\frac{284+n}{365}\right) \quad (6)$$

where n is the day number in the year ($n = 1{:}365$)

The amount of reflected solar energy on a tilted surface, R_R, can be calculated as [57]:

$$R_R = \frac{1-\cos\beta}{2} \quad (7)$$

The geometric factor R_D is defined as the ratio of the diffuse solar energy on the tilted surface to that on the horizontal surface at any time. Many solar models, classified as isotropic and anisotropic, have been used to estimate R_D. Isotropic solar models are based on the hypothesis that isotropic radiation has the same intensity regardless of the direction of measurement, and an isotropic field exerts the same action regardless of how the test particle is oriented. One of the most famous isotropic diffuse solar models is the Liu and Jordan model [59] with R_D being formulated as:

$$R_D = \frac{1+\cos\beta}{2} \quad (8)$$

By substituting Eqs. (5, 7, 8) into Eq. (4) a mathematical model can be obtained, based on the Liu and Jordan model, for calculating the optimum tilt angle. A code is written by using multidimensional arrays and MATLAB's built-in functions to find optimum tilt angle. Fig.7 shows the algorithm for calculating the optimum tilt angle, numbers in brackets show array sizes.

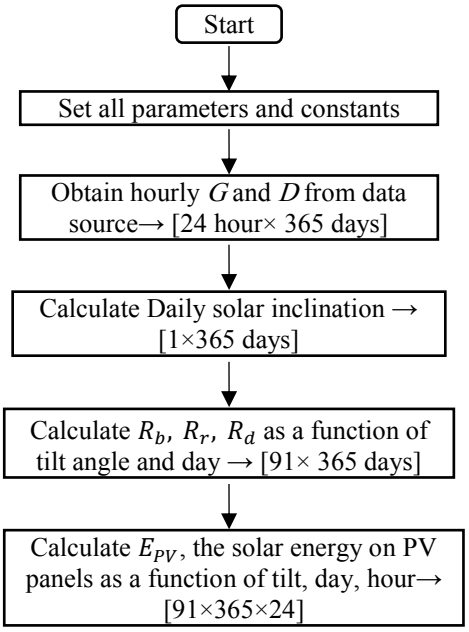

Figure 7. Tilted Solar Radiation Flow Chart

The MATLAB code calculates the tilted solar radiation as a function of hour, day, and tilt angle ($0° < \beta < 90°$), having a 24 by 365 matrix. Then, the optimum tilted solar radiation with respect to tilt the angle is set to design a PV system accordingly.

4. Life Cycle Cost Analysis

Today, the life span of a typical PV system reaches 30 years. In order to observe the financial benefits of the PV on-grid system, a 30-year life-cycle-analysis is performed. With a grid connected PV system that does not include batteries, the electric energy fed to the grid and that consumed from the grid are taken into account.

The following equation describes the Life Cycle Cost (LCC) function for the PV system (Duffie and Beckman):

$$LCC = C_{PV}\left[1 + (f_{O.M} \times PWF) - \left(f_{salv}\left(\frac{1+i}{1+r}\right)^{N}\right)\right] + (C_{Grid} \times PWF) \quad (9)$$

where C_{PV} is the initial cost of the PV system, $f_{O.M}$ is the operation and maintenance factor set at 5% of the capital cost, f_{salv} is the salvage factor set at 6% of the capital cost (according to local figures).

According to Jordanian market, the inflation rate, r, in fuel prices is around 8.9%, and the interest rate, i, is about 6.25% [60], N is the life span, PWF is the Present Worth Factor calculated according to the following equation:

$$PWF = \frac{1+i}{r-i}\left[1 - \left(\frac{1+i}{1+r}\right)^{N}\right] \quad (10)$$

C_{Grid} is the annual grid electricity cost, assuming a monthly billing system. Current electricity prices in Jordan are calculated monthly based on a slab tariff as shown in Table 3.

Table 3. Slab Tariff [61]

	Energy Consumption (kWh/Month)	Tariff (US cent/kWh)
Slab 1	0-160	46
Slab 2	161-300	101
Slab 3	301-500	121
Slab 4	501-600	161
Slab 5	601-750	199
Slab 6	751-1000	237
Slab 7	>1000	331

In the present study, the optimum area of a PV array is found by determining the minimum LCC of the PV system. A MATLAB program is used to calculate the LCC of PV systems ranging from 1 to 16 panels. The minimum LCC corresponds to the optimum number of PV panels. The program is described by the flow diagram shown in Figure 8, where the brackets indicate the matrix sizes.

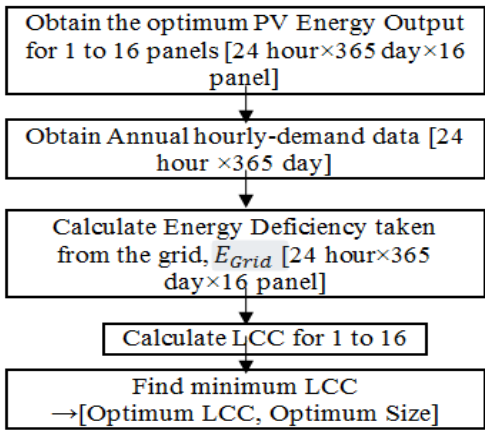

Figure 8. LCC Flow Chart

The Payback Period (PbP) is the length of time it takes for an initial investment to be repaid out of the net cash inflows from the project [62]. At the end of PbP, the system has paid for the initial investment and any revenue produced thereafter is pure gain. Thus, PbP in years is equal to:

$$\text{PbP} = \frac{\text{Initial Cost of PV system}}{\text{Annual Saving of PV system}} \quad (11)$$

5. Results

5.1. Optimal Sizing Of PV Tilt Angle

The magnitude of the solar radiation can be increased by a simple manipulation of the the panel tilt angle. To decide which angle is the optimum at the selected location, the monthly solar radiation, as a function of the tilt angle ($0° < \beta < 90°$), is simulated and plotted in Figure 9.

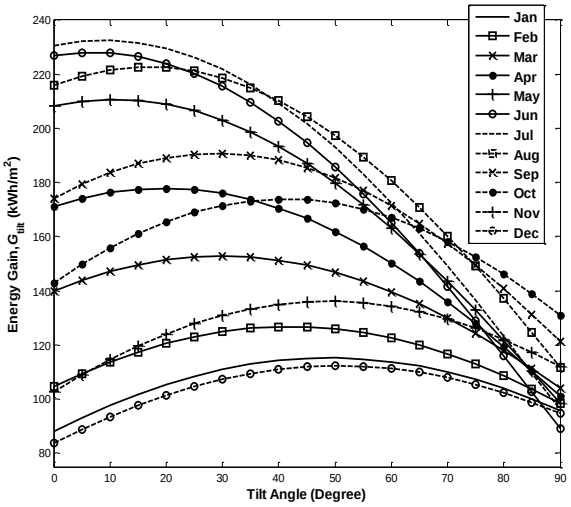

Figure 9. Monthly solar radiation gain vs. tilt angle

Figure 9 shows that the hot months (May – Aug.) have a small optimum tilt angles while the cold months (Jan – April and Sep. – Dec.) have a large optimum tilt angle. This is due to the location of the sun; in hot months, the sun is located at the highest point in the horizon where in cold months the sun is located at the lowest point. In this study, the gain obtained by adjusting the tilt angle of a PV panel is investigated for monthly, quarterly, biannual and annual (fixed) periods in order to determine the optimum tilt angle and solar energy yield. The monthly adjustment

assumed that the tilt angle is changed from month to month twelve times a year. The quarterly adjustment considers that the PV panel tilt angle is adjusted seasonally four times annually, whereas the biannual adjustment assumes that Amman has two climate seasons, so the tilt angle is adjusted twice a year. The annual adjustment means that the system will be sloped at fixed tilt angle during the lifetime of the PV system. The results are listed in Tables 4, 5, and 6 for monthly, quarterly, and bi-annual adjustment, respectively.

Table 4. Monthly optimum tilt angle

Month	β degree	G_{TLT} kWh/m^2	G_0 kWh/m^2	Energy Gain %
Jan.	49	115.3	88.1	30.9
Feb.	42	126.8	104.7	21.2
Mar.	30	152.9	139.9	9.2
Apr.	20	177.9	171.2	3.9
May	11	210.7	208.2	1.2
June	7	228.0	226.8	0.5
July	9	232.4	230.4	0.9
Aug.	17	222.7	215.9	3.2
Sep.	29	190.8	174.2	9.5
Oct.	41	173.9	143.0	21.7
Nov.	49	136.2	102.8	32.6
Dec.	51	112.3	83.9	33.9
	Total	2080	1889	10.1

Table 4 represents the optimization results of a monthly solar radiation on both slanted panel (G_{TLT}) and horizontal panel (G_0). The results show that the monthly tilt angle value varies between $7° - 51°$. The maximum tilt angle value is on December while the minimum tilt angle value occurs on June. The energy gain is increased on December by an amount of 33.9 % as compared with a horizontal panel. Moreover, the energy gain is increased by only 0.5 % on May. On the other hand, as an overall result, an increase of 10.1 % in the energy gain, as compared to the horizontal panel, is achieved by applying the monthly tilt angle adjustment.

Table 5 shows that the optimum tilt angle is 14° and 15° in the period of (21/03–21/06) and (22/6-21/9), respectively. Meanwhile, it is 44° for the period 22/09–21/12, and it is one degree less in the period of 22/12 – 20/3. However, the quarterly tilt angle optimization leads to an energy gain of 9.6 % as compared with PV horizontal panel.

Table 5. Quarterly optimum tilt angle

Period	β degree	G_{TLT} kWh/m^2	G_0 kWh/m^2	Energy Gain %
21/3-21/6	14	600.8	589.3	2.0
22/06-21/09	15	660.1	643.6	2.6
22/09-21/12	44	434.4	347.8	24.9
22/12-20/3	43	375.2	308.3	21.7
	Total	2071	1889	9.6

Table 6 represents that the slanting of the PV panel at 15° in the period of 21 March to 21 September and 43° for the period 22 September to 20 March, gains the energy by 9.6% as compared to the horizontal surface.

Table 6. Bi-annual optimum tilt angle

Period	β degree	G_{TLT} kWh/m^2	G_0 kWh/m^2	Energy Gain %
21/3-21/9	15	1260.8	1232.8	2.3
22/09-20/3	43	809.6	656.1	23.4
	Total	2070.4	1888.9	9.6

Both Table 5 and Table 6 show an interesting result, the overall energy gain either for quarterly or biannual strategies optimum tilt angle is the same. In addition, Table 6 shows that energy gain in the period of 22 September to 20 March is higher than the energy gain in the period of 21 March to 21 September by 90% (about ten times).

The solar energy gain per each fixed tilt angle for the whole year is shown in Figure 10. The optimum tilt angle is found out to be 26°. The solar energy gain is equal to 2028 kWh/m^2. This increases the solar energy by 7.4%, as compared to the solar energy gain collected by a horizontal surface.

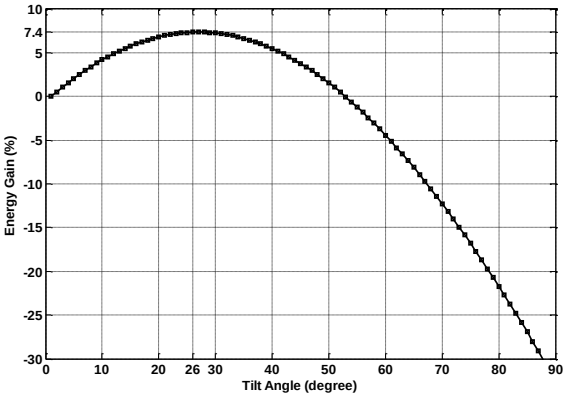

Figure 10. Energy gain according to varying tilt angle

From the previous results, it is clear that the monthly adjustment of tilt angle is the best strategy with an energy gain of 10.1% followed by the quarterly and the biannual techniques. The worst strategy of tilt angle adjustment is an annual (fixed) tilt angle whereas the energy gain value for this strategy is about 7.4%.

It is worth noting that for offline remote household, an adjustment system would have an enormous impact on the solar system efficiency. However, it is apparent that a monthly tilt angle adjustment has a negligible gain compared to the adjustment system cost and maintenance. Therefore, slanting the PV panels by 26° (latitude -6°) for the whole year time is the optimum, which increases the solar energy yield by 7.4%.

5.2. Optimal Sizing of PV System

In order to make the PV systems more feasible, a grid-connected PV system is considered. This system offers users both economic and environmental advantages. Where utility power is available, users can use a grid-connected PV system to supply a portion of the power they need while using utility-generated power at night and on very cloudy days.

For a monthly billing system, Figure 11 shows the amount of energy obtained from the grid each month as the

number of PV panels is varied from 1 to 16. The monthly auxiliary energy needed from the grid is indirectly

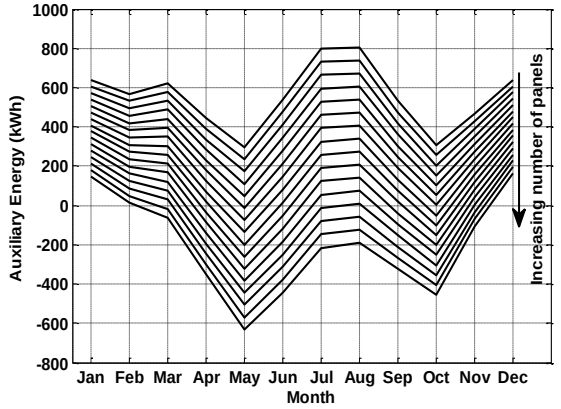

Figure 11. Monthly Auxiliary Energy needed from the grid versus number of panels

Figure 12 shows the grid energy use and the annual percent energy savings, system cost, and LCC as a function of the number of PV panels. Using LCC analysis, the optimum number of PV panels with the specifications in Table 2 is found to be ten panels. The total cost of the optimum PV system is US$ 4,056, while the life cycle cost over a 30-year period is determined to be US$ 19,524.

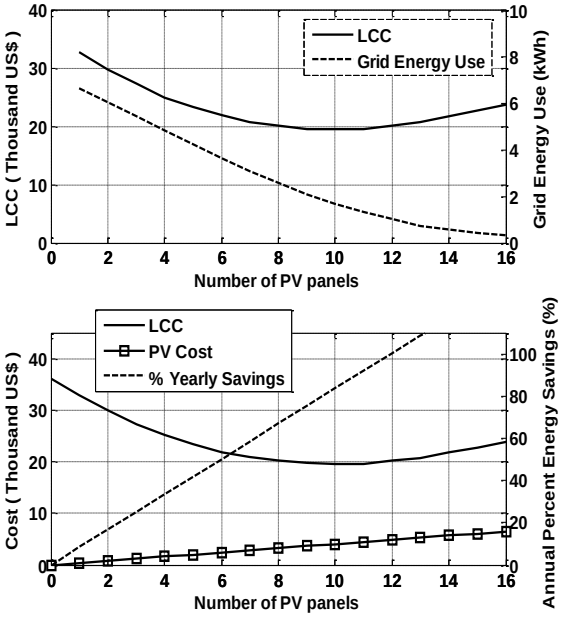

Figure 12. LCC Analysis for different PV System sizes

The electricity generated by the PV-grid energy system and the corresponding electricity consumed by the users (when the cost of PV is US$ 1,352 per kWp and global solar radiation is 5.5 kWh/m^2/day) is shown in Table 7. The total electricity produced by the energy system is 7,261 kWh/year which comprises of 6,075 kWh/year (83.7%) from the solar PV and 1,186 kWh/ year (16.3%) from the grid.

Table 7. Electricity generated by the solar

	Annual Production	
	kWh	%
Solar PV	6,075	83.7
Grid purchases	1,186	16.3
Total	7,261	100

Figure 13 represents the LCC reduction as a function of a number of PV panels as compared with energy cost from grid, calculated as follow:

$$\text{LCC}\,\% = \frac{\text{LCC}(1{:}16)] - \text{Energy cost from grid} * \text{PWF}}{\text{Energy cost from grid} * \text{PWF}} \times 100 \quad (12)$$

From this figure, it is determined that the minimum LCC occurs for a 10-panel solar system.

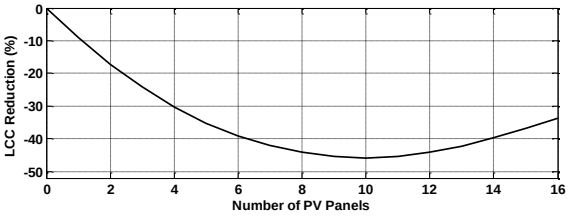

Figure 13. LCC reduction as a function of the number of PV panels

The relationship between the payback period and the number of panels is linear, as shown in Figure 14. The payback period for an optimum sized system is 5.88 years.

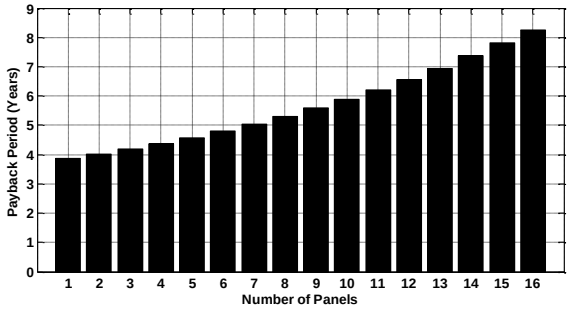

Figure 14. Payback period analysis for different PV System

The monthly average electric energy produced by the PV array is presented in Figure 15. The monthly and seasonal variations in electricity produced by PV system and the grid contribution can be observed from this figure. This is due to the variability in the monthly global solar radiation. The maximum monthly energy generated by the solar PV is about 675 kWh in July, and the minimum is about 315 kWh in December.

The monthly energy purchased from and sold to the grid is presented in Table 8. It can be seen from this table that the quantity of the electricity purchased varies from 179 kWh in May, when the load is low and the PV produced a relatively high amount of electricity, to 519 kWh in August when the load rises sharply due to the increased usage of AC in the hottest month of the summer. Similar variations in the electricity sold to the grid can also be observed from this table.

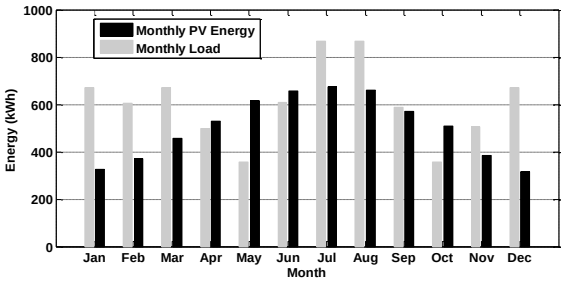

Figure 15. Monthly distribution of the electricity produced by the energy system

Table 8. Monthly distribution of the electricity produced by the energy system with optimum parameters

Month	Energy Purchased (kWh)	Energy Sold (kWh)
Jan.	472	128
Feb.	396	161
Mar.	422	210
Apr.	290	325
May	176	436
June	329	380
July	503	313
Aug.	519	313
Sep.	362	344
Oct.	220	371
Nov.	346	224
Dec.	490	133
Annual	4,525	3,339

Figure 16 shows the performance of the proposed system throughout the year. a snapshot showing zoomed in details of a 4-day period between the 50th and the 53rd day of the year is shown in Figure 17.

In addition to its economic savings, the PV system's main purpose is to protect the environment; the annual savings after installing a PV system for the chosen demand is around 6,075 kWh. In addition, the PV system will reduce around 3.6 Tons of CO_2 emissions annually [63].

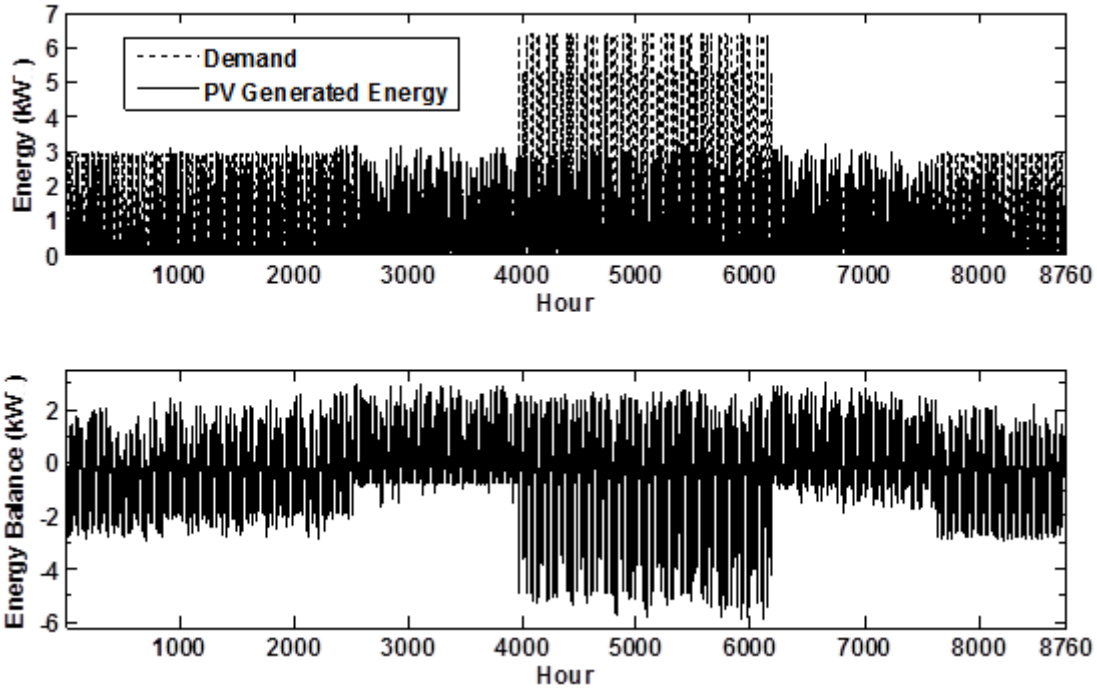

Figure 16. Designed system performance

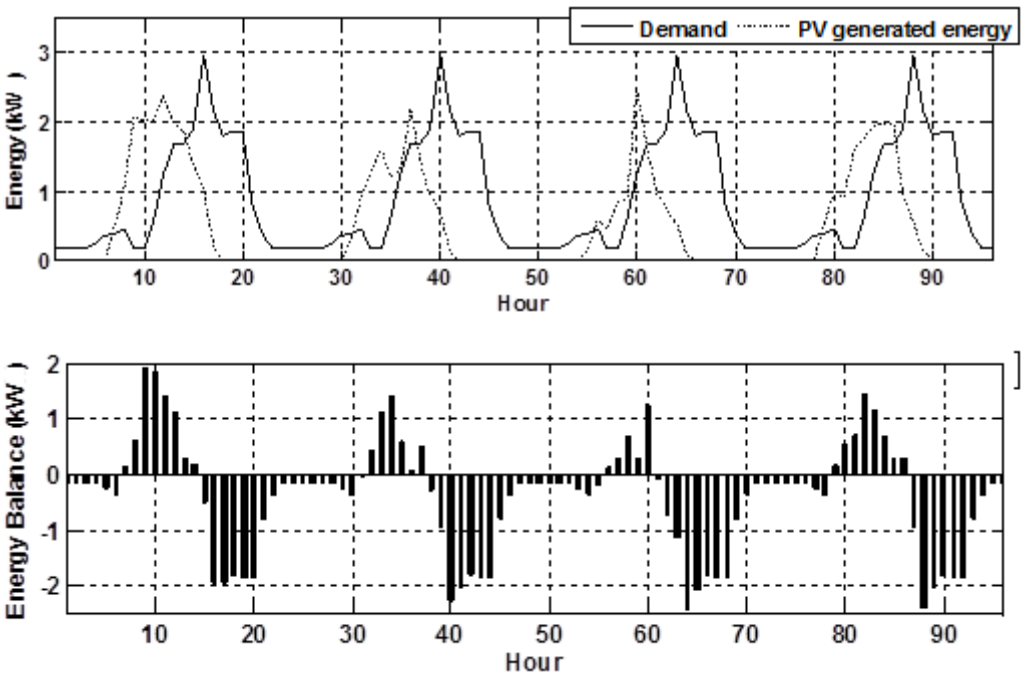

Figure 17. Four-day sample of hourly performance of the proposed system

6. Conclusion

As part of electrical energy can be produced by renewable means, and while the principal advantage of PV is the production of environment, it is a good chance to use alternative energy options before the supply of fossil fuels is depleted, and the damage to the environment is irreversible. The presented results are quite detailed and include, besides the optimum PV panel tilt angle, the simulation and the optimum sizing of the system in Mediterranean climate. It also presents a cost analysis of several years, and the system's behavior on an hourly basis.

With the rapid population growth and the increase in the various economic activities, more energy is consumed; to identify the impacts of the amount of saving, the macroeconomic analysis should be considered. Once only 100 houses in Jordan generate electricity by solar systems, around 607.5 MWh will be saved annually, and about 360 Tons of CO_2 emissions will be reduced. As PWF at 6.25% interest rate and inflation rate of 8.9% after 30 years, the total saving in the energy bill, during 30-years, is about US$ 3.4 million that will strengthen the local economy. Once the output of the present research is expanded to all the Mediterranean region, a superior economic and environmental benefits will be achieved.

References

[1] Abul Hawa A. Investigation of Control Problems of the PEM Fuel Cell for Variable Power Demand. UK: Coventry University; 2010.

[2] MEMR. Facts and Figures. Amman – Jordan: Ministry of Energy and Mineral Resources; 2013.

[3] S. Jaber, S. Ajib, "Optimum, technical and energy efficiency design of residential building in Mediterranean region". Energy and Buildings, Vol. 43 (2011) No. 8, 1829-1834.

[4] B. Hammad, S. Rababeh, M. Al-Abed, A. Al-Ghandoor, "Performance Study of On-Grid Thin-Film Photovoltaic Solar Station as a Pilot Project for Architectural Use". Jordan Journal of Mechanical and Industrial Engineering, Vol. 7 (2013) No. 1, 1-9.

[5] A. Srinivasan, K. Thomachan, "Photovoltaic panel-generator based autonomous power source for small refrigeration units". Solar Energy, Vol. 56 (1996) No. 6, 543-552.

[6] F. Martins, R. Ruther, E. Pereira, S. Abreu, "Solar energy scenarios in Brazil. Part two: Photovoltaics applications". Energy Policy, Vol. 36 (2008) No. 8, 2865- 2877.

[7] F. Ernest, A. Matthew, "Feasibility of solar technology (photovoltaic) adoption: A case study on Tennessee's poultry industry". Renewable Energy, Vol. 34 (2009) No. 3, 748-754.

[8] A. Campoccia, L. Dusonchet, E. Telaretti, G. Zizzo, "Comparative analysis of different supporting measures for the production of electrical energy by solar PV and Wind systems: Four representative European cases". Solar Energy, Vol. 83 (2009) No. 3, 287-297.

[9] N. Pragya, R. Nema, R. Saroj, "A current and future state of art development of hybrid energy system using wind and PV-solar: A review". Renewable and Sustainable Energy Reviews, Vol. 13 (2009) No. 8, 2096-2103.

[10] K. Iyappan, L. Suguna, N. Chandrababu, "Integration of solar photovoltaic power for wet tanning process application in leather industry". Journal of Scientific & Industrial Research, Vol. 1 (2012) No. 3, 118 - 123.

[11] M. Adaramola, S. Paul, O. Oyewola, "Assessment of decentralized hybrid PV solar-diesel power system for applications in Northern part of Nigeria". Energy for Sustainable Development, Vol. 19 (2014), 72–82.

[12] J. Tang, B. Ye, Q. Lu, D. Wang, J. Li, "Economic analysis of photovoltaic electricity supply for an electric vehicle fleet in Shenzhen, China". International Journal of Sustainable Transportation, Vol. 8 (2014), No. 3, 202–224.

[13] A. Hossam-Eldin, A. El-Nashar, A. Ismaiel, "Investigation into economical desalination using optimized hybrid renewable energy system, International Journal of Electrical Power & Energy System". Vol. 43 (2012) No. 1, 1393–1400.

[14] T. Khatib, "Review of designing, installing and evaluating standalone photovoltaic power systems". Journal of Applied Sciences, Vol. 10 (2010), 1212–1228.

[15] Taher A., Abdalla N., Jaber S., Shahin W. Report on analysis of the political, socio-economic and climatic conditions in the Mediterranean countries. Amman – Jordan: National Energy Research Center; 2009.
[16] Doppelintegral-GmbH. INSEL Users Manual-MS Windows. Stuttgart – Germany; 2009.
[17] R. Dufo-López, J. Bernal-Agustín, "Design and control strategies of PV–diesel systems using genetic algorithms". Solar Energy, Vol. 79 (2005), 33–46.
[18] G. Seeling-Hochmuth, "A combined optimisation concept for the design and operation strategy of hybrid-PV energy systems", Solar Energy, Vol. 61, (1997) 77–87.
[19] S. El-Hefnawi, "Photovoltaic diesel-generator hybrid power system sizing". Renewable Energy, Vol. 13 (1998), 33 - 40.
[20] M. Ashari, C. Nayar, "An optimum dispatch strategy using set points for a photovoltaic (PV)–diesel battery hybrid power system". Solar Energy, Vol. 66 (1999), 1 - 9.
[21] S. Rehman, L. Al-Hadhrami, "Study of a solar PV-diesel-battery hybrid power system for a remotely located population near Rafha". Energy, Vol. 35 (2010), 4986–4995.
[22] S. Kumar, N. Phuangpornpitak, "PV hybrid systems for rural electrification in Thailand". Renewable and Sustainable Energy Reviews, Vol. 11 (2007), 1530 - 1543.
[23] C. Ajan, S. Ahmed, H. Ahmad, F. Taha, A. MohdZin, "On the policy of photovoltaic and diesel generation mix for an off-grid site: East Malaysian perspectives". Solar Energy, Vol. 74 (2003), 453–467.
[24] H. Kazem, T. Khatib, K. Sopian, "Sizing of a standalone photovoltaic/battery system at minimum cost for remote housing electrification in Sohar, Oman". Energy and Buildings, Vol. 61 (2013), 108–115.
[25] W. Kellogg, M. Nehrir, G. Venkataramanan, V. Gerez, "Generation unit sizing and cost analysis for stand-alone wind, photovoltaic and hybrid wind/PV systems". IEEE Transactions on Energy Conversion, Vol. 13 (1998), 70 - 75.
[26] L. Goel, G. Shrestha, "A study on optimal sizing of stand-alone photovoltaic stations". IEEE Transactions on Energy Conversion, Vol. 13 (1998) No. 4, 373-378.
[27] A. Mellit, "Sizing of photovoltaic systems: a review". Revue des Energies Renouvelables, Vol. 10 (2007), 463–472.
[28] A. QayoomJakhrani, A. Othman, A. Rigit, S. Samo, S. Kamboh, "A novel analytical model for optimal sizing of standalone photovoltaic systems". Energy, Vol. 46 (2012), 675-682.
[29] E. Braunstein, A. Ofry, "The loss of power supply probability as a technique for designing stand-alone solar electrical (photovoltaic) systems". IEEE Transactions on Power Apparatus and Systems, Vol. 102 (1983) No. 5, 1171–1175.
[30] B. Salameh, Z. Borowy, "Methodology for optimally sizing the combination of a battery bank and PV array in a wind/PV hybrid system". IEEE Transactions on Energy Conversion, Vol. 11 (1996) No. 2, 367–375.
[31] C. Nogueira, M. Vidotto, R. Niedzialkoski, S.d. Souza, L. Chaves, T. Edwiges, D.d. Santos, I. Werncke, "Sizing and simulation of a photovoltaic-wind energy system using batteries, applied for a small rural property located in the south of Brazil". Renewable and Sustainable Energy Reviews, Vol. 29 (2014), 151-157.
[32] S. Diaf, G. Notton, M. Belhamel, M. Haddadi, A. Louche, "Design and techno-economical optimization for hybrid PV/wind system under various meteorological conditions". Aplied Energy, Vol. 85 (2008) No. 10, 968–987.
[33] H. Yang, J. Burnett, L. Lu, "Weather data and probability analysis of hybrid photovoltaic–wind power generation systems in Hong Kong". Renewable Energy, Vol. 28 (2003) No. 11, 1813–1824.
[34] M. Adaramola, "Viability of grid-connected solar PV energy system in Jos, Nigeria". Electrical Power and Energy Systems, Vol. 61 (2014), 64–69.
[35] G. Pillai, G. Putrus, T. Georgitsioti, N. Pearsall, "Near-term economic benefits from grid-connected residential PV (photovoltaic) systems". Energy, Vol. 68 (2014), 832-843.
[36] C. Boonmee, B. Plangklang, N. Watjanatepin, "System performance of a three-phase PV-grid-connected system installed in Thailand: Data monitored analysis". Renewable Energy, Vol. 34 (2009) No. 2, 384-389.
[37] G. Notton, V. Lazarov, L. Stoyanov, "Optimal sizing of a grid-connected PV system for various PV module technologies and inclinations, inverter efficiency characteristics and locations". Renewable Energy, Vol. 35 (2010) No. 2, 541-554.
[38] M. Mondal, A. Islam, "Potential and viability of grid-connected solar PV system in Bangladesh". Renewable Energy, Vol. 36 (2011), 1869–1874.
[39] H. Yang, W. Zhou, C. Lou, "Optimal design and techno-economic analysis of a hybrid solar–wind power generation system". Applied Energy, Vol. 86 (2009), 163–169.
[40] W. Zhou, H. Yang, Z. Fang, "Battery behavior prediction and battery working states analysis of a hybrid solar–wind power generation system". Renewable Energy, Vol. 33 (2008) No. 6, 1413–1423.
[41] S. Diafa, M. Belhamelb, M. Haddadic, A. Louchea, "Technical and economic assessment of hybrid photovoltaic/wind system with battery storage in Corsica Island". Energy Policy, Vol. 36 (2008) No. 2, 743–754.
[42] A. Celik, "Techno-economic analysis of autonomous PV–wind hybrid energy systems using different sizing methods". Energy Conversion and Management, Vol. 44 (2003) No. 12, 1951–1968.
[43] G. Tsagas, N. Bakos, "Technoeconomic assessment of a hybrid solar/wind installation for electrical energy saving". Energy Building, Vol. 35 (2003) No. 2, 139–145.
[44] T. Khatib, A. Mohamed, K. Sopian, "A review of photovoltaic systems size optimization techniques". Renewable and Sustainable Energy Reviews, Vol. 22 (2013), 454–465.
[45] Philadelphia-Company. Amman – Jordan; 2014.
[46] M. Benghanem, "Optimization of tilt angle for solar panel: case study for Madinah, Saudi Arabia". Applied Energy, Vol. 88 (2011), 1427 - 1433.
[47] P. Koronakis, "On the choice of the angle of tilt for south facing solar collectors in the Athens basin area". Solar Energy, Vol. 36 (1986), 217 - 225.
[48] B. Saiful, "Optimum slope angle and orientation of solar collectors for different periods of possible utilization". Energy Conversion and Management, Vol. 41 (2000), 855–860.
[49] A. Malik, A. Mohd, "Optimum tilt angle and orientation for solar collector in Brunei, Darussalam". Renewable Energy, Vol. 24 (2001), 223–234.
[50] B. Saiful, "Optimum orientation of domestic solar water heaters for the low latitude countries". Energy Conversion and Management, Vol. 42 (2001), 1205–1214.
[51] S. Adnan, M. Al-Akhras, I. Al-Omari, "Optimizing the tilt angle of solar collectors". Renewable Energy, Vol. 26 (2002), 587–598.
[52] B. Ai, H.Q. Ban, B. Ji, X. Liao, "Calculation of the hourly and daily radiation incident on three step tracking planes". Energy Conversion and Management, Vol. 44 (2003), 1999–2011.
[53] M. Kacira, M. Simsek, Y. Babur, S. Demirkol, "Determining optimum tilt angles and orientations of photovoltaic panels in Sanliurfa, Turkey". Renewable Energy, Vol. 29 (2004), 1265–1275.

[54] H. Hussein, G. Ahmad, H. El-Ghetany, "Performance evaluation of photovoltaic modules at different tilt angles and orientations". Energy Conversion and Management, Vol. 45 (2004), 2441–2452.

[55] H. Elminir, A. Ghitas, F. El-Hussainy, R. Hamid, M. Beheary, K. Abdel-Moneim, "Optimum solar flat-plate collector slope: case study for Helwan, Egypt". Energy Conversion and Management, Vol. 47 (2006), 624–637.

[56] K. Skeiker, "Optimum tilt angle and orientation for solar collectors in Syria". Energy Conversion and Management, Vol. 50 (2009), 2439–2448.

[57] Hay, "Calculation of monthly mean solar radiation for horizontal and tilted surfaces". Solar Energy, Vol. 23 (1979).

[58] Beckman J., Duffie W. Solar Engineering of Thermal Processes, 4th ed. New Jersey: John Wiley and Sons, Inc.; 2013.

[59] B. Jordan, R. Liu, "Daily insolation on surfaces tilted towards the equator". Transactions of the American Society of Heating Refrigeration and Air Conditioning Engineers, Vol. 67 (1962), 526–541.

[60] CBJ, Central Bank of Jordan; 2014.

[61] EDCO, Electricity distribution company; 2013.

[62] Arora J. Introduction to Optimum Design, 3rd edition, USA: Academic Press; 2011.

[63] EIA, Energy Information Administration, http://www.eia.doe.gov,

JJMIE

Volume 10 Number 1, March.2016
ISSN 1995-6665
Pages 51- 65

Jordan Journal of Mechanical and Industrial Engineering

Simulation of Optimal Exergy Efficiency of Solar Flat Plate Collector

Subhra Das *

Renewable Energy Department, Amity University Haryana, Gurgaon, India

Received 12 Sep 2014 *Accepted 25 Sep 2015*

Abstract

Exergy analysis identifies potential factors responsible for thermodynamic losses and leads to efficiency improvements. In the present paper, exergy efficiency is expressed as a function of dimensionless mass flow rate and outlet fluid temperature. A computer program was developed for determining the optimal performance parameters for maximum exergy efficiency in a flat plate collector. The study was conducted for six collectors of different areas, having a different overall loss coefficient and a heat removal factor. It is observed that for given values of incident solar radiation, inlet fluid temperature and ambient temperature, the optimal mass flow rate varied from 0.0019 -0.0022 kg/s and exergy efficiency varied from 5.2- 8.2% for the collectors depending on its gross area, overall heat loss coefficient and heat removal factor.

Keywords: *Optimization, Exergy Efficiency, Outlet Fluid Temperature, Mass Flow Rate, Flat Plate Collector*.

Nomenclature

A_c	Gross area of the collector, m^2.
A_p	Absorber plate area, m^2
c_p	Specific heat of the heat transfer fluid, J/ kg°C.
F_R	Heat removal factor of the collector, dimensionless.
F'	Collector efficiency factor, dimensionless.
H_a	Absorbed solar radiation per unit area of the collector, W/m^2.
H_t	Incident solar radiation per unit area, W/m^2.
$\dot{m}$	Mass flow rate, kg/s.
M	Mass flow number, dimensionless.
T_a	Ambient temperature, ºC.
$T_{f, in}$	Inlet fluid temperature, ºC
$T_{f, out}$	Outlet fluid temperature, ºC
T_p	Absorber plate temperature, ºC
$T_{p,max}$	Stagnation temperature, ºC
T_s	Apparent temperature of Sun, ºC
U_L	Overall heat loss coefficient, W/m^2ºC.

Greek Symbols

α	Absorptance of the absorber plate, dimensionless.
τ	Transmittance of the cover, dimensionless.
θ_{in}	Dimensionless inlet fluid temperature.
$\theta_{\max}$	Maximum collector temperature, dimensionless
θ_{out}	Dimensionless outlet fluid temperature.
θ^*_{out}	Dimensionless optimal outlet fluid temperature.
θ_s	Dimensionless apparent temperature of Sun.
η_I	Energy efficiency of collector, dimensionless.
η_{II}	Exergy efficiency of collector, dimensionless.

1. Introduction

Solar flat plate collectors are devices used for low temperature applications. The heat absorbed by absorber is partly transferred from absorber plate to the fluid flowing in the tubes and the rest is lost to ambient. Heat transfer irreversibility decreases with the increase in fluid flow rate but this increases losses due to fluid friction. To optimize heat transfer to fluid form the absorber plate, an optimal mass flow rate of the fluid needs to be determined which takes care of both heat transfer irreversibility and losses due to fluid friction.

In recent past, various methods have been applied to optimize the design of a collector. Analysis of a solar collector was conducted by Howell and Bannerot [1] in order to determine the optimum outlet temperature for a given solar collector that would maximize the work output for various idealized heat engine cycles. The analysis demonstrated the effect of the radiative and convective heat losses from the collector. Second law analysis for the optimization of flat plate solar air heaters was performed

* Corresponding author e-mail: nips.subhra@gmail.com.

by Altfeld *et al.* [2] where net exergy flow was maximized by minimizing exergy losses by absorption of radiation at absorber temperature level. Based on this analysis, optimal designs of the absorbers and flow ducts were determined. Having developed the optimal designs for air heaters, Altfeld *et al.* [3] conducted a sensitivity analysis to study the influence of varying operational conditions on optimal results. Hepbasli [4] comprehensively reviewed and evaluated the performance of a wide range of renewable energy resources and had defined exergy efficiency of solar flat plate collector. Luminosu *et al*. [5] conducted an exergy analysis of a flat plate collector with the assumption that the global solar radiation is equal to solar flux and inlet fluid temperature is equal to ambient temperature. Optimal operation mode of flat plate collector was determined by maximizing exergy efficiency of the collector with respect to various parameters. The global optimal operation mode of a flat plate collector was calculated considering exergy efficiency as a function of mass flow rate and collector area.

Exergy analysis was applied by various authors [6, 7, 8, 9] to judge a system and showed how exergy analysis provided illuminating and meaningful assessment of solar thermal processes and can assist in improving and optimizing designs. Kalogirou *et al.* [10] presented a review of exergy analysis of solar thermal systems. It includes exergy analysis of solar collectors like flat plate collectors, hybrid PV/T systems, parabolic trough collectors, parabolic dish collectors and reported various applications of solar thermal systems.

Though exergy analysis provides valuable information about the system but it is very complex to apply. Thus, the second law analyses which are simplified forms of exergy analysis are often employed. The Entropy Generation Minimization (EGM) technique was widely studied by Bejan [11] to optimize system performance in various heat transfer processes including solar thermal applications. In the past, many authors used the EGM method to judge and optimize processes [12, 13, 14]. Torres-Reyes *et al.* [15] established a procedure for the determination of optimal performance parameters for minimum entropy generation during the collection of solar energy. Doos *et al.* [16] presented Fuzzy ARTMAP neural network model to improve the process real-time performance of a power station in Al-Daura Refinery for the multi-agent process as a classifying system. Agent based fuzzy method has been employed by various authors in decision making problems to obtain the optimal solution [17, 18, 19, 20]. A numerical simulation was employed for the performance analysis of Stirling engine cycle by Tarawneh *et al*. [21].

F. Jafarkazemi *et al.* [22] conducted an energetic and exergetic evaluation of flat plate collector. The theoretical model was verified experimentally wherein flat plate collectors were tested in open loop with water as heat transfer fluid. The energy and exergy efficiency of flat plate collector were determined for constant mass flow rates of 0.03, 0.04 and 0.05 kg/s. The theoretical and experimental values were compared by computing the root mean square error. The effect of design parameters on the collector performance was also studied. Khademi *et al.* [23] studied the optimal exergy efficiency of flat plate collector by employing Sequential Quadratic Programming (SQP) and Genetic Algorithm (GA). Nonlinear constraint optimization technique was adopted in the present paper wherein objective function $(1-\eta_{II})$ is minimized w.r.t two inequality constraints viz. $\left[1 \le A_p \le 5 \text{ and } 0.001 \le \dot{m} \le 0.1\right]$. Khademi *et al*. [23] suggested that the rate of convergence of SQP [24] was much higher than that of GA, but GA provides results with a higher accuracy for exergy efficiency. They also suggested that the smaller collector could also have a similar and a better performance compared to the collector with a larger surface area. SQP algorithm has a high convergence rate. But the rate of convergence of SQP depends highly on the starting point, first and second order derivatives of the objective function and also it stops in local optimum points. These are the weaknesses of SQP. GA, on the other hand, requires an initial population for training and rate of convergence is also low. Mukhopadhyay *et al.* [25] optimized exergy efficiency of flat plate collector to obtain the optimal operational mode, i.e., mass flow rate and outlet fluid temperature for a given collector whereas Khademi *et al.* [23] optimized exergy efficiency to determine the optimal design parameters, i.e., area of collector and mass flow rate.

In the present paper, an analytical study [25] is conducted for six different collectors with different surface area A_c, heat removal factor F_R and overall heat loss coefficient U_L to determine the optimal mode of operation for which exergy and energy efficiency would be maximum for the fixed values of uncontrollable parameters such as solar radiation and ambient temperature. The present paper is an extension of our work [25], to present the simulation done to obtain the optimal operational mode of a flat plate collector. A computer program is written based on the proposed mathematical model to solve the nonlinear constrained optimization problem using Direct Substitution Method (DSM) to obtain the optimal results. DSM to solve nonlinear optimization problem is simple to implement compared to SQP and GA. The simulator thus developed requires initial input-specification data of collector ($F'U_L$, $F'\tau\alpha$, A_c, F_rU_L, $F_R\tau\alpha$, $\tau\alpha$), values of uncontrollable parameters (H_t, T_a, T_s) and heat capacity of heat transfer fluid, c_p to compute the optimal solution. The simulator is capable of determining the initial starting solution and thereby minimizes human error in its prediction. The optimal solution is obtained in less than 20 iterations. The development of the computer program based on the proposed optimization technique eliminates the dependency of author to use software which has its own limitations and complexities.

2. Optimization of Exergy Efficiency

Exergy efficiency of any process, as defined by Öztürk [6], is the ratio of the exergy transfer rate associated with the output to the exergy transfer rate associated with the driving input. Instantaneous exergy efficiency of flat plate collector can be defined as the ratio of the increased fluid exergy to the exergy of solar radiation.

The exergy transfer rate associated with output (fluid) at a given time is given by:

Exergy output associated with the fluid = Energy output – $T_a\times$ (Entropy generation in fluid)

$$\therefore Exergy_{output} =$$

$$\dot{m}c_p\left[(T_{f,out}-T_{f,in})-T_a\ln\frac{T_{f,out}}{T_{f,in}}\right] \quad (1)$$

Exergy transfer rate associated with solar radiation at a given time [7] is:

$$Exergy_{input} =$$

$$A_cH_t\left[1+\frac{1}{3}\left(\frac{T_a}{T_s}\right)^4-\frac{4}{3}\left(\frac{T_a}{T_s}\right)\right] \quad (2)$$

The instantaneous exergy efficiency of the collector is given by:

$$\eta_{II}=\frac{Exergy_{output}}{Exergy_{input}}=$$

$$\frac{\dot{m}c_p\left[(T_{f,out}-T_{f,in})-T_a\ln\frac{T_{f,out}}{T_{f,in}}\right]}{A_cH_t\left[1+\frac{1}{3}\left(\frac{T_a}{T_s}\right)^4-\frac{4}{3}\left(\frac{T_a}{T_s}\right)\right]} \quad (3)$$

Exergy efficiency given in Eq. (3) is expressed in dimensionless form as:

$$\eta_{II}=\frac{M}{\eta_e}\left[(\theta_{out}-\theta_{in})-\ln\left(\frac{\theta_{out}}{\theta_{in}}\right)\right] \quad (4)$$

where mass flow number

$$M=\frac{\dot{m}c_pT_a}{A_cH_t};$$

exergy fraction of solar radiation,

$$\eta_e=\left[1+\frac{1}{3}\left(\frac{T_a}{T_s}\right)^4-\frac{4}{3}\left(\frac{T_a}{T_s}\right)\right] \quad (5)$$

Dimensionless outlet and inlet fluid temperature respectively are,

$$\theta_{out}=\frac{T_{f,out}}{T_a};\ \theta_{in}=\frac{T_{f,in}}{T_a} \quad (6)$$

It is evident from Eq. (4) that the exergy efficiency of a given collector is a function of mass flow number, *M* and dimensionless outlet fluid temperature θ_{out}, for given solar insolation and ambient temperature.

Outlet fluid temperature for a collector can be computed using the following relation [26]:

$$\frac{T_{f,out}-T_a-H_a/U_L}{T_{f,in}-T_a-H_a/U_L}=\exp\left(\frac{-A_cF'U_L}{\dot{m}c_p}\right) \quad (7)$$

In dimensionless form the outlet fluid temperature in a flat plate collector can be expressed as:

$$\theta_{out}=$$

$$\theta_{\max}+(\theta_{in}-\theta_{\max})\exp\left(\frac{-F'(\tau\alpha)}{M(\theta_{\max}-1)}\right) \quad (8)$$

where $\theta_{\max}$ is the maximum collector temperature in dimensionless form. The maximum temperature of the plate ($T_{p,max}$) called the 'stagnation temperature', occurs when the entire solar heat transfer is lost to the ambient. That is, when the useful energy gains by the collector is zero. The maximum collector temperature is given in dimensionless form as [10]:

$$\theta_{\max}=\frac{T_{p,\max}}{T_a}=1+\frac{H_t}{U_LT_a} \quad (9)$$

Eliminating θ_{out} from Eq. (4) using Eq. (8) and differentiating η_{II} with respect to mass flow number M assuming θ_{in} and η_e constant and equating to zero we obtain:

$$\ln\left[\theta_{\max}+(1-\theta_{\max})\exp\left(-\tau\alpha F'/(\theta_{\max}-1)M\right)\right]+\frac{\left(-\tau\alpha F'/(\theta_{\max}-1)\right)(1-\theta_{\max})\exp\left(-\tau\alpha F'/(\theta_{\max}-1)M\right)}{M\left[\theta_{\max}+(1-\theta_{\max})\exp\left(-\tau\alpha F'/(\theta_{\max}-1)M\right)\right]}+$$

$$-(\theta_{\max}-1)\left[1-\exp\left(-\tau\alpha F'/(\theta_{\max}-1)M\right)\left(1+\left(-\tau\alpha F'/(\theta_{\max}-1)M\right)\right)\right]=0 \quad (10)$$

For the computer program, the left hand side of Eq. (10) is denoted by dEffdM. Eq. (10) is solved using Bisection Method to find the optimal mass flow number *M** for which exergy efficiency is maximum for a given collector. Substituting *M** in Eq. (8) gives the optimal outlet fluid temperature θ^*_{out}. The optimal exergy efficiency η^*_{II} is obtained by substituting *M** and θ^*_{out} in Eq. (4).

3. Optimization Process

The mathematical model for optimizing exergy efficiency is based on the following nonlinear constrained optimization problem:

$$\text{Maximize } \eta_{II} = \frac{M}{\eta_e}\left[(\theta_{out} - \theta_{in}) - \ln\left(\frac{\theta_{out}}{\theta_{in}}\right)\right] \quad \text{eq.(4)}$$

subject to the constraints

$$M = \frac{\dot{m} c_p T_a}{A_c H_t} \quad \text{eq.(5)}$$

$$\theta_{out} = \theta_{\max} + (\theta_{in} - \theta_{\max}) \exp\left(\frac{-F'(\tau\alpha)}{M(\theta_{\max} - 1)}\right) \quad \text{eq.(8)}$$

$M \geq 0,\ \theta_{out} \geq 0$

The Direct Substitution Method was applied to solve the optimization problem as discussed in Section 2. The optimization process is described in the following schematic diagram, Figure 1.

Variation of the exergy efficiency was studied as a function of mass flow rate with the following assumptions:

- For a given collector assume that the parameters like area of the collector A_c; heat removal factor, F_R; collector efficiency factor F' and overall heat loss coefficient, U_L; transmissivity of cover (τ) and absorptance of plate (α) are constant.
- Inlet fluid temperature is assumed to be equal to ambient temperature, i.e., $\theta_{in} = T_{f,in}/T_a = 1$; incident solar radiation on the collector, $H_t = 800\ W/m^2$; ambient temperature, $T_a = 30^oC$ and apparent sun temperature, $T_s = 6000\ K$.
- Mass flow rate is varied from 0.0001 to 0.0419 kg/s and the corresponding exergy efficiency and energy efficiency are calculated for a given collector.

The flow chart for the optimization process to compute optimal mass flow rate and outlet fluid temperature, which maximizes exergy efficiency of the collector, is shown in Figures 2-4. Figure 2 represents the process for computing energy and exergy efficiency for different values of mass flow rate. Flow chart for computing two initial values of mass flow rate such that dEffdM takes a positive value for one and a negative value for the other, shown in Figure 3. These two values are the initial input for starting bisection method to obtain the optimal mass flow rate. Figure 4 shows the flow chart for computing the optimal mass flow rate that optimizes exergy efficiency.

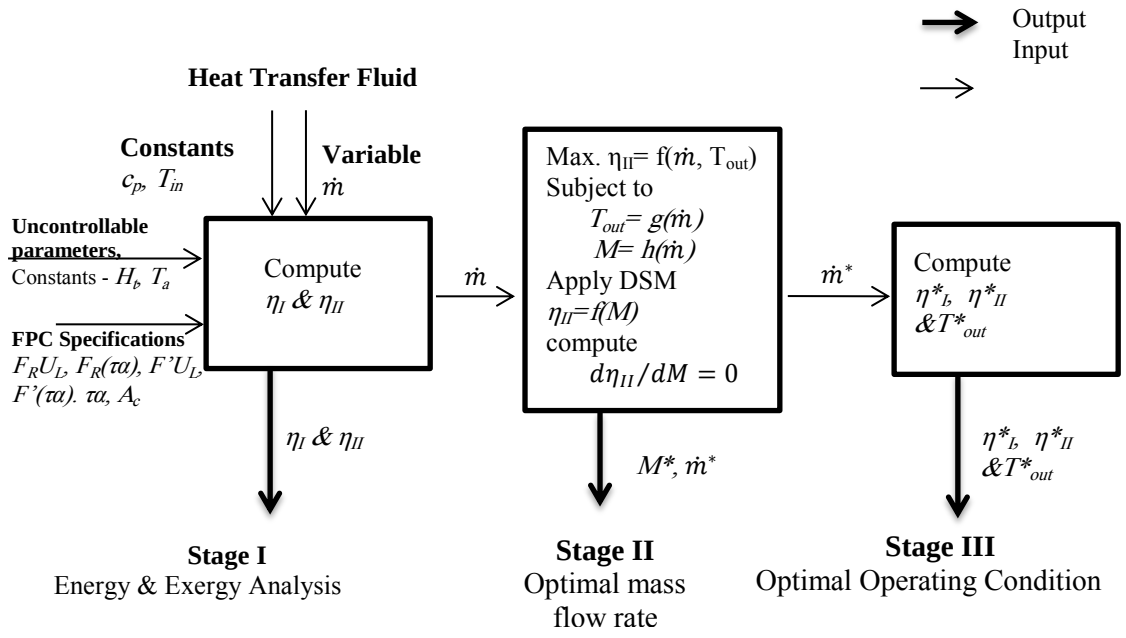

Figure 1. Schematic Diagram of Optimization Process

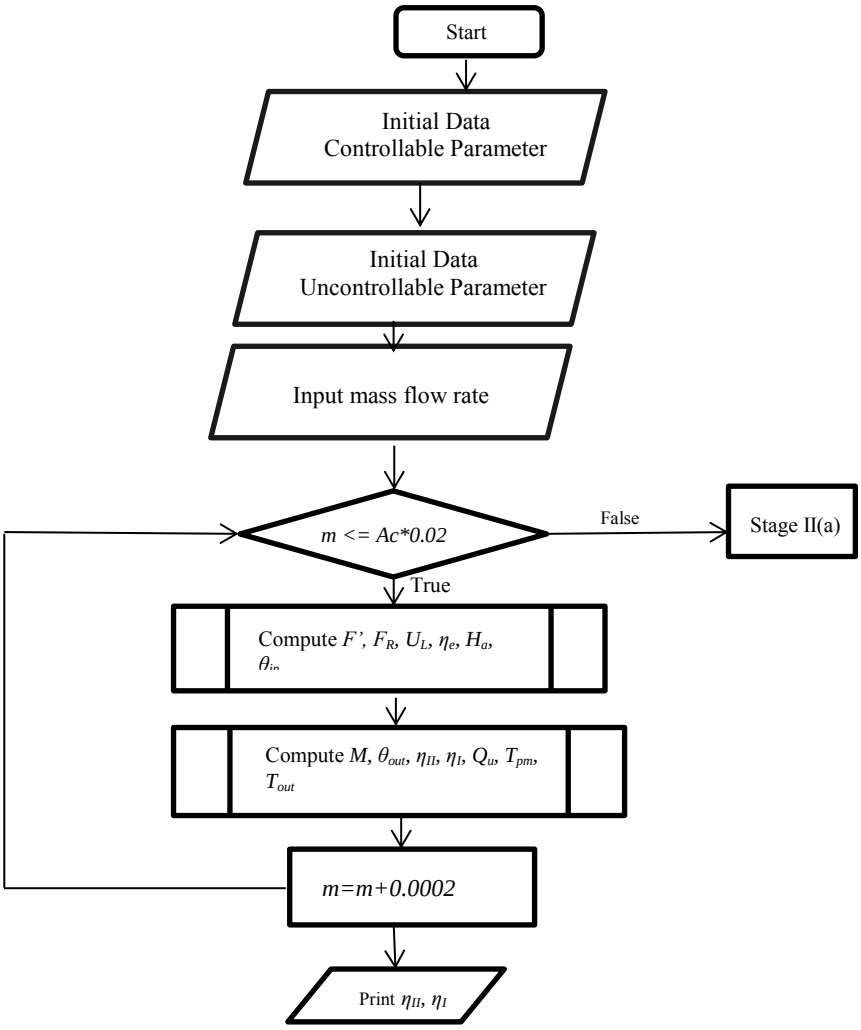

Figure 2. Flow Chart for Energy & Exergy Analysis

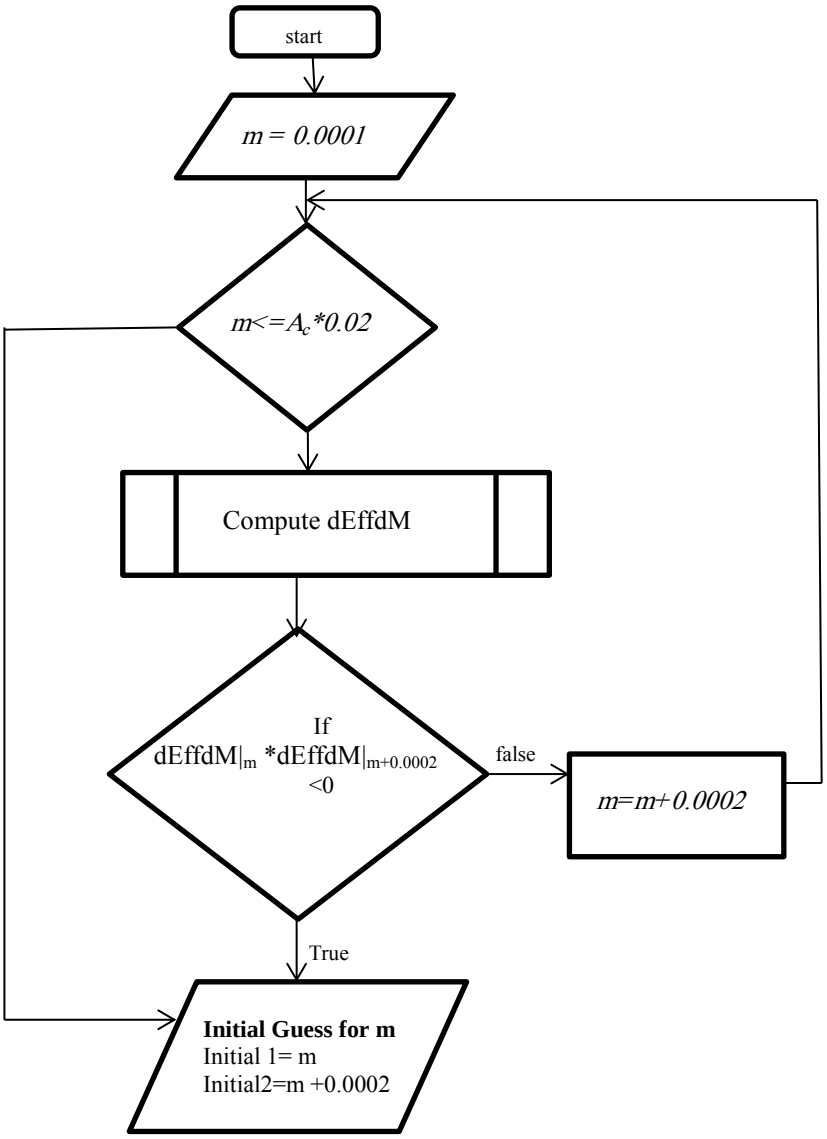

Figure 3: Stage II (a)- Flow chart for computing initial values of mass flow rate to start Bisection method

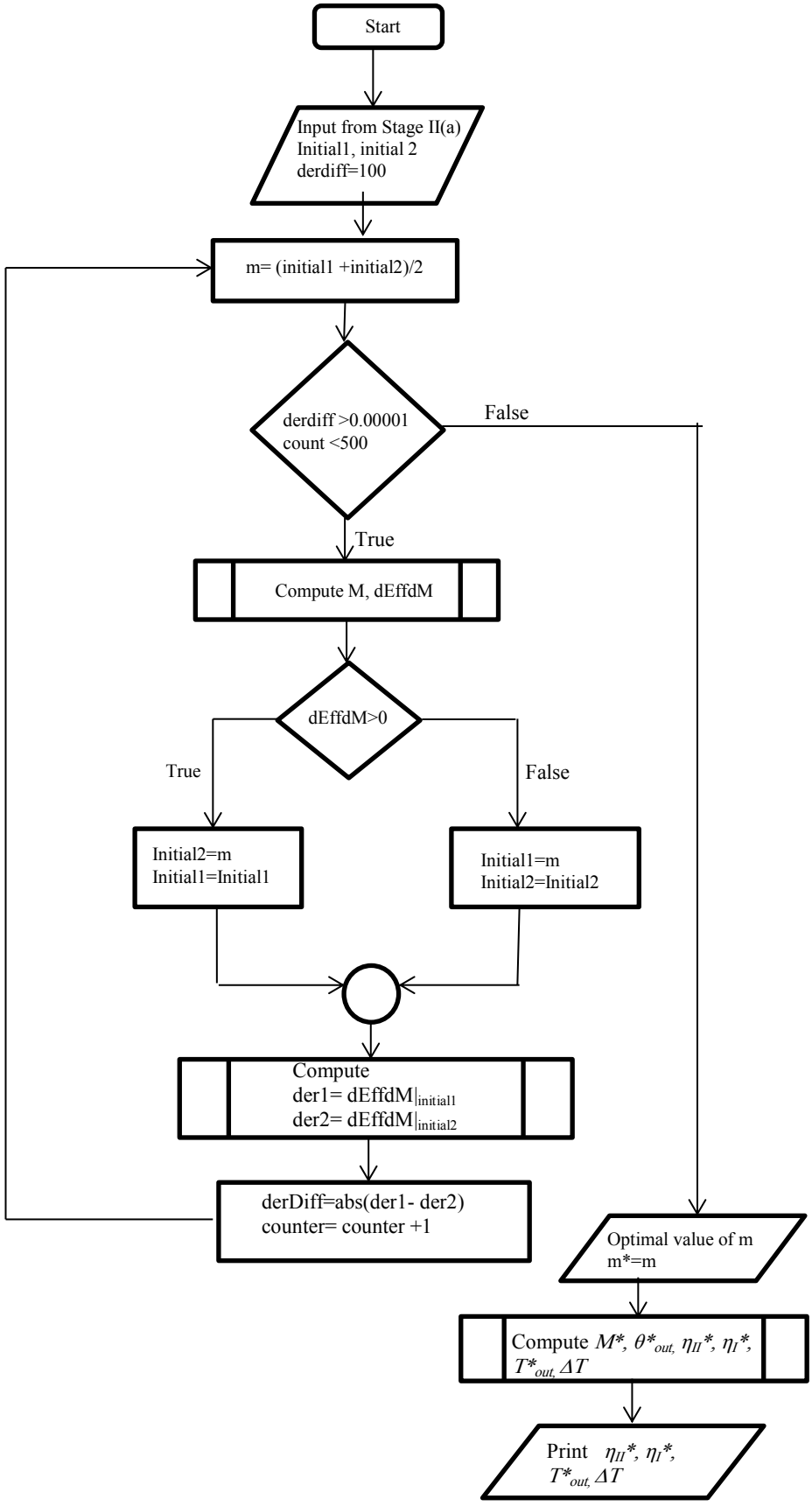

Figure 4. Flow chart for computing optimal mass flow rate and corresponding optimal energy and exergy efficiency, optimal outlet temperature

4. Results and Discussion

A computer program in C language was developed based on the method discussed in Section 3 for computing the optimal mass flow rate that maximizes exergy efficiency of a flat plate collector. Figures 5 and 6, respectively, show the variation of energy and exergy efficiency of a flat plate collector with respect to mass flow rate. From Figure 5, it is observed that energy efficiency increases exponentially with the increase in mass flow rate then saturation begins, the growth slows and finally the growth stops and the energy efficiency remains unchanged with the increase in mass flow rate. Energy efficiency growth curve resembles the logistic curve in 1st quadrant. A similar pattern of the growth of energy efficiency with respect to mass flow rate is reported by Jafarkazemi [22].

Exergy efficiency increases rapidly with the increase in mass flow rate; it attains a maximum value and then decreases with the further increase in mass flow rate.

The optimal operating conditions, i.e., optimal mass flow rate $\dot{m}^*$ and the corresponding optimal outlet fluid temperature, the exergy efficiency and ΔT are determined for a given flat plate collector. The optimal operating conditions for six different collectors with a different collector area, a heat removal factor and an overall heat loss coefficient are computed assuming $H_t = 800\ W/m^2$ and $T_a = 30\ ^oC = T_{f,in}$ and are tabulated in Table 1.

It is observed that for a given value of incident solar radiation, inlet fluid temperature and ambient temperature, optimal mass flow rate varied from 0.0019 -0.0022 kg/s and exergy efficiency varied from 5.2 - 8.2% for the collectors depending on its gross area A_c, overall heat loss coefficient U_L and heat removal factor F_R.

Luminosu *et al.* [5] also determined the optimal operational mode of flat plate collector by exergetic analysis. They assumed that the exergy flow rate in global solar radiation is equal to the solar flux (*HR*) and defined exergy efficiency for flat plate collector as:

$$\eta_{II,Luminosu} = \dot{m}c_p\left[\frac{\Delta T - T_a \ln\left(\frac{T_{f,out}}{T_{f,in}}\right)}{A_c(HR)}\right] \quad (11)$$

The global maximum points suggested by Luminosu *et al.* [5] are: $A_c = 3.3\ m^2$, mass flow rate = 0.0031 kg/s, $\eta_{II} = 3.9\%$ and $\Delta T = 63.3\ K$. The optimal operating conditions for collector with area $A_c = 3.12\ m^2$ as obtained by author in this work are optimal mass flow rate = 0.0027 kg/s, exergy efficiency = 8.9%. For the same collector, Khademi *et al.* [23] obtained optimal mass flow rate = 0.0022 kg/s, exergy efficiency = 7.002%. The optimal mass flow rates obtained in all the three works above are almost equal. A significant difference in optimal values of exergy efficiency is noted in the work of Luminosu *et al.* which maybe because of the simplifying assumption for sun's exergy flow rate made by them.

Khademi *et al.* [23] applied SQP and Genetic Algorithm to obtain optimal design criteria for maximizing exergy efficiency. Optimal result obtained by Khademi *et al.* [22] applying SQP is:

$$\dot{m} = 0.004365\frac{kg}{s}, A_p = 5m^2, \eta_{II} = 6.1728\%, T_{f,out} = 388.997\ K, \eta_I = 46.4519\%.$$

The optimal results obtained by employing GA over a population of 500 and 150 generation are:

$$\dot{m} = 0.002178\frac{kg}{s}, A_p = 3.12\ m^2, \eta_{II} = 7.0002\%, T_{f,out} = 407.684\ K, \eta_I = 44.9486\%.$$

Table 1. Optimal mass flow rate for different flat plate collectors and the corresponding optimal exergy efficiency, optimal outlet fluid temperature and $\Delta T = T^*_{f,out} - T_{f,in}$ are tabulated where $H_t = 800\ W/m^2$, $T_a = 303\ K = T_{f,in}$ and c_p of water is considered at the inlet fluid temperature.

Collector	A_c	F_R	U_L	$\dot{m}^*$	η_{II}^*	$T^*_{f,out}$	ΔT
	m^2		W/m^{2}K	kg/s	%	K	K
A	2.13	0.805	5.78	0.0023	5.2	380.01	77.01
B	2.26	0.76	3.68	0.0016	7.0	419.98	116.98
C	2.23	0.76	3.08	0.0019	8.2	419.99	116.99
D	1.55	0.78	3.56	0.0013	7.5	419.98	116.98
E	1.99	0.76	4.45	0.0017	6.1	405.01	102.01
F	2.125	0.805	5.8	0.0022	5.2	380.01	77.01

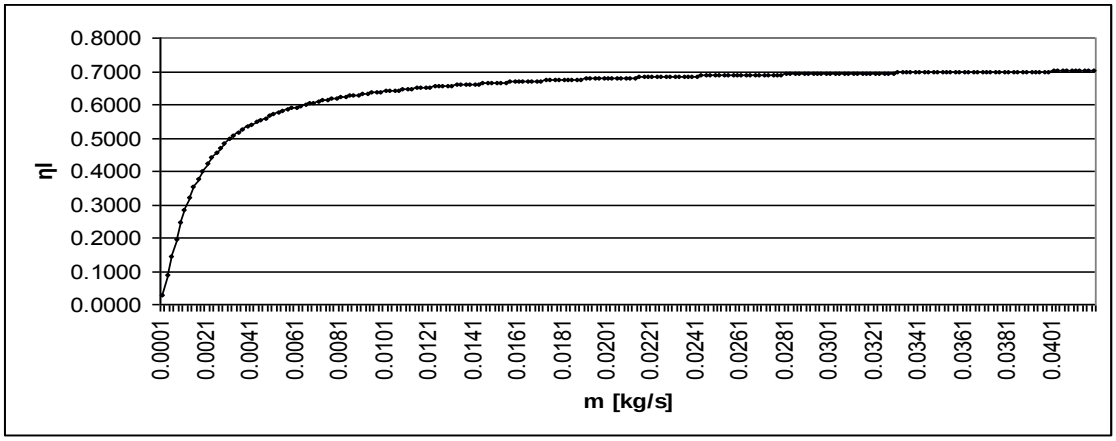

Figure 5. Variation of energy efficiency with respect to mass flow rate for a collector of area Ac = 2.13 m2, FR =0.805, UL =5.76 W/m2K, Ht = 800 W/m2 and Ta = 30 ºC.

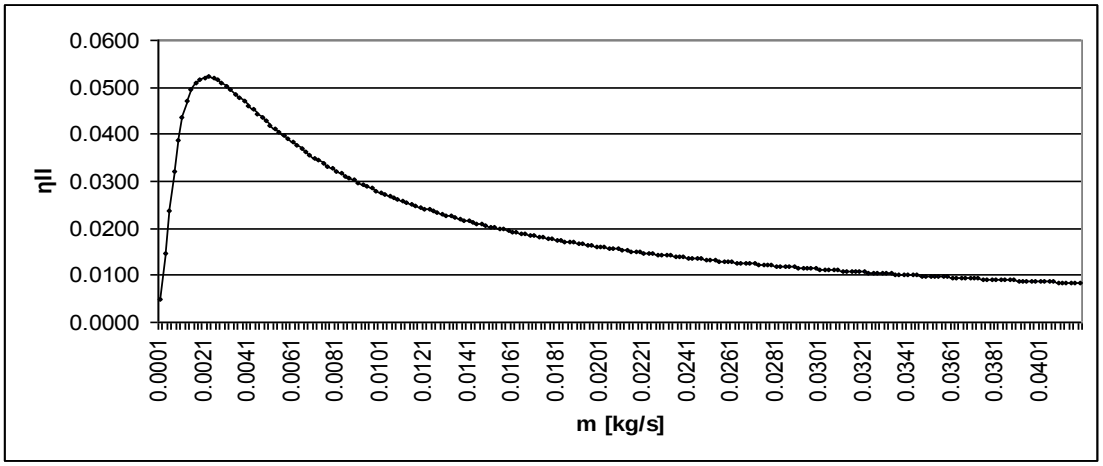

Figure 6. Variation of exergy efficiency with respect to mass flow rate for a collector of area A_c = 2.13 m^2, F_R =0.805, U_L =5.76 W/m^2K, H_t = 800 W/m^2 and T_a = 30 ºC = $T_{f,in}$.

5. Validation of Computer Code

To validate the computer code, optimal operation mode is determined for flat plate collector with design parameters considered by Khademi *et al*. [23] as input for the proposed model. The optimal results are compared with those reported by Khademi *et al.*. Tables 2 and 3 respectively presents a comparison of the optimal results obtained in the present work with those obtained by Khademi *et al.* using Genetic Algorithm and SQP. From Tables 2 and 3, it is evident that the error in computing the optimal exergy efficiency, optimal mass flow rate and optimal outlet temperature using the proposed method is small in both cases. One of the sources of error may be the input solar radiation which is considered to be 800W/m^2 in the present work and is taken to be constant. Khademi *et al*. [23] did not report explicitly the value of input solar radiation used for computing the optimal design conditions.

Table 2. Comparison of optimal results obtained by using proposed model with that obtained by Khademi [23] using Genetic Algorithm; Number of iteration is 15 for proposed model.

Input					*η*II*			*m**			*T*out*		
Ac	***Tin***	U_L	Q_u	η_I	**Applying GA**	**Present work**	**Error**	**Applying GA**	**Present work**	**Error**	**Applying GA**	**Present work**	**Error**
m^2	K	W/m^2K	W/m^2								K		
3.12	300	3.29	1493.8	44.9	7.002	8.9	1.898	0.002178	0.002675	4.97E-04	407.684	414.514	6.83

Table 3. Comparison of optimal results obtained by using proposed model with that obtained by Khademi [23] using SQP; Number of iteration is 17 for proposed model and 9 for SQP.

Input					*η*II*			*m**			*T*out*		
Ac	***Tin***	U_L	Q_u	η_I	**Applying SQP**	**Present work**	**Error**	**Applying SQP**	**Present work**	**Error**	**Applying SQP**	**Present work**	**Error**
m^2	K	W/m^2K	W/m^2								K		
5	300	3.7978	1621.9	46.45	6.1728	5.28	0.893	0.004365	0.003063	1.30E-03	388.997	406.638	17.64

6. Conclusions

Exergetic optimization of flat plate collectors is carried out to evaluate the performance of a flat plate collector depending on mass flow rate and outlet fluid temperature. It is observed that decreasing the flow rate below optimal value increases the temperature of the fluid but a decrease in the exergy efficiency occurs. On the other hand, increasing the flow rate above the optimal value increases the energy efficiency but a decrease in the exergy efficiency and fluid temperature occurs. Thus, it can be concluded that the exergy analysis of the solar flat plate collectors allows the pre-determination of the optimal operational conditions for a collector for given values of controlled or uncontrolled parameters.

The simulator developed based on the proposed mathematical model can be used to determine the optimal operational mode of a flat plate collector for given environmental conditions. The rate of convergence of the proposed method is high and the accuracy of the result is also high. The results obtained are comparable to those reported by Khademi *et al.* [23] with an error of 0.8 for computing optimal exergy efficiency, error of the order of 10^{-3} for computing the optimal mass flow rate and error of 17.64 for computing the optimal outlet fluid temperature when results were compared with those obtained by using SQP. When results were compared with results obtained by Genetic Algorithm, error in computing the optimal exergy is 1.9, error is of the order of 10^{-4} for computing the optimal mass flow rate and an error of 6.83 for computing the optimal outlet fluid temperature is observed. It is observed that the error in computing the optimal operational mode using the proposed model is less when compared to the optimal solution obtained by Genetic Algorithm than SQP. Khademi *et al.* [23] reported that the results of GA represent more accuracy of algorithm. Hence, the simulator developed to solve the nonlinear constraint optimization problem based on direct substitution method gives an optimal result with a considerably good accuracy.

References

[1] J. R. Howell, R. B. Bannerot, "Optimum solar collector operation for maximizing cycle work output". Solar Energy, 19 (1977), 149-153.

[2] K. Altfeld, W. Leiner, M. Fiebig, "Second law optimization of flat plate solar air heaters". Solar Energy, Vol. 41(1988) No. 2, 127-132.

[3] K. Altfeld, W. Leiner, M. Fiebig, "Second law optimization of flat plate solar air heaters. Part 2: Results of optimization and analysis of sensibility to variations of operating conditions". Solar Energy, Vol. 41 (1988) No. 4, 309-317.

[4] A. Hepbasli, "A key review on exergetic analysis and assessment of renewable energy resources for a sustainable future". Renewable and Sustainable Energy Reviews, Vol. 12 (2008), 593-661.

[5] I. Luminosu, L. Fara, "Determination of the optimal operation mode of a flat solar collector by exergetic analysis and numerical simulation". Energy, Vol. 30 (2005) issue 5, 731-747.

[6] H. H. Öztürk, "Experimental determination of energy and exergy efficiency of the solar parabolic-cooker". Solar Energy, Vol.77 (2004), 67-71.

[7] R. Petala,"Exergy analysis of the solar cylindrical-parabolic cooker". Solar Energy, Vol.79 (2005), 221-233.

[8] M. A. Rosen, "Second-Law of Analysis: Approach and Implication". International Journal of Energy Research, Vol. 23 (1999), 415-429.

[9] S. Farahat, F. Sarhaddi, H. Ajam, "Exergetic optimization of flat plate solar collectors". Renewable Energy, Vol 34 (2009) No.4, 1169-1174.

[10] S. A. Kalogirou, S. Karellas, V. Badescu, K. Braimakis, "Exergy analysis on solar thermal systems: A better understanding of their sustainability". Renewable Energy XXX (2015) 1-6, In press.

[11] A. Bejan. Entropy generation minimization. CRC press. Inc., 1996, p. 249- 259.

[12] D. K. Mahanta, S. K. Saha, "Internal irreversibility in a water heating solar flat plate collector". Energy Conversion and Management, Vol. 43 (2002), 2425-2435.

[13] S. K. Saha, D. K. Mahanta, "Thermodynamic optimization of solar-plate collector". Renewal Energy, Vol. 23 (2001), 181-193.

[14] S. K. Saha, K. K. Datta Gupta, "Thermodynamic optimization of solar thermal collectors". Proceedings of National Solar Energy Society of India, Integrated Renewable Energy for Rural Development, 1990.

[15] E. Torres-Reyes, J. G. Cervantes-De Gortari, B. A. Ibarra-Salazar, M. Picon-Nuñez, "A design method of flat plate solar collectors based on minimum entropy generation". Exergy International, Vol. 1 (2001) 46-52.

[16] Q. M. Doos, Z. Al-Daoud, S. M. Al-Thraa, "Agent Based Fuzzy ARTMAP Neural Network for Classifying the Power Plant Performance". Jordan Journal of Mechanical and Industrial Engineering, Vol. 2, (2008) No. 3, 123-129.

[17] Vivek Kumar, S. Srinivasan, S. Das, "Optimal Solution for Supplier Selection based on SMART Fuzzy Case Base Approach". 7th IEEE International Conference on Soft Computing and Intelligent Systems, flagship international conference of Soft Computing in Asia, Fukuoka, JAPAN, 2014.

[18] Vivek Kumar, S. Srinivasan, S. Das, "Multi-Agent based Decision Support System using Data Mining, Case Based Reasoning and Fuzzy in Supply Chain Management". International Conference on e-Commerce, e-Administration, e-Society, e-Education, and e-Technology – Fall Session (e-CASE & e-Tech 2014 – Fall Session), Tokyo, JAPAN. 2014.

[19] Vivek Kumar, S. Srinivasan, S. Das, "A Fuzzy Agent-based Architecture for Supplier Selection". Journal of Computing, Vol 3, (2011) Issue 5.

[20] Vivek Kumar, S. Srinivasan, S. Das, "A Multi-Agent System for Management of Supplier Selection Process in a Fuzzy Supply Chain". International Journal of Computer Application, Vol.23 (2011) No. 6, 31–37.

[21] M. Tarawneh, F. Al-Ghathianb, M. A. Nawaflehc, N.Al-Kloub, "Numerical Simulation and Performance Evaluation of Stirling Engine Cycle". Jordan Journal of Mechanical and Industrial Engineering, Vol. 4 (2010) No. 5, 615- 628.

[22] F. Jafarkazemi, E. Ahmadifard, "Energetic and exergetic evaluation of flat plate solar collectors". Renewable Energy, Vol. 56 (2013) 55-63.

[23] M. Khademi, F. Jafarkazemi, E. Ahmadifard, S. younesnejad, **"**Optimizing Exergy Efficiency of Flat Plate Solar Collectors Using SQP and Genetic Algorithm", Applied Mechanics and Materials, Vols. 253-255 (2013) 760-765.

[24] P. T Boggs, J. W. Tolle. "Sequential Quadratic Programming", Acta Numerica (1996) 1-000.

[25] S. Mukhopadhyay, B. Bandyopadhyay , S. K. Saha, "Thermodynamic Optimization of the Performance of a Flat Plate Collector". Proceedings of International Conference on Issues and Challenge in Energy Conversion and Management, BHU, India 2009

[26] J. A. Duffie, W. A. Beckman. Solar Engineering of Thermal Process. 2nd ed. New York : Wiley Interscience, 1991.

Appendix

Computer Code Developed for Exergetic Optimization of Flat Plate Collectors

```
//*************************************************************
File Name            : Efficiency.cpp
PURPOSE              : Optimization of Second Law Efficiency w.r.t. mass flow rate
*************************************************************/
// ********************* HEADER FILES ***************************
#include<stdio.h>
#include<iostream.h>
#include<fstream.h>
#include<math.h>
void main()
{
        // ********* DECLARATION AND INITIALIZATION *************
        double F_Ul =       4.86;                       // F'UL
        double F_TowAlpha = 0.722;          // F'(Tow)(Alpha)
        double Ac = 2.13;                   // Gross Area of the Collector
        double Ts = 6000;           // Aparent Temp of the Solar Radiation
        double FrUl = 4.66;                         // FRUL
        double FrTowAlpha = 0.688;          // FR(Tow)(Alpha)
        double TowAlpha = 0.855;            // (Tow)(Alpha)

        double Ht = 800;    // Solar Insolation on the Collector Plane (W/m*m)
        double Ta = 303;                            // Ambient Temp. (in Kelvin)
        double cp = 4179;           // Specific Heat Capacity of Water (J/kg-K)

        int i,j,counter;
        double tow,alpha,Fdash,Fr,Ul;
        double Tin,Tout,Ha,thetaIn, thetaMax,Qu;
        double etaE,M,md,eff2,dEffdM;
        double eta1,thetaOut,tpm,deltaT;
        double temp,mInitial1,mInitial2;
        double mdLower, mdUpper, mdMiddle, mdOptimum;
        double der1, der2, derDiff;
        ofstream result("Result.txt",ios::app);
        int slopSign1, slopSign2;
        double initial1 = -1000;
        double initial2 = -1000;
         int flagFound = 0;
         int flagStart = 1;

        // ********** CALCULATION  *****************
        Fdash = F_TowAlpha/TowAlpha;        // Fdash: Collector Efficiency Factor
        Fr =        FrTowAlpha/TowAlpha;    // Fr: Collector Heat removal factor
```

```
Ul =        FrUl/Fr;              // Ul: Overall Loss Coefficient (W/m*m-K)

Ha = TowAlpha*Ht;                 // Ha: Absorbed Solar Radiation (W/m*m)
Tin = Ta;                                 // Tin: Inlet Fluid Temp. (K)
thetaIn = Tin/Ta;                 // thetaIn: Dimensionless Inlet fluid temp.
thetaMax = 1 + Ha/(Ul*Ta);  // thetaMax: Dimensionless max plate temp.
etaE = 1 + pow((Ta/Ts),4)/3 - 4*(Ta/Ts)/3;
                                          // etaE: Exergy Fraction of Solar radiation
printf("Fdash:%f\n",Fdash);
printf("Fr:%f\n",Fr);
printf("Ul:%f\n",Ul);
printf("Ha:%f\n",Ha);
printf("Tin:%f\n",Tin);
printf("thetaIn:%f\n",thetaIn);
printf("thetaMax:%f\n",thetaMax);
printf("cp:%f\n",cp);
printf("Ta:%f\n",Ta);
printf("Ht:%f\n",Ht);
printf("Ac:%f\n",Ac);
printf("etaE:%f\n",etaE);

result<<"m-dot"<<"    "<<"M"<<"    "<<"Eff 2"<<"    "<<"Derivation"<<"    "<<"Eff 1"<<"
"<<"Tpm"<<"    "<<"Delta-T"<<endl;

// ***CALCULATION OF ENERGY EFFICIENCY AND EXERGY EFFICIENCY OF COLLECTOR &
INITIAL GUESS FOR BISECTION METHOD*********

//        md: Mass Flow rate (kg/s)
//        M: Mass Flow Number
//        eff2: Second Law Efficiency
//        dEffdM: Derivative of Second Law Efficiency w.r.t M
//        eta1: First Law Efficiency
//        tpm: Mean Plate temp.(K)
//        deltaT: Difference between Outlet and Inlet fluid temp (K)

mInitial1 = -1000;
mInitial2 = -1000;

for(md = 0.0001; md<= Ac*0.02 ; md=md+0.0002)
{
        M = md*cp*Ta/(Ac*Ht);

        eff2 =  (M*(thetaMax - 1)/etaE)*(1 - exp(-F_TowAlpha/(M*(thetaMax-1)))) -
                (M/etaE)*log(thetaMax + (1 - thetaMax)*exp(-F_TowAlpha/(M*(thetaMax-1))));
```

```
                // Output results for Eta1, Tpm
                thetaOut = thetaMax + (thetaIn - thetaMax)*exp(-F_TowAlpha/(M*(thetaMax-1)));
                eta1 = M*(thetaOut - thetaIn);

                Qu = Ac*Ht*eta1;
                tpm = Tin + (Qu*(1-Fr))/(Ac*FrUl);

                Tout = Ta*thetaOut;
                deltaT = Tout - Tin;

                // To Find the Initial Guess for Bisection Method
                temp =          F_TowAlpha/(thetaMax - 1);
                dEffdM =log(thetaMax + (1-thetaMax)*exp(-temp/M))
                                +(temp*(1-thetaMax)*exp(- temp/M))/(M*(thetaMax + (1-thetaMax)*exp(-
                temp/M)))
                                                -       (thetaMax-1)*(1-exp(-temp/M)*(1+(temp/M)));

                    if (flagStart==1)
{
  if (dEffdM>0)
  {
    slopSign1 = 1;
            }
  else
  {
    slopSign1 = -1;
            }
            initial1 = md;
            initial2 = md+ 0.0002;
            flagStart = 0;
          }
          else
          {
            if (flagFound == 0)
            {
              if (dEffdM>0)
              {
                slopSign2 = 1;
                        der1= dEffdM;
              }
              else
              {
                slopSign2 = -1;
                        der2= dEffdM;
              }
```

```
            if (slopSign1*slopSign2 < 0)
            {
               flagFound = 1;
            }
            else
            {
               initial1 = md;
               initial2 = md+ 0.02;
            }
          }
        }// End of Else

            printf("m:%f        M:%f      Eff:%f    Derivative:%f       Eta1:%f Tpm:%f
                    deltaT:%f\n",md,M,eff2,dEffdM,eta1,tpm,deltaT);
            result<<md<<"      "<<M<<""<<eff2<<"          "<<dEffdM<<"      "<<eta1<<"          "<<tpm<<"
"<<deltaT<<endl;

}// End of for (md)

printf("\nInitial 1: %f            Initial 2: %f\n",mInitial1,mInitial2);
//** CALCULATION OF OPTIMUM MASS FLOW RATE BY BISECTION METHOD **/
mdLower = mInitial1;
mdUpper = mInitial2;
mdMiddle = (mInitial1 + mInitial2)/2;

derDiff = 100;
counter = 0;
temp =              F_TowAlpha/(thetaMax - 1);
while(derDiff>0.000001 && counter < 500)
{
            M = mdMiddle*cp*Ta/(Ac*Ht);
                    dEffdM =log(thetaMax + (1-thetaMax)*exp(-temp/M))
                                        +       (temp*(1-thetaMax)*exp(-temp/M))/(M*(thetaMax + (1-
            thetaMax)*exp(-temp/M)))
                                        -       (thetaMax-1)*(1-exp(-temp/M)*(1+(temp/M)));

            if(dEffdM > 0)
                    mdUpper = mdMiddle;
            else mdLower = mdMiddle;
            M = mdLower*cp*Ta/(Ac*Ht);
            der1 =  log(thetaMax + (1-thetaMax)*exp(-temp/M))
                                        +       (temp*(1-thetaMax)*exp(-temp/M))/(M*(thetaMax + (1-
            thetaMax)*exp(-temp/M)))
                                        -       (thetaMax-1)*(1-exp(-temp/M)*(1+(temp/M)));
```

```
            M = mdUpper*cp*Ta/(Ac*Ht);
            der2 =    log(thetaMax + (1-thetaMax)*exp(-temp/M))
                                    +        (temp*(1-thetaMax)*exp(-temp/M))/(M*(thetaMax + (1-
            thetaMax)*exp(-temp/M)))
                                    -        (thetaMax-1)*(1-exp(-temp/M)*(1+(temp/M)));

            mdMiddle = (mdUpper + mdLower)/2;
            derDiff = fabs(der1 – der2);
            counter++;
        }// End of while()

        // **** CALCULATE THE OPTIMUM VALUES ***************
        mdOptimum = mdMiddle;
        M = mdOptimum*cp*Ta/(Ac*Ht);

        eff2 =    (M*(thetaMax - 1)/etaE)*(1 - exp(-F_TowAlpha/(M*(thetaMax-1)))) -        (M/etaE)*log(thetaMax
        + (1 - thetaMax)*exp(-F_TowAlpha/(M*(thetaMax-1))));

        // Output results for Eta1, Tpm

        thetaOut = thetaMax + (thetaIn - thetaMax)*exp(- F_TowAlpha/(M*(thetaMax-1)));
        eta1 = M*(thetaOut - thetaIn);

        Qu = Ac*Ht*eta1;
        tpm = Tin + (Qu*(1-Fr))/(Ac*FrUl);

        Tout = Ta*thetaOut;
        deltaT = Tout - Tin;

        printf("Optimum m:%f        Eff2:%f   Eta1:%f            Tpm:%f
        deltaT:%f\n",mdOptimum,eff2,eta1,tpm,deltaT);

        result<<endl;
        result<<"******  OPTIMUM VALUES ***********"<<endl;
        result<<"Optimum Mass Flow rate:"<<mdOptimum<<endl;
        result<<"2nd law Efficiency:"<<eff2<<endl;
        result<<"1st law Efficiency:"<<eta1<<endl;
        result<<"Tpm:"<<tpm<<endl;
        result<<"Delta T:"<<deltaT<<endl;
        result.close();
}// End of main()
```

JJMIE

Volume 10 Number 1, March.2016
ISSN 1995-6665
Pages 67- 74

Jordan Journal of Mechanical and Industrial Engineering

A Fuzzy Approach for Modeling and Design of Agile Supply Chains using Interpretive Structural Modeling

Balaji M [a *], Velmurugan V [b], Prapa M [c], Mythily V [c]

[a] Assistant professor (III), Department of Mechanical Engineering, Kumaraguru College of Technology, Coimbatore 641049, India
[b] Principal, Sree Sakthi Engineering College, Coimbatore 641104, India
[c] Department of Mechanical Engineering,Kumaraguru College of Technology, Coimbatore 641049, India

Received 9 Feb 2015 Accepted 16 Oct 2015

Abstract

Supply chain agility has opened new perspectives for efficient and intelligent manufacturing. In the arena of intense global competition, analysis of supply chain enablers and their interactions between one another decide the levels of agility. Previous research studies have effectively used Interpretive Structural Modeling (ISM) to study the relationships between identified enablers with the aid of Structural Self Interaction Matrix (SSIM), Reachability Matrix (RM) & Graph Theoretic Approach (GTA). In the present paper, fuzzy agility evaluation is deployed to spot and rank Agile Supply Chain Attributes (ASCA) of ISM identified driver enablers. The fuzzy system addressed uses linguistic variables, MATLAB & fuzzy Technique for Order Preferences by Similiarity to Ideal Solution (TOPSIS) methods for the tabulation of Fuzzy Agility Index (FAI), Fuzzy Merit Important Index (FMII) and ranking the scores of ASCA. This attempt may provide firms with engrossed information in the design of agile supply chains which will be dominant competitive vehicles in future.

Keywords: *Intelligent Manufacturing, Interpretive Structural Modeling, Structural Self Interaction Matrix, Fuzzy Agility Index, Fuzzy Merit Important Index, MATLAB.*

1. Introduction

The prime focus of any supply chain is to organize internal and external resources of an economic enterprise comprehensively. Off late, success measures for manufacturing firms were thought of as lower production costs, shorter production times, shorter lead times, lesser inventory, reliable delivery times, higher quality and better customer satisfaction. In recent past, success levels are mostly determined by balancing demand, supply and production and, hence, the concept of supply chain has emerged. Managing a supply chain effectively is a generative complex problem, with the growing levels of uncertainty and complex interrelationships. An efficient integration of production and distribution functions into a unified flexible entity is vital for competitive advantage. Most studies focused on traditional, analytical and orthodox methods for identifying critical ASCA. The present attempt, however, is to model the agility problem using fuzzy systems. The hypothesis of the present paper is that fuzzy modeling is an appropriate tool for a supply chain to become responsive, adaptive and flexible.

Complex and dynamic interactions between supply chain entities lead to a considerable uncertainty in planning. Uncertainty tends to propagate the supply chain up and down. Many proposed strategies for mitigating this bullwhip effect have a history of successful application . This effect leads to inefficiencies in supply chains since it increases the cost for logistics, and it lowers its competitive ability [1]. According to Faisal *et al*. [2], an Agile Supply Chain (ASC) should acquire characteristics such as market sensitiveness, virtual integration, network integration and process alignment which provides the opportunity to understand the dynamics among the enablers of agility in a supply chain. Here, the GTA approach has been used to analyze supply chain agility from the perspective of key enablers as obtained from ISM. Mehdi abbasi *et al*. [3] have used ISM as a tool for the determination of the optimal manufacturing strategy by using expert opinion technique and also applied the seven step algorithm and MICMAC analysis to analyze the elements in a complicated supply chain system. Iyer and mohammed sagheer [4] focused on risk prioritization in public-private partnership projects. ISM, here, is used to prepare a hierarchical structure as well as to study the interrelationships of these risks that would enable decision makers to take appropriate steps. Kannan govindhan [5] attempted ISM in logistics where the model was used to identify and summarize relationships among the specific

* Corresponding author e-mail: balpurush@rediffmail.com.

attributes for selecting the best among the various third party logistic providers. Ching-torng lin [6] applied Fuzzy logics based on agility providers to determine the ranking of sub enablers deduced from ISM by calculating the fuzzy agility index comprising attribute rating and weights aggregated by average. Mir Aryanezhad [7] employed fuzzy topsis method using right and left scores to calculate the final ranking score among the selected sub enablers.

While several studies have steered the making of an ASC [2 - 7], a potential gap in combining them for extracting ASC driver enablers through ISM and prioritizing ASCA using Fuzzy approach ought to lend justification to this novel endeavor. The present paper is organized as follows: In section 2, ISM, SSIM, and RM model are developed; in section 3, estimation of fuzzy agility index and ranking of ASCA using fuzzy TOPSIS method are presented, followed by Results in section 4 and Conclusions in section 5.

2. ISM Methodology

ISM is a model that transforms unclear, poorly articulated models of systems into well-defined models. It is palpable that for a complex problem under consideration, a number of factors may be related and the direct and indirect relationships between the factors describe the situation far more accurately than the individual factor taken in isolation. ISM develops insights into collective understandings of these relationships. ISM starts with the identification of variables relevant to the problem and extends with a group problem solving technique by choosing a contextually relevant subordinate relation. Having decided on the element set and the contextual relation, SSIM is developed based on a pairwise comparison of variables. SSIM is later converted into a binary matrix called as the RM. Prominent ASC enablers referred in past literature are exhibited in Table 1.

Table 1. ASC Enablers

S.No	ASC Enablers	Reference
1.	Managerial control, Deliverability, Quality	[8]
2.	Organization role	[5]
3.	Strategic planning	[9]
4.	Cooperative behavior of chain members	[10]
5.	Information sharing, Reliability of information	[11]
6.	Production methodology, Time management	[12]

2.1. SSIM Matrix

Listed enablers and their interrelationships identified through interactive studies are depicted in Table 2 using 4 cyphers namely V, A, X and O were:

V: enabler i will augment enabler j;
A: enabler i will be augmented by the enabler j;
X: enabler i and j will augment each other;
O: enabler i and j are unrelated.

Table 2. Formation of SSIM matrix

S.No	ASC Enablers	Reference	10	9	8	7	6	5	4	3	2
1	Managerial control	[8]	V	A	O	V	O	O	O	A	O
2	Organizational role	[5]	A	O	O	O	X	O	O	X	
3	Quality	[8]	A	O	O	A	X	O	O		
4	Production methodology	[12]	V	V	A	O	X	O			
5	Deliverability	[8]	A	A	X	O	O				
6	Cooperative behavior of chain members	[10]	X	A	V	O					
7	Information sharing	[11]	X	V	V						
8	Strategic planning	[9]	A	O							
9	Time management	[12]	V								
10	Reliability of information	[11]									

2.2. Reachability Matrix

From the deduced SSIM matrix, the RM can be framed using alpha variables tabulated with binary numbers as shown in Table 3. This renders a methodology to calculate the driver and dependence values by summing up rows and columns respectively. The SSIM is transformed into a binary matrix, called RM by substituting 1 and 0 on behalf of V, A, X, O based on the following syntax.

- If the (i, j) entry in the SSIM is V, then the (i, j) entry in the RM becomes 1 and the (j, i) entry becomes 0.
- If the (i, j) entry in the SSIM is A, then the (i, j) entry in the RM becomes 0 and the (j, i) entry becomes 1.
- If the (i, j) entry in the SSIM is X, then the (i, j) entry in the RM becomes 1 and the (j, i) entry also becomes 1.
- If the (i, j) entry in the SSIM is O, then the (i, j) entry in the RM becomes 0 and the (j, i) entry also becomes 0.
- From the RM, the driver power of each element is obtained by the summation of 1's in the corresponding row. Similarly, dependence power of each element is obtained by the summation of 1's in the corresponding column.

Table 3. Reachability matrix

S.No.	ASC Enablers (ASC_i)	10	9	8	7	6	5	4	3	2	1	*Driver*
1	Managerial control	1	0	0	1	0	0	0	0	0	1	**3**
2	Organizational role	0	0	0	0	1	0	0	1	1	0	**3**
3	Quality	0	0	0	0	1	0	0	1	1	1	**4**
4	Production methodology	1	1	0	0	1	0	1	0	0	0	**4**
5	Deliverability	0	0	1	0	0	1	0	0	0	0	**2**
6	Cooperative behavior of chain Members	1	0	1	0	1	0	1	1	1	0	**6**
7	Information sharing	1	1	1	1	0	0	0	1	0	0	**5**
8	Strategic planning	0	0	1	0	0	1	1	0	0	0	**3**
9	Time management	1	1	0	0	1	1	0	0	0	1	**5**
10	Reliability of Information	1	0	1	1	1	1	0	1	1	0	**7**
	Dependence	**6**	**3**	**5**	**3**	**6**	**4**	**3**	**5**	**4**	**3**	

2.3. Classification of Enablers

From the findings of RM in the form of driver and dependence power of each ASC enabler, a graph is drawn were each element is plotted as a point using the conventional x-y coordinate system as depicted in Figure 1 in order to classify the four quadrants for the ease of viewing and analyzing. First quadrant consists of 'Autonomous enablers' posessing weak driver power and weak dependence. The 'Dependant enablers' constitute the second quadrant which has a weak driver power but a strong dependence. The third quadrant represents the 'Linkage enablers' that has a strong driving power and a strong dependence power. The fourth quadrant entails 'Driver enablers' having a strong driver power but a weak dependence. As per past research done on ISM, the driver enablers were often inferred for the improvement of agility levels as they have the potential to influence the other 3 quadrants. Accordingly, Driver enablers 4, 7, 9 were sidelined as per classification done similar to the one by Mandal *et al*. [13] and Faisal *et al* [14].

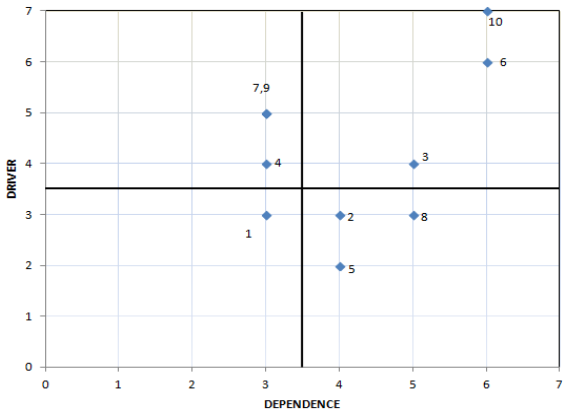

Figure 1. Classification of enablers

3. Fuzzy Modeling

Fuzzy logic is a technique suitable for dealing with uncertainty and subjectivity, which becomes an interesting supplementary approach to manage the performance of supply chains. It helps to deal with parameters that are difficult to express in a quantitative or a numerical measure and is used in making decisions with imprecise data. Due to its availability for representing uncertain values, fuzzy numbers are extensively used in many applications. In order to rank fuzzy numbers, one fuzzy number needs to be deployed, evaluated and compared with its counterparts or the median. Henceforth, to reduce the vagueness of the problem under study and to have a deep focus on ISM speckled driver enablers, Fuzzy agility evaluation is used on the basis of fuzzy logic systems.The evaluation can be done by classifying the sub enablers or attributes from driver enabler and by ranking them to improve supply chain agility.

Opulent review of related literature reveals that fuzzy logic has been applied for analyzing and monitoring the performance of supply chains, in developing models for strategy related performance outcomes and in developing methods for ranking fuzzy numbers for decision making from the viewpoints of users [15]. It has also served as a versatile tool in Multiple Criteria Decision Making (MCDM), arraying TOPSIS methods with fuzzy weighted averages [16]. Fuzzy logics have also been functional in the calculation of agility index in supply chains [6], designing optimal network for supply chain with fuzzy mathematical programming [17] and fractional programming for estimating fuzzy weighted averages in decision analysis [18].

3.1. Fuzzy Model Construction

3.1.1. Exploring ASCA Of ISM Identified Driver Enablers

The driver enablers identified from ISM were taken up for further studies and with the help of wide-ranging past literature, the ASCA pertaining to each of the driver enablers were surfaced as shown in Table 4.

Table 4. ASCA

ASC Driver Enablers (ASC_i)	ASCA of Driver Enablers ($ASCA_{ij}$)	Reference
Production methodology (ASC_4)	Fully automated inspection systems ($ASCA_{41}$)	[12]
	Management's interest towards investment on FMS concepts($ASCA_{42}$)	[12]
	Application of Lean manufacturing principles for waste elimination ($ASCA_{43}$)	[12]
	IT application to exercise better vendor and supplier management[11] ($ASCA_{44}$)	[12]
Information sharing (ASC_7)	Infrastructure support for information sharing($ASCA_{71}$)	[11]
	End to end connectivity ($ASCA_{72}$)	[11]
	Honesty in sharing the information ($ASCA_{73}$)	[11]
	Undistorted communication ($ASCA_{74}$)	[11]
Time management (ASC_9)	Scheduled activities ($ASCA_{91}$)	[12]
	IT based communication system ($ASCA_{92}$)	[12]
	Training programme on time management concepts ($ASCA_{93}$)	[12]
	Adoption of time compression technologies ($ASCA_{94}$)	[12]

3.1.2. Fuzzy Ratings & Weights Using Linguistic Levels

Fuzzy evaluation is used to find and elicit the negative factors in the supply chain to improve the agility levels. Using linguistic levels, shown in Table 5 [19], the corresponding ratings and weights given by the 5 identified experts as exhibited in Table 6 and Table 7 was instrumental in the tabulating the aggregate rating and weights.

3.1.3. Aggregating Fuzzy Ratings & Weights for Estimating FAI

The aggregate mean of fuzzy ratings and weights (Rij and Wij) were estimated using equations 1 & 2 where E denotes experts and n the number of experts for the ASC enabler i and ASC attribute j, the summary of which is exhibited in Table 8.

$$Rij = E1 + E2 + E3 + \cdots En/n \quad (1)$$

$$Wij = E1 + E2 + E3 + \cdots En/n \quad (2)$$

Table 5. Linguistic Levels

For Ratings		For Weights	
Linguistic variables	Fuzzy numbers	Linguistic variables	Fuzzy numbers
Worst (W)	(0, 0.05, 0.15)	Very Low (VL)	(0, 0.05, 0.15)
Very Poor (VP)	(0.1, 0.2, 0.3)	Low (L)	(0.1, 0.2, 0.3)
Poor (P)	(0.2, 0.35, 0.5)	Fairly Low (FL)	(0.2, 0.35, 0.5)
Fair (F)	(0.3, 0.5, 0.7)	Medium (M)	(0.3, 0.5, 0.7)
Good (G)	(0.5, 0.65, 0.8)	Fairly High (FH)	(0.5, 0.65, 0.8)
Very Good (VG)	(0.7, 0.8, 0.9)	High (H)	(0.7, 0.8, 0.9)
Excellent (E)	(0.85, 0.95, 1.0)	Very High (VH)	(0.85, 0.95, 1.0)

Table 6. Ratings of ASCA assigned by experts using linguistic levels

ASC_i	$ASCA_{ij}$	E1	E2	E3	E4	E5
ASC_4						
	$ASCA_{41}$	**E**(0.85,0.95,1.0)	**G**(0.5,0.65,0.8)	**G**(0.5,0.65,0.8)	**G**(0.5,0.65,0.8)	**F**(0.3,0.5,0.7)
	$ASCA_{42}$	**F**(0.3,0.5,0.7)	**F**(0.3,0.5,0.7)	**G**(0.5,0.65,0.8)	**G**(0.5,0.65,0.8)	**G**(0.5,0.65,0.8)
	$ASCA_{43}$	**E**(0.85,0.95,1.0)	**G**(0.5,0.65,0.8)	**F**(0.3,0.5,0.7)	**G**(0.5,0.65,0.8)	**VG**(0.7,0.8,0.9)
	$ASCA_{44}$	**P**(0.2,0.35,0.5)	**F**(0.3,0.5,0.7)	**P**(0.2,0.35,0.5)	**F**(0.3,0.5,0.7)	**F**(0.3,0.5,0.7)
ASC_7						
	$ASCA_{71}$	**E**(0.85,0.95,1.0)	**G**(0.5,0.65,0.8)	**G**(0.5,0.65,0.8)	**E**(0.85,0.95,1.0)	**G**(0.5,0.65,0.8)
	$ASCA_{72}$	**G**(0.5,0.65,0.8)	**VG**(0.7,0.8,0.9)	**G**(0.5,0.65,0.8)	**G**(0.5,0.65,0.8)	**VG**(0.7,0.8,0.9)
	$ASCA_{73}$	**G**(0.5,0.65,0.8)	**VG**(0.7,0.8,0.9)	**G**(0.5,0.65,0.8)	**F**(0.3,0.5,0.7)	**F**(0.3,0.5,0.7)
	$ASCA_{74}$	**G**(0.5,0.65,0.8)	**VG**(0.7,0.8,0.9)	**G**(0.5,0.65,0.8)	**E**(0.85,0.95,1.0)	**G**(0.5,0.65,0.8)
ASC_9						
	$ASCA_{91}$	**E**(0.85,0.95,1.0)	**F**(0.3,0.5,0.7)	**G**(0.5,0.65,0.8)	**G**(0.5,0.65,0.8)	**VG**(0.7,0.8,0.9)
	$ASCA_{92}$	**E**(0.85,0.95,1.0)	**G**(0.5,0.65,0.8)	**F**(0.3,0.5,0.7)	**G**(0.5,0.65,0.8)	**G**(0.5,0.65,0.8)
	$ASCA_{93}$	**F**(0.3,0.5,0.7)	**VG**(0.7,0.8,0.9)	**VG**(0.7,0.8,0.9)	**G**(0.5,0.65,0.8)	**G**(0.5,0.65,0.8)
	$ASCA_{94}$	**F**(0.3,0.5,0.7)	**G**(0.5,0.65,0.8)	**E**(0.85,0.95,1.0)	**G**(0.5,0.65,0.8)	**G**(0.5,0.65,0.8)

Table 7. Weights of ASCA assigned by experts using linguistic levels

ASC_i	$ASCA_{ij}$	E1	E2	E3	E4	E5
ASC_4		**H**(0.7,0.8,0.9)	**VH**(0.85,0.95,1.0)	**VH**(0.85,0.95,1.0)	**H**(0.7,0.8,0.9)	**VH**(0.85,0.95,1.0)
	$ASCA_{41}$	**H**(0.7,0.8,0.9)	**H**(0.7,0.8,0.9)	**FH**(0.5,0.65,0.8)	**FH** (0.5,0.65,0.8)	**H**(0.7,0.8,0.9)
	$ASCA_{42}$	**H**(0.7,0.8,0.9)	**H**(0.7,0.8,0.9)	**M**(0.3,0.5,0.7)	**H**(0.7,0.8,0.9)	**M**(0.3,0.5,0.7)
	$ASCA_{43}$	**M**(0.3,0.5,0.7)	**H**(0.7,0.8,0.9)	**M**(0.3,0.5,0.7)	**FH**(0.5,0.65,0.8)	**M**(0.3,0.5,0.7)
	$ASCA_{44}$	**M**(0.3,0.5,0.7)	**H**(0.7,0.8,0.9)	**H**(0.7,0.8,0.9)	**H**(0.7,0.8,0.9)	**H**(0.7,0.8,0.9)
ASC_7		**FH**(0.5,0.65,0.8)	**H**(0.7,0.8,0.9)	**FH**(0.5,0.65,0.8)	**FH**(0.5,0.65,0.8)	**FH**(0.5,0.65,0.8)
	$ASCA_{71}$	**VH**(0.85,0.95,1)	**H**(0.7,0.8,0.9)	**VH**(0.85,0.95,1.0)	**VH**(0.85,0.95,1.0)	**VH**(0.85,0.95,1.0)
	$ASCA_{72}$	**H**(0.7,0.8,0.9)	**VH**(0.85,0.95,1.0)	**VH**(0.85,0.95,1.0)	**VH**(0.85,0.95,1.0)	**VH**(0.85,0.95,1.0)
	$ASCA_{73}$	**H**(0.7,0.8,0.9)	**H**(0.7,0.8,0.9)	**FH**(0.5,0.65,0.8)	**FH** (0.5,0.65,0.8)	**H**(0.7,0.8,0.9)
	$ASCA_{74}$	**M**(0.3,0.5,0.7)	**H**(0.7,0.8,0.9)	**M**(0.3,0.5,0.7)	**FH**(0.5,0.65,0.8)	**M**(0.3,0.5,0.7)
ASC_9		**M**(0.3,0.5,0.7)	**M**(0.3,0.5,0.7)	**L**(0.1,0.2,0.3)	**FH**(0.5,0.65,0.8)	**FH**(0.5,0.65,0.8)
	$ASCA_{91}$	**H**(0.7,0.8,0.9)	**VH**(0.85,0.95,1.0)	**VH**(0.85,0.95,1.0)	**H**(0.7,0.8,0.9)	**VH**(0.85,0.95,1.0)
	$ASCA_{92}$	**H**(0.7,0.8,0.9)	**H**(0.7,0.8,0.9)	**M**(0.3,0.5,0.7)	**H**(0.7,0.8,0.9)	**M**(0.3,0.5,0.7)
	$ASCA_{93}$	**M**(0.3,0.5,0.7)	**H**(0.7,0.8,0.9)	**M**(0.3,0.5,0.7)	**M**(0.3,0.5,0.7)	**M**(0.3,0.5,0.7)
	$ASCA_{94}$	**H**(0.7,0.8,0.9)	**FH**(0.5,0.65,0.8)	**FH**(0.5,0.65,0.8)	**FH** (0.5,0.65,0.8)	**FH**(0.5,0.65,0.8)

Table 8. Average of Ratings and Weights

ASC_i	ASCAij	Average RatIngs (Rij)	Average WeightS (WIJ)
ASC_4			(0.79,0.89,0.96)
	$ASCA_{41}$	(0.53,0.68,0.82)	(0.62,0.74,0.86)
	$ASCA_{42}$	(0.42,0.59,0.76)	(0.54,0.68,0.82)
	$ASCA_{43}$	(0.57,0.7,0.84)	(0.42,0.59,0.76)
	$ASCA_{44}$	(0.26,0.44,0.62)	(0.62,0.74,0.86)
ASC_7			(0.54,0.68,0.82)
	$ASCA_{71}$	(0.65,0.77,0.88)	(0.82,0.920.98)
	$ASCA_{72}$	(0.58,0.71,0.84)	(0.82,0.920.98)
	$ASCA_{73}$	(0.46,0.62,0.78)	(0.62,0.74,0.86)
	$ASCA_{74}$	(0.61,0.74,0.86)	(0.42,0.59,0.76)
ASC_9			(0.34,0.5,0.66)
	$ASCA_{91}$	(0.57,0.71,0.84)	(0.79,0.89,0.96)
	$ASCA_{92}$	(0.53,0.68,0.82)	(0.54,0.68,0.82)
	$ASCA_{93}$	(0.54,0.68,0.82)	(0.38,0.56,0.74)
	$ASCA_{94}$	(0.53,0.68,0.82)	((0.54,0.68,0.82)

3.1.4. Associating FAI with agility levels

Fuzzy Agility Index (FAI) is an information fusion composed of aggregate fuzzy ratings and weights [18] and is mathematically defined as presented in equation 3. Arithmetical findings reveal an FAI value of (0.5035,0.6770,0.8038) which can be associated with natural language Agility Level (AL) expression shown in Table 9, to estimate the FAI of the case with the employability of Euclidean distance method. Assuming U_{FAI} and U_{ALi} represents membership functions of FAI and natural language agility i, respectively, the distance between FAI and AL is calculated using equation 4 and designed using MATLAB as depicted in Figure 2.

$$FAI = \sum_{j=1}^{n}(Wij)(Rij)/\sum_{j=1}^{n} Wij \quad (3)$$

$$d(FAI, ALi) = \left\{\sum_{x\in p} U_{FAI}(x) - U_{AL_i}(x))^2\right\}^{1/2} \quad (4)$$

Table 9. Agility Levels

Slowly Agile (S)	(0.0,0.1,0.2)
Low Agile (LA)	(0.1,0.2,0.3)
Slightly Agile (SA)	(0.2,0.3,0.4)
Fairly Agile (F)	(0.3,0.4,0.5)
Agile (A)	(0.4,0.5,0.6)
High Agile (HA)	(0.5,0.6,0.7)
Very Agile (VA)	(0.6,0.7,0.8)
Extremely Agile (EA)	(0.7,0.8,0.9)
Definitely Agile (DA)	(0.8,0.9,1.0)

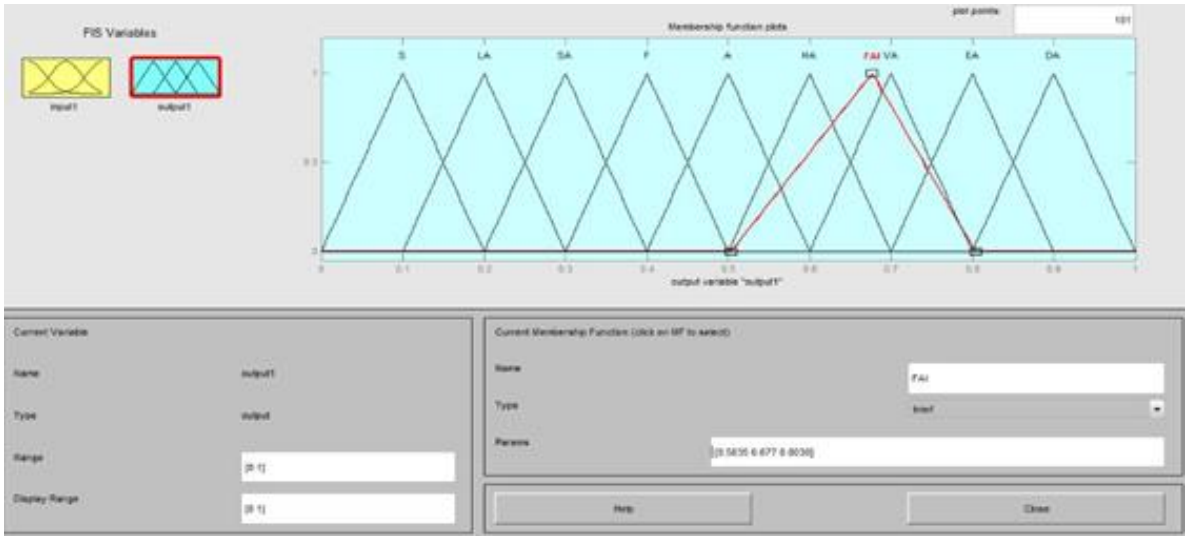

Figure 2. Distance measures in MATLAB

The results of the distances between FAI and AL formulated using equation 4 are exhibited in Table 10. As per the support given by previous researchers [19], the closest natural expression with the smallest distance is identified. Accordingly, the minimum value of the focused case is 0.0436 which clearly indicates the system to be 'very agile'.

3.1.5. Estimating FMII

The degree of contribution of supply chain agility for a factor decreases with decreasing FMII and thus leverages in identifying principal obstacles. To avoid the effect of neutralization, FMII is defined as shown in equation 5 and summarized in Table 11.

$$\text{FMII} = \text{Rij}(.)[(1,1,1) - (\text{Wij})] \quad (5)$$

3.1.6. Calculating Right, Left and Ranking Scores using Fuzzy TOPSIS

The proposed fuzzy TOPSIS method mainly accounts for systematic evaluation and ranking of attributes from the integrated rating and weights and the performance values. Supposing FMII scores to resemble aij,bij and cij, the left score [UL(FMII)], right score [UR(FMII)] and the ranking score [UT(FMII)] of ASCA were obtained using equation 6,7 & 8, respectively, where i denotes ASC enabler and j denotes ASC attribute as shown in Table 11.

$$\text{UL(FMII)} = (\text{LS})\text{ij} = (\text{bij})/1 + (\text{bij}) - (\text{aij}) \quad (6)$$

$$\text{UR(FMII)} = (\text{RS})\text{ij} = (\text{cij})/1 + (\text{cij}) - (\text{bij}) \quad (7)$$

$$\text{UT(FMII)} = [\text{UR(FMII)} + 1 - \text{UL(FMII)}]/2 \quad (8)$$

Table 10. FAI Distance summary

d(FAI,S)	d(FAI,LA)	d(FAI,SA)	d(FAI,F)	d(FAI,A)	d(FAI,HA)	d(FAI,VA)	d(FAI,EA)	d(FAI,DA)
0.5700	0.4702	0.3705	0.2709	0.1720	0.5188	0.0436	0.1343	0.3252

Table 11. Fuzzy Merit Important Indexes and Ranking scores of ASCA

ASCAij	Rij	(1.0,1.0,1.0) (-)Wij	Fuzzy Merit- Important Indexes Rij (.) (1.0,1.0,1.0) (-) Wij	Left and right scores [UL,UR]	Ranking scores [UT]
ASCA41	(0.53,0.68,0.82)	(0.14,0.26,0.38)	(0.0742,0.1768,0.3116)	(0.1603,0.2745)	0.5571
ASCA42	(0.42,0.59,0.76)	(0.18,0.32,0.46)	(0.0756,0.1888,0.3496)	(0.1696,0.3011)	0.5657
ASCA43	(0.57,0.7,0.84)	(0.24,0.41,0.58)	(0.1368,0.287,0.4872)	(0.2495,0.4059)	0.5782
ASCA44	(0.26,0.44,0.62)	(0.14,0.26,0.38)	(0.0364,0.1144,0.2356)	(0.1061,0.2101)	0.552
ASCA71	(0.65,0.77,0.88)	(0.02,0.08,0.18)	(0.013,0.0616,0.1584)	(0.0587,0.1444)	0.542
ASCA72	(0.58,0.71,0.84)	(0.02,0.08,0.18)	(0.0116,0.0568,0.1512)	(0.0543,0.1381)	0.5419
ASCA73	(0.46,0.62,0.78)	(0.14,0.26,0.38)	(0.0644,0.1612,0.2964)	(0.1469,0.2610)	0.5570
ASCA74	(0.61,0.74,0.86)	(0.24,0.41,0.58)	(0.1464,0.3034,0.4988)	(0.2622,0.4172)	0.5775
ASCA91	(0.57,0.71,0.84)	(0.04,0.11,0.21)	(0.0228,0.0781,0.1764)	(0.0740,0.1606)	0.5433
ASCA92	(0.53,0.68,0.82)	(0.18,0.32,0.46)	(0.0954,0.2176,0.3772)	(0.1939,0.3252)	0.5656
ASCA93	(0.54,0.68,0.82)	(0.26,0.44,0.62)	(0.1404,0.2992,0.5084)	(0.2581,0.4204)	0.5811
ASCA94	(0.53,0.68,0.82)	(0.18,0.32,0.46)	(0.0954,0.2176,0.3772)	(0.1939,0.3252)	0.5656

4. Results and Discussion

Malignancies disfavoring an agile enterprise challenge the managers and policy makers. The evaluation of agility is gaining extreme importance as it is an indicator of the organisational excellence. A few researchers contributed approaches for measuring agility in past, but since conventional agility measurement has always been associated with vagueness and complexity, the fuzzy logic approach is used in the study [12]. The proposed model provides an opportunity to understand the dynamics among the enablers and attributes of an ASC. Unlike many of MCDM methods, the proposed fuzzy TOPSIS method is easy to use, and it considers the decision-maker's preference and enjoys a low computational volume and flexibility [7]. A few notable results drawn from identifying and investigating the interactions between crtitical attributes; these are:

- ISM classification of enablers reveals that Production Methodology (ASC_4), Information Sharing (ASC_7) and Time Management (ASC_9) are the driver enablers where the firm should place high precedence.
- The outcomes of FAI tabulations classifies the existing system to be 'very agile' and exemplifies the margins of difference on desired agility levels.
- Fuzzy TOPSIS prioritization of ASCA of ISM acknowledged driver enablers, emphasizes that the priority should start from End to end connectivity ($ASCA_{72}$) which has the minimum ranking score of 0.5419 and progress onwards till Training programme on time management concepts ($ASCA_{93}$) which has the maximum ranking score of 0.5811.

5. Conclusions

The agility paradigm has become an important avenue in modern manufacturing. World class organizations are attempting to gain competitive advantage by impinging agile concepts in their supply chain. Achieving agility lies in designing agile friendly processes and, thus, firms need to concentrate on their supply chains and their enablers in the attempt of redressing themselves as responsive supply chains[20]. Ample opportunities exist for the growth of this field due to its multi-functional and interdisciplinary focus [21]. The present study aimed to develop a quantitative analysis framework for organizations to identify their weakness in supply chains. ISM and fuzzy theory has been effectively utilized to handle the imprecision and vagueness of ASC enablers and ASC attributes congruently. The study addresses the question of how to measure and improve supply chain agility as we can't manage what we can't measure. The uniqueness of the model is in bridging the traditional concepts of ISM with the non-traditional concepts of fuzzy arithmetics. This trial has doubtlessly presented a model for future managers to spot uncertainties in business and demonstrated an unprecedented application of fuzzy logic systems. In lines of novelty, the model will opine the following features:

- The model is a scientific approach to identify ASC enablers and roots itself with betterment plans by generating ASC attributes.
- The FAI provides a holistic picture of agility and, thus, helps managers to perform gap analysis between existing agility levels and desired levels of the subject under limelight.
- The model facilitates supply chain managers for swift and effective MCDM.
- Considering and investigating the roots of agility enablers could show directions for further research. Targeting the relationships between these enablers and its capabilities could set the platform for the design of a perfect agile supply chain in future.

References

[1] B. Chandra Mohana Reddy, K. Hemachandra Reddy, C. Nadha Muni Reddy, K. Vijaya kumar Reddy, "Quota Allocation to Distributors of the Supply Chain under Distributors' Uncertainty and Demand Uncertainty by Using Fuzzy Goal Programming". Jordan Journal of Mechanical and Industrial Engineering, Vol. 2 (2008) No.4, 215-226.

[2] M.N. Faisal, D.K. Banwet, R. Shankar, " Supply chain agility : Analysing the enablers". International Journal of Agile systems and Management, Vol. 2 (2007) No.1, 76-91.

[3] Mehdi Abbasi, Mohsen Akbarpour Shirazi, Mir Bahador Aryanezad, "Determination of manufacturing strategy using interpretive structural". African Journal of Business Management, Vol. 6 (2012) No. 3, 881 – 887.

[4] K. C. Iyer, Mohammed Sagheer, " Hierarchical Structuring of ppp risks using interpretive structural modeling". Journal of Construction Engineering and Management, Vol. 136 (2010), 151-159.

[5] Kannan Govindan, Murugesan Palaniappan, QinghuaZhu, Devika Kannan, "Analysis of third party reverse logistics provider using interpretive structural modeling". International Journal of Production Economics, Vol. 140 (2012) No. 1, 204-211.

[6] Ching Torng Lin, Chen Tung Chen, "A fuzzy – logic based approach for new product go/nogo decision at the front end". IEEE Transactions on Systems, Man and Cybernetics – Part a: Systems and Humans", Vol. 34 (2004) No.1, 132-142.

[7] Mir. B. Aryanezhad, M.J. Tarokh, M.N. Mokhtarain, F.Zaheri, "A Fuzzy TOPSIS method based on left and right scores". International Journal of Industrial Engineering and Production Research, Vol. 22 (2011) No.1, 51-62.

[8] Shiri. D Vivek, D. K. Banwet, Ravi Shankar, "Analysis of interactions among core, transaction and relationship-specific investments: The case of offshoring". Journal of Operations Management, Vol. 26 (2008) No. 2, 180-197.

[9] Vimal Kumar Eswarlal , Prasanta Kumar Dey, Ravi Shankar, "Enhanced Renewable Energy Adoption for Sustainable Development in India: Interpretive Structural Modeling Approach". World Renewable Energy Congress, (2011) No. 5, 351-358.

[10] S. K. Sharma, B. N. Panda, S. S. Mahapatra, S. Sahu, "Analysis of Barriers for Reverse Logistics: An IndianPerspective". International Journal of Modeling and Optimization, Vol. 1 (2011) No. 2, 101-106.

[11] M .K. Khurana, P.K. Mishra, Rajeev Jain, A. R. Singh, " Modeling of information sharing enablers for building trust in Indian Manufacturing Industry: An Integrated ISM and Fuzzy, MICMAC Approach". International Journal of Engineering Science and Technology, Vol. 2 (2010) No.6, 1651-1669.

[12] S. Vinodh, S. R. Devadasan, " Twenty criteria based agility assessment using fuzy logic approach". International Journal of Advanced Manufacturing Technology, Vol. 54 (2011) No. 9-12, 1219-1231.

[13] A.Mandal, S.G. Deshmukh, "Vendor selection using interpretive structural modeling (ISM)". International Jounal

of Operation and Production Management, Vol.14 (1994) No.6, 52-59.

[14] M.N.Faisal, D.K. Banwet, R. Shankar, " Supply chain risk mitigation : Modeling the enablers". Business Process Management Journal, Vol. 12 (2006) No. 4, 535-552.

[15] H. Lee Kwang, Jee Hyong Lee, " A Method for ranking fuzzy numbers and its application to Decision making". IEEE Transactions on fuzzy systems, Vol.7 (1999) No.6, 677-685.

[16] S. R. Ansari, P.K. Mittal, Ritu Chandna, " Multi-criteria decision making using fuzzy logic approach for evauating the manufacturing flexibility". Journal of Engineering and Technology Research, Vol. 2 (2010) No. 12, 237-244.

[17] Mostafa Maleki Someah Lu, Alireza Irajpour, Naser Hamidi, Reza Kiani Mavi., "Designing Excellent Supply Chain Network in Uncertainty Environment with Fuzzy Logic". International Journal of Business and Management, Vol. 6 (2011) No.4, 241-251.

[18] Chiang Kao,Shiang Tai Liu, "Fractional programming approach to fuzzy weighted average". Fuzzy Sets and Systems, Vol. 120 (2001) No.3 , 435-444.

[19] Ching Torng Lin, Hero Chiu, Po Young Chu, "Agility index in the supply chain". International Journal of Production Economics, Vol. 100 (2006) No. 2, 285–299.

[20] M. Balaji, V. Velmurugan, N.R. Arun kumar, "Creating agile supply chains by TADS". Latin American Applied Research, Vol. 44(2014), 345-350.

[21] Arvind Jayant, P. Gupta, S.K. Garg, "Perspectives in Reverse Supply Chain Management(R-SCM): A State of the Art Literature Review". Jordan Journal of Mechanical and Industrial engineering, Vol. 6(2012) No.1, 87-102.

JJMIE

Jordan Journal of Mechanical and Industrial Engineering

Volume 10 Number 1, March.2016
ISSN 1995-6665
Pages 75- 83

Computational modeling of gaseous flow and heat transfer in a wavy microchannel

Aiman Alshare[*a], Wael Al-Kouz[a], Suhil Kiwan[b],
Ammar Al-khalidi[c], Montasir Hader[d]

[a]*Mechanical Engineering Department, German Jordanian University*
[b]*Mechanial Engineering Department, Jordan University of Science and Technology*
[c]*Engery Engineering Department, German Jordanian University*
[d]*Aeronautical Engineering Department, Jordan University of Science and Technology*

Received 7 Nov 2015 *Accepted 28 Feb 2016*

Abstract

The present work is an investigation of the developing gas flow and heat transfer through a wavy micro-channel. Computational fluid dynamics (CFD) is used to solve the fluid flow and energy equations along with the slip flow and temperature jump boundary conditions. The simulations are carried out using three wavy amplitudes for Knudsen number 0.025 to 0.1 in the slip flow regime. It is shown that increasing the wavy amplitude results in augmentation of the heat transfer rate at the cost of increasing the frictional losses. However, the rarefication has a declining effect on both friction factor and Nusselt number. Correlations for the friction factor and Nusselt number as function of amplitude and Knudsen number are provided.

Keywords: *Wavy, microchannel, slip flow, temperature jump, Knudsen number*.

Nomenclature

A	amplitude of the wave (m)
C_f	skin friction coefficient
e_{Cf}	the ratio of wavy channel friction coefficient to that of planar channel
e_{Nu}	the ratio of wavy channel Nusselt number to that of planar channel
D_H	hydraulic diameter of the channel (m)
E	total energy
h	heat transfer coefficient (W/m^2 K)
H	the channel Height (m)
k	thermal conductivity of air (W/m.K)
k_B	the Boltzmann constant (J/K)
Kn	Knudsen number
L	length of single wave of the computational domain (m)
Ma	Mach number
n	unit vector normal to solid wall
Nu(x)	local Nusselt number
Nu	average Nusselt number
p	pressure (Pa)
$\bar{R}$	universal gas constant
Re	Reynolds number
s	wavy wall stream-wise local coordinate
t	unit vector tangent to solid wall
T	temperature, K
T_w	microchannel wall temperature, K
U_o	average velocity at inlet, m/s
V	velocity vector
WU	upper wall microchannel boundary
WL	lower wall microchannel boundary
x	axial coordinate, m
y	vertical coordinate, m

Greek Symbols

γ	ration of the specific heat (c_p/c_v)
λ	molecular mean free path (m)
λ_0	Length of the wave (m)
ν	kinematic viscosity
ρ	density of air, given by ideal gas equation (P/RT), Kg/m^3
σ	Lennard-Jones characteristic length (A^o)
σ_T	thermal accommodation coefficient
σ_v	momentum accommodation coefficient
τ_w	Wall shear stress (pa)

* Corresponding author e-mail: Aiman.Share@gju.edu.jo.

1. Introduction

Design and fabrication of micro-electro mechanical systems (MEMS) have increased the need for understanding fluid flow and heat transfer due to wide spread use in micro-fluidic devices, micro heat exchangers, biological and medical applications. In gaseous flows the two-counter competing effects rarefaction and compressibility influence the physics of the flow in micro-scale systems. The slip effect is dominant when the characteristic length becomes comparable to the mean free path of the fluid molecules in the microchannel, or at low-pressure gas flows in ordinary channel.

To enhance the heat transfer characteristics the traditional way is the inclusion of finned surface as in the study by Yeom et al. [1] where a micro-pin fin array is micro-fabricated in a rectangle channel for thermal management in electronics. A maximum enhancement in the heat transfer of nearly 79% over the planar channel was found and it was attributed to the flow dynamics around the pin fins rather than the increase in heat transfer area since the array with larger pin diameter was superior to the array with smaller diameter, although the latter had greater overall surface area, since the porosity is lesser.

Departing from planar channel is typically associated with increased pressure drop penalty. A micro scale gas flow in a channel with three protruding steps carried out by Bakhshan et al. [2] showed the rarefication and inclusion of obstructing steps in the channel had a competing effect on pressure drop pently. Inserting a convergent divergent section in planar channel reduces the mixing length of two gas mixer was shown in a study by Darbandi and Sabouri [3] where Monte Carlo (DSMC) the solution method employed.

Kiwan and Al-Nimr [4] investigated convection over linearly stretched, isothermal microsurface via similarity solution of the boundary layer equations. They presented correlations for skin friction coefficient and Nusselt number in terms of velocity slip, and temperature slip parameters. Kiwan and Al-Nimr [5] also showed that complete similarity solution is possible for boundary layer flows only for a stagnation flow over isothermal microsurface. They found that skin friction coefficient is inversely proportional to both the slip velocity parameter and local Reynolds number. Shakir et al. [6] investigated flow and heat transfer in counter-flow rectangular microchannel heat exchanger for 3-D, laminar, incompressible, steady state, slip, airflow. It is found that the effectiveness decrease with increasing Re and increasing Kn number.

In an analysis of corrugation amplitude of two-dimensional steady laminar and incompressible liquid flow in micro-channel, Castellões et al. [7] found that increasing the amplitude corresponds to enhancement of the local heat transfer in comparison with the smooth parallel-plate channel. Zhang et al. [8] studied the effect of viscous heating on cooled and heated walls with other wall adiabatic in parallel flow microchannel. It was concluded that for a heated wall, viscous heating acts as volumetric heat source and raises the temperature of the cold fluid thus reducing the temperature difference between the wall, and fluid, which decreases the heat transfer and Nusselt.

Hooman and Ejali [9] presented closed form solutions for hydrodynamically and thermally fully developed, forced convection for both parallel plate and circular micro-channels using both no-slip and slip-flow forced convection of a liquid and a gas with temperature-dependent properties. It was shown that the Nusselt number decrease with increasing Kn number and slightly decreased with Brinkman number due to viscous dissipation. Ji et al. [10] investigated the roughness effects on friction factor using rectangular elements on two parallel plates with different spacing and heights. It is found that the effect of wall roughness reduces with increasing Knudsen number. Morini et al. [11] investigated the conditions for rarefaction effects on the pressure drop. It was demonstrated that for a fixed geometry of the microchannel cross-section, it is possible to determine the minimum value of the Knudsen number for which the rarefaction effects can be observed experimentally. Rached and Dahar [12] numerically investigated the effects of Knudsen number on the velocity and temperature fields for the microchannel flow.

The effects of rarefaction have been examined for simultaneously developing 2-D laminar, incompressible, constant-property flows in rectangular microchannels. Demsis et al. [13] conducted experiments using different gases in circular, and square cross-section channels with various wall roughnesses. They used a scaled-up version by employing low pressure in the test section. The ranges of Knudsen number and Reynolds numbers covered in this study were 0.0022– 0.024 and 0.54 –13.2 respectively. The results suggest that fRe (Poiseuille number) in the slip regime decreases monotonically with an increase in Knudsen number from continuum-laminar value of 64, for all the conditions studied. The results signify that the friction factor responds to changes in gas, tube material and geometry of cross-section. Further, fRe increases with an increase in wall roughness. Experiments conducted with copper and stainless steel as pipe material indicated that fRe is lower for the copper wall case than that of stainless steel pipe. The value of fRe for oxygen, nitrogen and argon in same hydraulic diameter, same roughness and same cross-section pipe is close.

ALsqirate et al. [14] provided heat transfer and pressure drop correlations for CO_2 flow in mini and micro tubes under superheated conditions; analytical and experimental results are found to be in good agreement. Demsis et al. [15-16] experimentally investigated flow channel with low pressure simulating slip flow in microchannel and reported unusually Nusselt number correlation, which is proportional to both Reynolds number and Brinkman number, and inversely proportional to Knudsen number. The reported Nusselt number values for the slip flow are two-five orders of magnitude less than the corresponding values in the continuum flow regime. Zade et al. [17] studied the effects of variable physical properties on the flow and heat transfer characteristics of simultaneously hydrodynamically and thermally developing slip-flow in rectangular microchannels with constant wall temperature; channel aspect ratios are studied at different Knudsen numbers. For instance, for a temperature difference of 50 K, the change in the Nusselt number in the entrance and fully developed regions can be as high as 20% and 15%, respectively.

* Corresponding author e-mail: aiman.share@gju.edu.jo.

Mohammed et al. [18] numerically investigated the effect of various microchannel shapes such as zigzag, curvy, and step with rectangular cross-section on the overall thermal and hydraulic performance of water flow. Shojaeian et al. [19] employed three-dimensional numerical analysis for fully developed incompressible fluid flow and heat transfer through triangular microchannels over the slip flow regime. The influences of Knudsen, aspect ratio, and Reynolds number on the fluid flow and heat transfer characteristics are investigated. The results showed the rarefaction decreases the Poiseuille number, while its effect on the Nusselt number depends on the interaction between velocity slip and temperature jump. Gou and Li [20] reviewed and discussed the size effect impact on the flow and heat transfer characteristics in microchannel. Affirmed that the large surface to volume ratio in microchannel leads to higher friction factor and Nusselt numbers in comparison to the classical correlations. Sui et al. [21] Experimentally investigated friction and heat transfer in sinusoidal microchannels with rectangular cross sections using deionized water as the working fluid and the Reynolds numbers considered range from about 300 to 800. The results of Nusselt number and friction factor, for wavy microchannels are compared with those of baseline case of straight with the same cross section and footprint length. It is found that the heat transfer performance of the wavy microchannels is much better than that of straight baseline microchannels; at the same time the pressure drop penalty of the wavy microchannels can be much smaller than the heat transfer enhancement.

Shokouhmand and Bigham [22] investigated the developing fluid flow and heat transfer through a wavy microchannel numerically. The effects of creep flow and viscous dissipation are assumed. The results show that Knudsen number has declining effect on both the C_f Re and Nusselt number and rarefaction increased the temperature jump and slip velocity. In a CFD study of laminar flow and heat transfer in periodic trapezoidal channel with semi-circular cross-section, Geyer et al. [23] found that, for no-slip flow; the heat transfer enhancements of up to four times of that of fully-developed flow in a straight pipe at relatively small pressure loss penalty. Guzmán et al. [24] studied the enhancement characteristics of heat transfer, through a transition scenario of flow bifurcations, in asymmetric wavy wall channels by direct numerical simulations of the mass, momentum and energy equations, using the spectral element method. Hossain et al. [25] studied the case of unsteady sine-shaped wavy module with periodic boundary condition. It is found that the flow becomes unsteady with self-sustained oscillation at low Re on the order of 130 - 205 depending on the inlet spacing of the channel. It is found that the both the unsteady flow and increasing amplitude of the channel increases the Nusselt number and friction factor.

A comprehensive review on gas flow in microchannels is given by Agrawal [26]. It is noted that flow in planar channels of different cross-section has been extensively studied and analytical solution obtained by various approaches agree reasonably well amongst each other. Agrawal [26] affirms that studies focused on complex microchannels holds a great practical importance, since frequently the microchannels may not be straight.

In the present work, a steady, two-dimensional analysis of airflow through a wavy microchannel with uniform wall temperature is investigated. At micro level, the surface effects became more important than volume effects and presents and opportunity of enhancement of thermal transport. The flow is assumed steady, laminar and developing hydrodynamically and thermally. The continuum governing equations along with Maxwell slip [27] and Smoluchowski [28] temperature boundary conditions are solved numerically. The effect of the wave amplitude on both the friction coefficient and Nusselt number is investigated for range of Knudsen numbers in the slip regime. Knudsen is defined as the ratio of molecular mean free path length, λ, to the channel hydraulic diameter, D_H.

2. Problem statement and solution methodology

We consider the flow of air at low pressure through an asymmetric wavy microchannel. The physical domain of the channel, which consists of five wavy units, is shown in Fig. 1. The microchannel wavy walls geometry is given as

$$y = A\,cos(2\pi x/\lambda_o) \tag{1}$$

Where A is amplitude of the wave and λ_o is length of wave. Here, three wave amplitudes are considered, the base case wavy channel amplitude is given by A1, whereas A2 and A3 are scaled from A1 by incrementing the amplitude by 25% and 50%, respectively, while maintain a constant wave foot-print. Hence, from a practical point of view if we are interested to cool a given surface with a specific designed geometry, we can adjust the degree of waviness of the channel to achieve the desired cooling rate.

The flow is assumed to be steady, two-dimensional and laminar. The fluid is assumed to be an ideal gas. Further, it is supposed that the flow is developing both hydrodynamically and thermally. The continuum governing equations are utilized in conjunction with the slip velocity and temperature jump boundary conditions. The continuity, momentum and energy equations governing the flow and heat transfer in the microchannel under consideration, are as follows

$$\nabla \cdot \rho\vec{V} = 0 \tag{2}$$

$$\left(\nabla.\rho\vec{V}\right) = -\nabla p + \mu\nabla^2\vec{V} \tag{3}$$

$$\nabla \cdot \left(\vec{V}\ (\rho E + p)\right) = k\nabla^2 T + \mu\Phi \tag{4}$$

Where $E = h - \frac{p}{\rho} + \frac{v^2}{2}$ and Φ is viscous dissipation.

The boundary conditions associated with the governing equations for the problem are:

Slip-condition and temperature jump at the channel walls; reported by Lokerby et al. [29] and Colins [30] as follows

$$u_s = \left(\frac{2-\sigma_v}{\sigma_v}\right)\lambda\left(\frac{\partial u_t}{\partial n} + \frac{\partial u_n}{\partial t}\right) \tag{5a}$$

$$T_s = \left(\frac{2-\sigma_T}{\sigma_T}\right)\frac{2\gamma}{\gamma+1}\frac{k}{\mu c_v}\lambda\left(\frac{\partial T}{\partial n}\right) \tag{5b}$$

The mean free path length is specified as follows:

$$\lambda = \frac{k_B T}{\sqrt{2}\pi\sigma^2 P} \tag{6}$$

Where $k_B = 1.38066 \times 10^{-23}\, JK^{-1}$ is the Boltzmann constant, T the temperature, P the pressure and σ the Lennard-Jones characteristic length of air.

The inlet gas temperature is specified to be T_{in} = 300K, while the wall temperature is maintained at 345 K. Relating the Knudsen number, to the Reynolds number and Mach number as follows specifies the mass flow rate at the channel inlet

$$Kn = k_2\sqrt{\gamma}\frac{Ma}{Re} \quad (7)$$

Where, γ, is the specific heat ratio of the gas and the constant, $k_2 = \sqrt{\pi/2}$ is of the Maxwell model. This relationship shows the linking between rarefication and compressibility as explained in gas flows within a microchannel, detailed theoretical accounting of this is given by Colin [30]. It is noteworthy that at high *Re* the effect of *Ma* (compressibility) is significant, however, for low *Re* the *Kn* effect (rarefaction) is dominant. The governing equations along with the boundary conditions are solved in utilizing the Finite Volume Method (FVM). The computational domain consists of five-wave geometry as specified by Eq. (1). Progressions of meshes with increasing sizes, (200×110), (250×130), (300×150), and (350×170) are tested to select an optimal mesh size. The effect of mesh refinement on average Nusselt number and friction factor is shown in table 1. A non-uniform, quad mapped, mesh consisting of 45,000 elements is found to be adequate for all computation (For clarity the mesh of only the third wave is shown in Fig. 1). The steady governing equations were spatially discretized using the 2nd order upwind scheme. Pressure-velocity decoupling is handled using the SIMPLE algorithm [31]. The mean free path is calculated using the inlet condition temperature in K, and the operating pressure, in Pa, which is taken as one tenth of atmospheric pressure. Assuming totally thermally diffuse walls, the thermal accommodation coefficient, σ_T, is taken as unity for all the simulations. In a review of measurement techniques of the momentum accommodation factor, Agrawal and Prabhu [32] suggested a value of 0.926 for momentum accommodation factor, σ_v that is adopted in these in all the simulations.

Reynolds number of value two is considered in this study, which results in slight compressibility affects. Knudsen number was varied from 0.025 to 0.1, which is considered within the slip flow regime rarefaction is expected to dominate compressibility. The mass flow rate at the channel inlet is calculated using Eq. (7) above that relates the Mach number to the Knudsen number and Reynolds number.

The residuals for the convergence were monitored and solutions are deemed converged when the mass and velocity residuals were less than 10^{-7} and the energy residual are less than 10^{-9}. The local skin friction, $C_f(s) = \frac{\tau_w(s)}{\frac{1}{2}\rho\,\bar{U}^2}$ and local Nusslet number, $(s) = \frac{h\,D_H}{k}$, Where the heat transfer coefficient is computed using the local heat flux, wall temperature and a reference temperature, which is taken, as the film temperature. Whereas, the average Nusselt number is based on the total heat transfer rate and the inlet and outlet bulk temperatures.

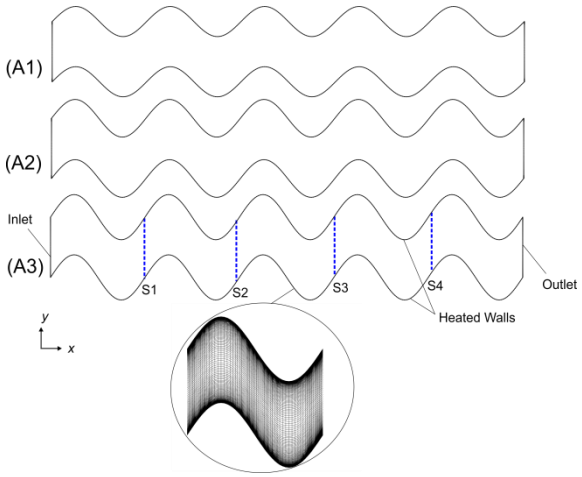

Figure 1 The geometry used for the computational domain, three amplitude and fixed

3. Results and Discussion

The velocity profiles are shown in Fig. (2a) for case of microchannel with amplitude A1. It can be observed that the slip velocity increases with increased rarefication, and is nearly 24%, 51%, and 67% of the average velocity, for Kn number 0.025, 0.075, and 0.1, respectively. At high Kn number the slip velocity on the lower channel wall is greater than on the upper wall, which corresponds to local acceleration of the flow. The increase in rarefication increases wall slip, which results in flattening of the velocity profiles. Also we note that the peak velocity does not coincide with centerline of the channel due to the centripetal acceleration of the flow caused by the local curvature and the peak velocity shifts toward the lower channel wall with increasing Kn number. The asymmetry in flow is evident by inspecting the local friction factor depicted in Fig. (2b), which indicates that the shear stress on the upper and lower walls is out of phase.

Table 1. Grid independent study

	cf	Nu	cf	Nu
Mesh size	Kn 0.025		Kn 0.1	
200, 100	2.5725E-02	2.1023E+01	3.6125E-03	1.0047E+01
250, 130	2.5536E-02	2.0730E+01	3.5609E-03	9.9484E+00
300, 150	2.5472E-02	2.0533E+01	3.5247E-03	9.8801E+00
% Error	0.739	1.417	1.449	0.993
% Error	0.253	0.958	1.027	0.691

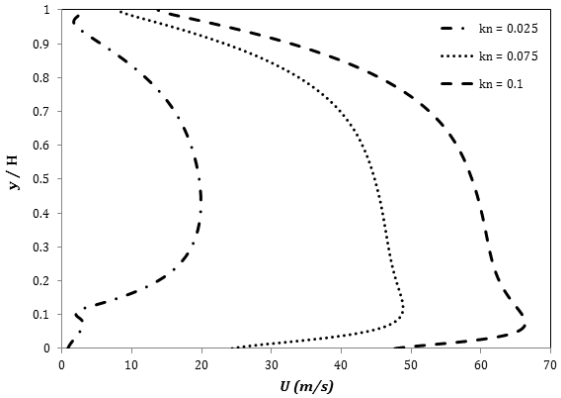

Figure 2a. Velocity profile at middle section of the wavy channel with amplitude, A1, shows the effect of Kn number on the velocity slip.

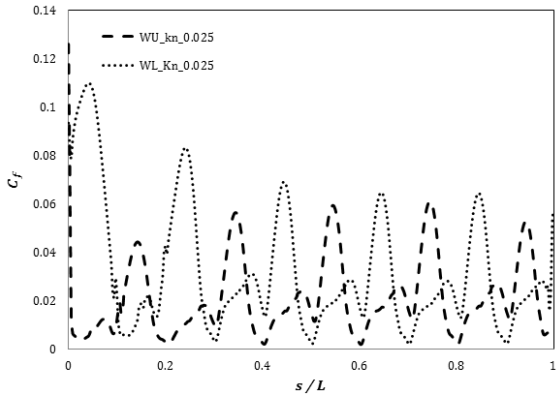

Figure 2b. Local friction coefficient vs. dimensionless stream-wise location, for the microchannel with amplitudes, A1, at the upper and lower channel walls, Kn = 0.025.

Figure 3 illustrates the effect of Kn numbers 0.025 and 0.1 on the flow field in terms of the velocity vectors and the corresponding stream function plots for case of microchannel with amplitude, A1. The vector plots shows maximum slip velocity in the vicinity of concave section of the wall and recirculating flow near the convex sections of the wall. The slip velocity significantly increase with increased rarefication effect as can be seen in velocity vector plots of Figure 3, Kn = 0.025 (left) in contrast to Kn = 0.1 (right). It is interesting to note the asymmetry in recirculating flow regions near the upper and lower walls as illustrated by stream function plots Fig. 3 (left) and Fig. 3 (right). Furthermore, the reduction in rarefication near the microchannel wall results in higher frictional losses as depicted in Fig. 4, for a given Knudsen number local friction coefficient varies along the channel dimensionless length. It can be observed that the frictional losses are extremely steep very near the channel entrance. However, there is a reduction of 50% in the frictional losses in the subsequent wave sections. The higher frictional losses at the inlet of the channel are related to uniform velocity boundary condition imposed there. However, spatial periodicity of the flow is almost established, after three waves, as illustrated by the similarity of the frictional-loss profiles of the fourth and fifth waves.

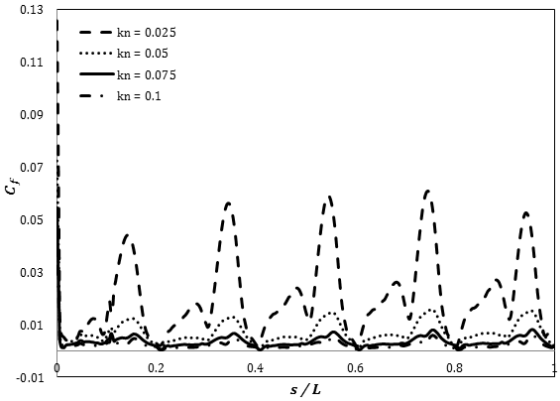

Figure 4. Friction coefficient vs. dimensionless stream-wise location, Kn = 0.025, 0.05, 0.075, and 0.1, wavy channel with amplitude A1.

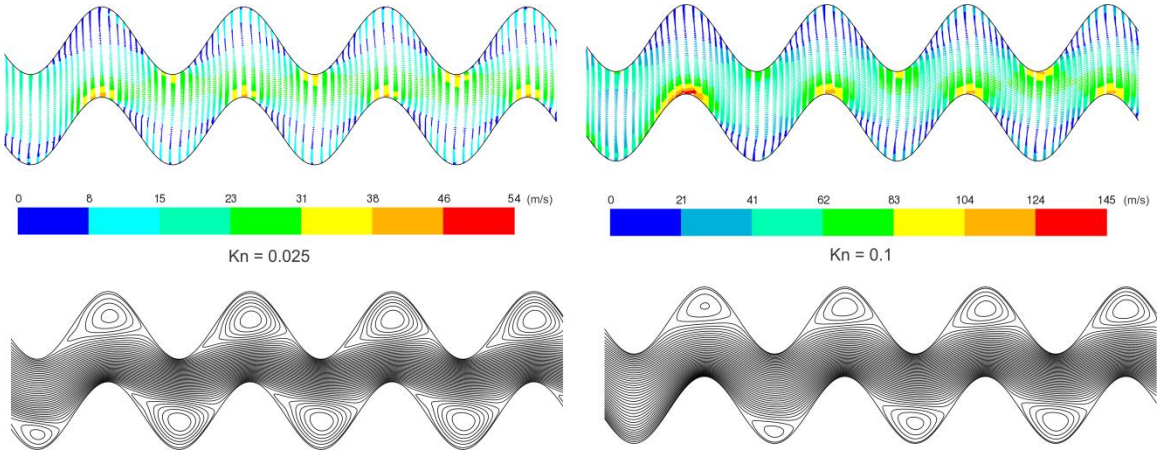

Figure 3. Velocity vectors and stream function, wavy channel with amplitude, A1, third wave in the center of the channel,

(a) Kn = 0.025, (b) Kn = 0.1

Figure 5 considers the simulation case of Knudsen number 0.5 for planar channel and three wavy channels with increasing amplitudes A1, A2, A3, respectively. For the hydrodynamically developing flow, in the case of planar channel, we observe the expected steep shear stress at channel entrance and tapering off with the development of the boundary layer. For the cases of wavy channel also we observed the spatially periodic behavior in the last three waves following a steep gradient at the inlet followed by developing flow in the first two-wave sections as mentioned earlier. It is interesting to note the effect of the wall shear stress as illustrated by the friction factor to increase with amplitude, due to increasingly tortuous path the flow must follow. An increase of the base amplitude by 25% on the average increases the local friction coefficient by nearly 50%.

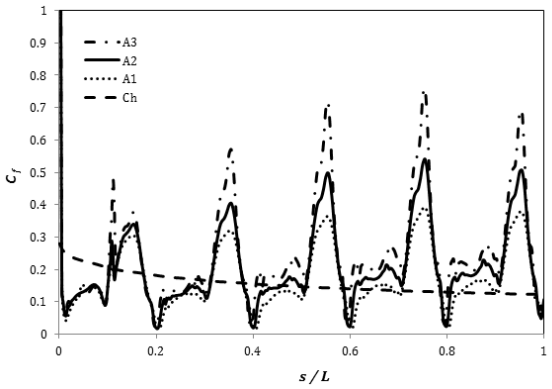

Figure 5. Friction coefficient vs. dimensionless stream-wise location, for the three wavy amplitudes and the planar channel, Kn = 0.05.

Figure 6 shows the temperature profiles at a cross-section in the middle of the microchannel. It can be noted that the fluid temperature near the wall diminishes with increased rarefication, or in other words as expected, increasing the Knudsen number results in increasing the temperature jump or an increase in rarefication affect result in flattening of the temperature profiles. The asymmetry in the temperature profiles is also inline with asymmetric in the velocity profiles, which was caused the varying local acceleration in the cross-stream direction. Presented in Fig. 7 is the effect of rarefication on the temperature field. Figure 7(b) shows the intensification of the temperature jump for case of Knudsen number 0.1, where the temperature contours near the wall are marginally higher than those near the microchannel centerline in contrast to the case of Kn number 0.025 illustrated in Fig 7(a), where we note significantly higher temperatures near the heated wall, particularly in the vicinity of the leeward portions of the channel. It can also be noted in Fig. 7(a) and Fig. 7(b); higher temperatures are found in the standing eddy regions where its expected that diffusion from these region to the core flow dominates convection. The variation in fluid density near the wavy boundaries and the core flow is caused by the compressibility effect, which increases with increasing Kn number as illustrated in Fig. 7(b).

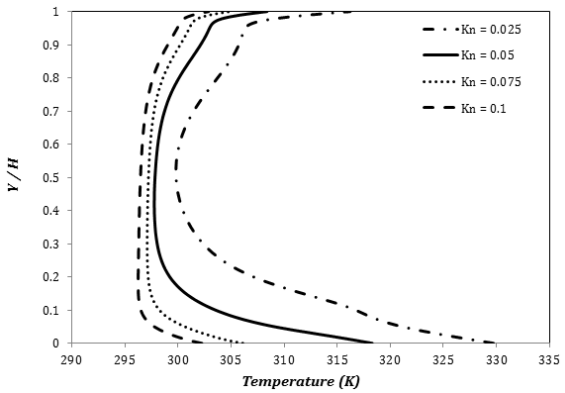

Figure 6. Temperature profile at S2, wavy channel with amplitude, A1, showing the effect of Kn number on the temperature jump.

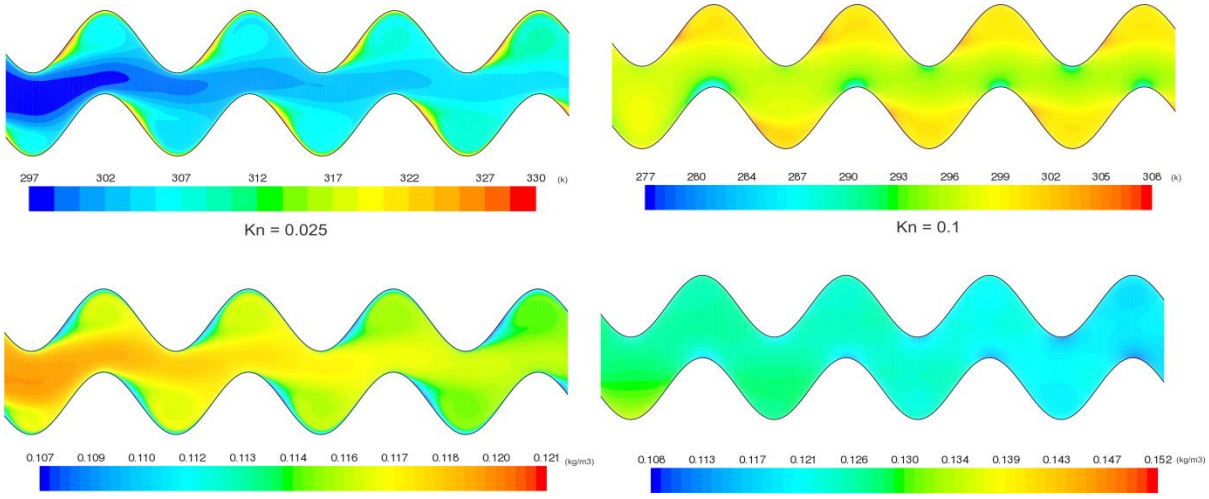

Figure 7. Temperature and density contours, wavy channel with amplitude, A1, third wave in the center of the channel, (a) Kn = 0.025, (b) Kn = 0.1

Figure 8 presents the variations of the local Nusselt number for Knudsen numbers within the slip flow regime. In the channel entrance, the heat transfer rates are steep due to high temperature gradients and conjunction with the thin thermal boundary layer, which presents little thermal resistance. After an adjustment from the uniform inlet temperature imposed on the entrance of the channel the Nusselt number exhibits a cyclic behavior in each subsequent wave, and noticeably the dimensionless heat transfer coefficient decrease with increased Knudsen number. Figure 9 shows the variations of the local Nusselt number with amplitude. It is clear that increasing the amplitude of the channel enhances the heat transfer rate.

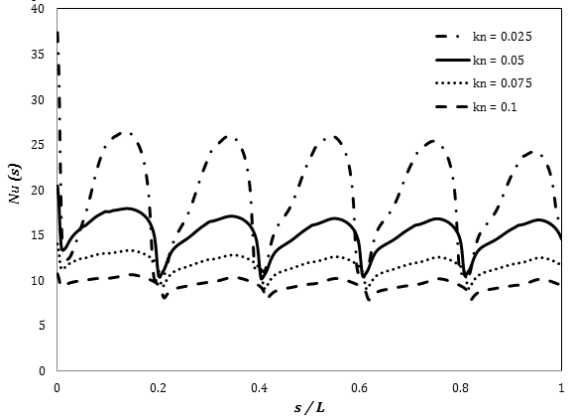

Figure 8. Variation of local Nusselt number vs. dimensionless stream-wise location, Kn = 0.025, 0.05, 0.075, and 0.1, for the wavy channel with amplitude, A1.

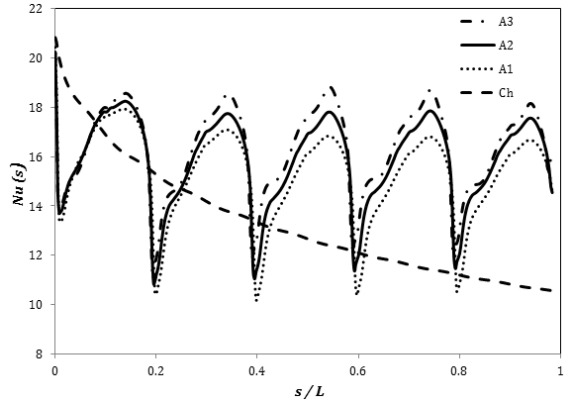

Figure 9. Variation of local Nusselt number along the microchannel, for the three amplitudes and the planar channel, Kn = 0.05.

Figure 10 and Figure 11 present the effect of rarefication and varying wave amplitude on the channel-averaged friction factor and Nusselt number. The frictional resistance decreases linearly with rarefication at two different rates. Whereas, the Nusselt number decreases linearly with increased rarefication at nearly fixed rate. The effect of the increase in the channel amplitude clearly enhances the heat transfer rate at the cost of increase in frictional losses. In addition, the slip velocity increases heat transfer rate since it increases advection in a region where diffusion is the dominate mode of transport. On the other hand, the temperature jump at the wall reduces the heat transfer rate by creating an effect similar to "contact resistance" such that the net effect is a reduction in heat transfer. In order to assess the effectiveness of waviness on the characteristic of flow and heat transfer in the microchannel, channel-averaged values of those of the planar channel normalize the friction factor and average Nusselt number of the wavy channel as follows

$$e_{C_f} = \frac{C_{f_{Wavy}}}{C_{f_{Planar\ Channel}}} \tag{8}$$

$$e_{Nu} = \frac{Nu_{Wavy}}{Nu_{Planar\ Channel}} \tag{9}$$

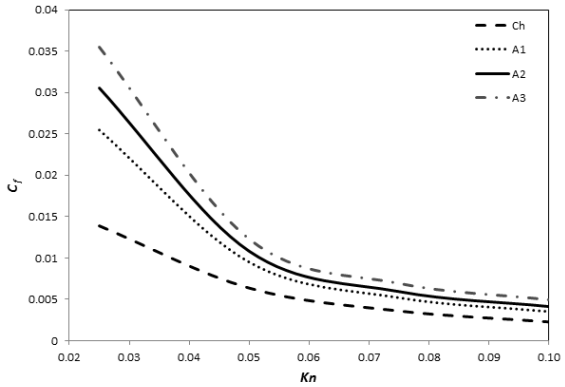

Figure 10. Effect of Kn number and wave amplitude on the average friction coefficient.

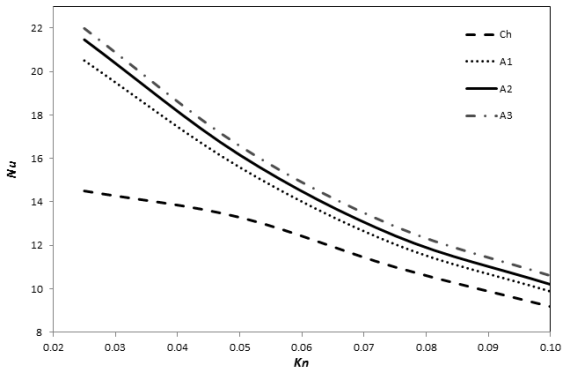

Figure 11. Effect of Kn number and wave amplitude on the average Nusselt number.

Figure 12 and 13 shows for a given Knudsen number the friction losses and augmentation in the heat transfer. The enhancement of heat transfer with increased waviness comes at the cost of increased frictional effects. On the average the pressure drop penalty is about 58%, 84%, and 115% for amplitudes A1, A2, and A3, respectively. However, nearly reaching an asymptotic value with increased rarefication effect. The corresponding heat transfer enhancement is on the average is 19%, 23%, and 27%. The average Nusselt number and friction factor are correlated to Kn number as follows:

$$Nu = c_1 \left(\frac{A}{\lambda_o}\right)^a Pr\ e^{(-b\,Kn)} \tag{10}$$

$$C_f = \left(\frac{A}{\lambda_o}\right)^d \left(c_2 + c_3\, e^{(-f\,Kn)}\right) \tag{11}$$

Where A and λ_0 are the amplitude and length of the wave, the constants are given as:

$a = 0.2$, $b = 10.16$, $d = 0.75$, $f = 52.5135$, $c_1 = 45.586$, $c_2 = 0.0077$and $c_3 = 0.1979$; the expected average error for either correlations is less than 2.5%.

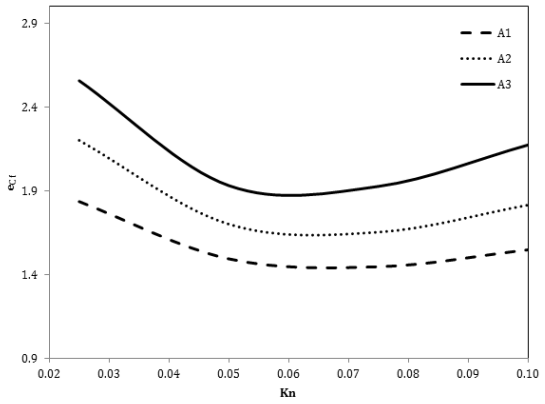

Figure 12. Effect of wave amplitude on the enhancement of heat transfer.

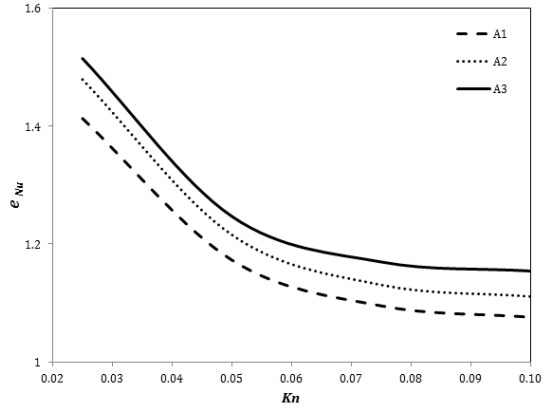

Figure 13. Effect of wave amplitude on the pressure drop penalty.

4. Conclusions

A steady two-dimensional analysis of developing flow through a wavy microchannel has been carried out. It is found that the slip velocity and temperature jump increase with increasing Kn number. Increased rarefication has a diminishing effect on both the heat transfer rate and frictional losses. However, the increase in channel waviness enhances the heat transfer at the cost of higher frictional losses. On the average the pressure drop penalty is about 58%, 84%, and 115%, for the three amplitudes considered which corresponds to average augmentation in heat transfer rate of 19%, 23%, and 27%, where a planar channel of same footprint as the three wavy channels is taken as the base-line reference. The friction factor and Nusselt number are correlated to Kn number.

REFERENCES

[1] T. Yeom, T.W. Simon, T. Zhang, M. Zhang, M. North, T. Cui, "Enhanced heat transfer of heat sink channels with micro pin fin roughened walls". International Journal of Heat and Mass Transfer, Vol. 92 (2016), 617-627.

[2] Y. Bakhshan, A. Omidvar, "Calculation of friction coefficient and analysis of fluid flow in a stepped micro-channel for wide range of Knudsen number using Lattice Boltzmann (MRT) method". Physica A, Vol. 440 (2015), 161-175.

[3] M. Darabndi, M. Sabouri, "Detail study on improving micro/nano gas mixer performance in slip and transitional flow regimes". Sensors and Actuators B Vol. 218 (2015), 78-88.

[4] S. Kiwan and M. A. Al-Nimr, "Flow and heat transfer over a stretched microsurface". ASME transaction Journal of Heat Transfer, Vol. 131 (2009) No. 6, 0617031-0617039.

[5] S. Kiwan and M. A. Al-Nimr, "Investigation into the similarity for boundary layer flows in micro-systems". ASME, transaction Journal of Heat Transfer Vol. 132 (2010) No. 4, 041011- 041019

[6] A.M. Shakir , A.K. Mohammed, M. I. Hasan, "Numerical investigation of counter flow microchannel heat exchanger with slip flow heat transfer". International Journal of Thermal Sciences. Vol. 50 (2011), 2132-2140

[7] F.V. Castellões , J.N. Quaresma , R.M. Cotta, "Convective heat transfer enhancement in low Reynolds number flows with wavy walls". International Journal of Heat and Mass Transfer Vol. 53 (2010), 2022–2034.

[8] T. Zhang , L. Jia , L. Yang, Y. Jaluria, "Effect of viscous heating on heat transfer performance in microchannel slip flow region". International Journal of Heat and Mass Transfer. Vol. 53 (2010), 4927–4934.

[9] K. Hooman, A. Ejlali, "Effects of viscous heating, fluid property variation, velocity slip, and temperature jump on convection through parallel plate and circular microchannel". International Communications in Heat and Mass Transfer. Vol. 37 (2010), 34–3.

[10] Y. Ji, K. Yuan, J.N. Chung, "Numerical simulation of wall roughness on gaseous flow and heat transfer in a microchannel." International Journal of Heat and Mass Transfer, 49, (2006), 1329-1339.

[11] G.L. Morini, M. Lorenzini, M. Spiga, "A criterion for experimental validation of slip-flow models for incompressible rarefied gases through microchannels". Microfluid Nanofluid, Vol. 1 (2005), 190-196.

[12] J.A. Rached, N. M. Daher, "Numerical prediction of slip flow and heat transfer in microchannels". International Journal of Thermal Sciences. Vol. 2 (2006) No. 5, 870-881.

[13] A. Demsis, S.V. Prabhu, A. Agrawal, "Influence of wall conditions on friction factor for flow of gases under slip condition". Experimental Thermal and Fluid Science. Vol. 34 (2010), 1448–1455.

[14] A. ALShqirate, M. Hammad, M. Tarawneh, "Cooling of superheated refrigerants flowing inside mini and micro tubes, study of heat transfer and pressure drop, CO_2, case study", Jordan Journal of Mechanical and Industrial Engineering, Vol. 6 (2012) No. 2, 199-203.

[15] A. Demsis, B. Verma, S.V. Prabhu, A. Agrawal, "Experimental determination of heat transfer coefficient in the slip regime and its anomalously low value", Physical Review E Vol. 80 (2009), 016311.

[16] A. Demsis, B. Verma, S.V. Prabhu, A. Agrawal, "Heat transfer coefficient of gas flowing in a circular tube under rarefied condition". International Journal of Thermal Sciences, Vol. 49 (2010), 1994-1999.

[17] A.Q. Zade, M. Renksizbulut, J. Friedman, "Heat transfer characteristics of developing gaseous slip-flow in rectangular microchannels with variable physical properties". International Journal of Heat and Fluid Flow Vol. 32 (2011), 117–127.

[18] H.A. Mohammed , P. Gunnasegaran, N.H. Shuaib, "Influence of channel shape on the thermal and hydraulic performance of microchannel heat sink". International Communications in Heat and Mass Transfer. Vol. 38 (2011), 474–480.

[19] M. Shojaeian , Seyed, A. R. Dibaji, "Three-dimensional numerical simulation of the slip flow through triangular micro-channels". International Communications in Heat and Mass Transfer. Vol. 37 (2010), 324–329.

[20] Z, Guo , Z. Li, "Size effect on single-phase channel flow and heat transfer at microscale." International Journal of Heat and Fluid Flow. Vol. 24 (2003) 284–298.

[21] Y. Sui, P.S. Lee, C.J. Teo, "An experimental study of flow friction and heat transfer in wavy microchannels with rectangular cross section." International Journal of Thermal Sciences. Vol. 50 (2011), 2473-2482.

[22] H. Shokouhmand, S. Bigham, "Slip-flow and heat transfer of gaseous flows in the entrance of a wavy microchannel." International Communications in Heat and Mass Transfer. Vol. 37 (2010), 695–702.

[23] P.E. Geyer, D.F. Fletcher, B.S. Haynes, "Laminar flow and heat transfer in a periodic trapezoidal channel with semi-circular cross-section", International Journal of Heat and Mass Transfer. Vol. 50 (2007), 3471–3480.

[24] A.M. Guzmán, M.J. Cárdenas, F.A. Urzúa, P.E. Araya, "Heat transfer enhancement by flow bifurcations in asymmetric wavy wall channels". International Journal of Heat and Mass Transfer, Vol. 52 (2009), 3778–3789.

[25] M.Z. Hossain, S. Islam, "Numerical investigation of fluid flow and heat transfer characteristics in sine, triangular, and arc-shaped channels". Thermal Science Vol. (2007) No. 1, 17-26.

[26] A. Agrawal, "A comprehensive review on gas flow in microchannels". International Journal of Micro-Nano Scale Transport. Vol. 2 (2011) No.1, 1-40.

[27] J.C. Maxwell, "On stresses in rarefied gases arising from inequalities of temperature". Philosophical Transactions of the Royal Society of London, Vol. 170 (1879), 231–256.

[28] M. von Smoluchowski, U. Wärmeleitung, "Verdünnten Gasen". Annual Review of Physical Chemistry, Vo. 64 (1898), 101–130.

[29] D.A. Lockerby, J.M. Reese, D.R. Barber, "Velocity Boundary Condition at Solid Wall in Rarefied Gas Calculations". Physical Review E, Vol. 70 (2004) No. 1, 017303 (2004)

[30] Colin S, Single-phase gas flow in microchannels. In: Kandlikar S, Garimella S, Li D, Colin S, King MR, editors. Heat Transfer and Fluid Flow in Minichannels and Microchannels; Oxford, UK, Elsevier Ltd, 2006, p. 9-86.

[31] FLUENT® Inc.

[32] A. Agrawal and S.V. Prabhu, "Survey on measurement of tangential momentum accommodation coefficient". Journal of Vacuum Science and Technology A, Vol. 26 (2008) No. 4, 634-645.

المملكة الأردنية الهاشمية

الجامعة الهاشمية

المجلة الأردنية
للهندسة الميكانيكية والصناعية

JJMIE

مجلة علمية عالمية محكمة

تصدر بدعم من صندوق البحث العلمي

http://jjmie.hu.edu.jo/

ISSN 1995-6665

المجلة الأردنية للهندسة الميكانيكية والصناعية

مجلة علمية عالمية محكمة

المجلة الأردنية للهندسة الميكانيكية والصناعية: مجلة علمية عالمية محكمة تصدر عن الجامعة الهاشمية بالتعاون مع صندوق دعم البحث العلمي في الأردن

هيئة التحرير

فريـق الدعـم

ترسل البحوث إلى العنوان التالي

رئيس تحرير المجلة الأردنية للهندسة الميكانيكية والصناعية

الجامعة الهاشمية
كلية الهندسة
قسم الهندسة الميكانيكية
الزرقاء - الأردن

هاتف : 3903333 5 00962 فرعي 4537

Email: jjmie@hu.edu.jo

Website: www.jjmie.hu.edu.jo